CFD Modeling and Measurement of Liquid Flow Structure and Phase Holdup in Two- and Three-Phase Bubble Columns

Von der Gemeinsamen Fakultät für
Maschinenbau und Elektrotechnik
der Technischen Universität Carolo-Wilhelmina zu Braunschweig

zur Erlangung der Würde
eines Doktor-Ingenieurs (Dr.-Ing.)
genehmigte Dissertation

von Dipl.-Ing. Volker Michele
aus Recklinghausen

Eingereicht am: 8. Oktober 2001
Mündliche Prüfung am: 4. März 2002
Referent: Prof. Dr.-Ing. D. C. Hempel
Korreferent: Prof. Dr.-Ing. M. Bohnet

This project report has been prepared using LaTeX with the `dvipdfm` package. It is available online for free from Technical University of Braunschweig's OPuS Server under http://opus.tu-bs.de/opus/index_1.html or via http://www.ibvt.de/forschung/diss/diss.htm; a printed version may be obtained from FIT-Verlag, Am Langen Hahn 31, D-33100 Paderborn / Germany.

The author's e-mail address (V.Michele@tu-bs.de) will remain a valid alias; information on Technical University of Braunschweig's Institute of Biochemical Engineering may be obtained from http://www.ibvt.de or from ibvt@tu-bs.de.

Paying Tribute...

I am obliged to the following people and institutions without whose help this project could not have been completed:

- Prof. D. C. Hempel for this interesting and challenging topic, the granted freedom and continued support in all phases of the work,
- Prof. M. Bohnet for taking over the position of co-examiner and generously letting me temporarily use the Institute of Process and Nuclear Technology's CFX licences,
- Prof. J. Schwedes for taking over the position of chairman of the examination board,
- my colleagues Holger Dziallas, Eike Mahnke and Jan Enß who always had an open ear for my troubles and by asking the right questions helped me understand some of the more complicated project aspects better myself,
- all other colleagues at the Institute of Biochemical Engineering for providing a relaxed yet focused work environment,
- Saskia John, Roland Wilfer, Holger Parchmann and Prof. N. Räbiger from University of Bremen's Institute of Environmental Process Engineering for providing equipment and continued support for the Electrodiffusion Measurements,
- Josef Schüle from TU Braunschweig's Institute of Scientific Computing for fruitful discussions on numerical issues and for support with the compute servers,
- Christoph Kohnen from TU Braunschweig's Institute of Process and Nuclear Technology for helpful discussions and support with CFX,
- Frank Lehr from University of Hannover's Institute of Process Engineering for help with CFX and for letting me use his Fortran routine for computation of time-averages,
- Santiago Lain from University of Halle-Wittenberg's Institute of Mechanical Process Engineering for helpful comments on the manuscript,
- all the other colleagues participating with Deutsche Forschungsgemeinschaft's Focus Program "Analysis, Modeling and Computation of Multiphase Flows" for interesting meetings and good discussions,

- the workshop staff at Leichtweiss Institute for Hydraulic Engineering (especially H.-P. Hollmann and H. Appeltauer) and at the Physics department (especially A. Ellermann) for fast and precise work,

- all the students for valuable services with computer and measurement work, namely Andreas Reuter, Linus Aschenbach, Michael Vollmert, Sridhar Thatikunda, Stefan Leschka and Vijaykanth Ponnada,

- Deutsche Forschungsgemeinschaft (DFG) and the Province of Niedersachsen for funding of this project,

- My parents Margot and Jürgen Michele and my brother Oliver for support and help with the more general aspects of a student's life.

Braunschweig, March 2002

Volker Michele

Contents

1 Introduction

Multiphase flows are of fundamental importance in many reactor concepts in today's chemical and bioprocess industry. Over the last years, increasing volumes of products manufactured in fermentation processes or using heterogeneous catalysis have yielded a need for large-scale reactors, in turn inducing new demand for precise scale-up rules for the transfer of processes from lab-scale to full industrial scale which in the case of bubble columns can mean diameters of several meters.

Design of gas-liquid bubble columns has so far mainly been carried out by means of empirical and semi-empirical correlations which have been gained from experimental data e. g. of mass transfer for bubble columns of different scales [27]. While a strong experimental foundation of such correlations provides security for the applications that they initially were conceived for, transferability to other situations (e. g. different substances or temperature and pressure ranges) is usually very limited. Thus, in many cases trial-and-error schemes or time-consuming scale-up experiments are necessary to achieve satisfactory performance of the large-scale reactor system.

Three-phase flow in bubble columns introduces additional challenges for design and scale-up. Now, not only gas-liquid mass transfer is of concern but additionally, solid fluidization and liquid-solid heat and mass exchange enter the picture yielding a complex interaction of turbulent flow fields, mass transfer and chemical or biochemical reaction inside the reactor. Even modern approaches to reactor scale-up mostly do only consider single aspects out of this multitude, i. e. are restricted to fluiddynamic facets, mass transfer issues or reaction topics [103]. Complete reactor models are still out of reach mostly due to numerical problems in solving the resulting equation systems and – the accelerating development in this field notwithstanding – due to a lack in computational power.

On the measurement side of the issue, recent developments have cast some light into gas distribution and solid fluidization depending on superficial gas velocity and sparger geometry in three-phase bubble columns of pilot-plant scale. Based on work by Sauer and Hempel [101], Lindert et al. [69, 70] and Kochbeck et al. [56], Dziallas et al. [31, 32] have developed a new invasive measurement technique based on a combination of differential pressure measurement and conductivity respectively time domain reflectometry measurement which enables a detailed determination of local gas and solid holdup. Using this new technique, interesting aspects of

sparger geometry and superficial gas velocity influence on local gas distribution as well as solid fluidization in a model system consisting of deionized water, plastic granules and air could be shown.

On the modeling side, Computational Fluid Dynamics (CFD) are gaining importance in general process applications. CFD approaches use numerical techniques for solving the Navier-Stokes equations for given flow geometry and boundary conditions thereby implementing models for flow aspects like turbulence or heat and mass transfer as relevant for the specific modeling task. CFD has been an important tool in air and space industry or vehicle design for a long time [2] where it has to a large extent replaced time-consuming and expensive wind tunnel experiments. Yet, while in these applications single-phase flows are prevailing, modeling applications in chemical and biochemical reactors in most cases include multiphase flows the modeling and numerical treatment of which introduce additional challenges [24, 29]. Therefore, multiphase CFD applications have gained broad attention only during the last decade since increasing computational power available has enabled computations previously considered infeasible. Still, most literature reports are limited to two-phase flows [7], and especially gas-liquid CFD projects often deal only with very low dispersed phase holdups. In effect this means that multiphase CFD still is far away from being a general tool for the practitioner even if recent advances in computational power available in desktop PCs do enable first steps in this direction [45, 116].

Starting point for the project presented in this report was the question how liquid flow structure inside a pilot plant-size bubble column is interacting with local gas and solid holdup, i. e. what influence gassing rate has on liquid flow, how liquid flow is related to solid fluidization and what influence solid loading on liquid circulation and mixing inside the reactor has. For this purpose, the Electrodiffusion Measurement technique (EDM) was to be implemented for reason of its capabilities to deliver two-dimensional liquid velocity values even at high gas and solid holdups inside the 0.63 m diameter, 6 m high bubble column as used by Dziallas et al. [31, 32]. Fig. 1.1 shows the experimental setup.

The reactor could be equipped with a plate sparger (335 holes of 1 mm diameter in triangular layout), a ring sparger (diameter 0.45 m, 12 gassing openings facing to the bottom of the reactor for better solid fluidization) or a central nozzle sparger (diameter 22 mm). Table 1.1 shows properties of the model system as introduced by Dziallas et al. [31, 32] and used for the experiments of the present work.

The model system and especially the solid material have been chosen such as to resemble the flow situation inside a bubble column bioreactor where microorganisms grow immobilized on particles and aeration is used for oxygen intake, mixing and fluidization.

In addition, a Computational Fluid Dynamics (CFD) model based on the experimental results was to be developed that – neglecting mass transfer and chemical reactions for the time being – should be able to reproduce the measured distributions of gas and solid holdup as well as liquid

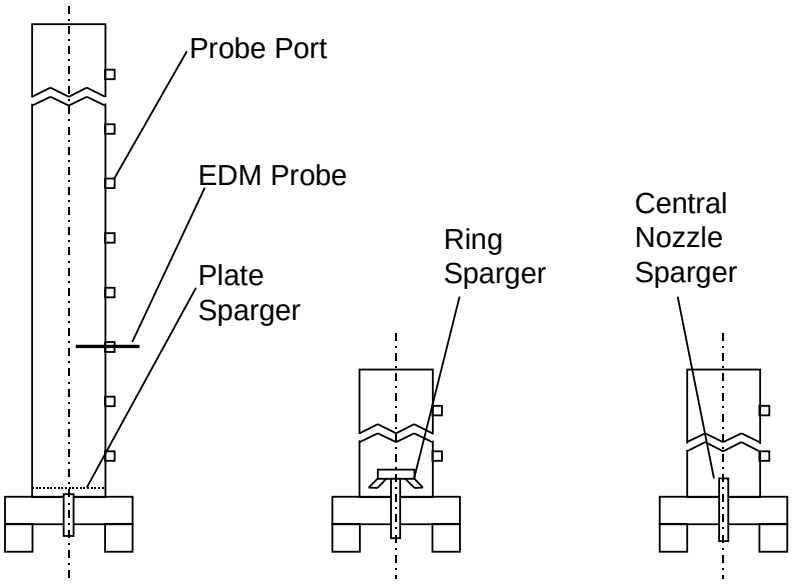

Figure 1.1: Experimental setup: Pilot-plant sized bubble column with different sparger systems; column height 6 m, inner diameter 0.63 m

Table 1.1: Properties of the three-phase model system chosen for the experiments

Liquid Phase	Deionized water with 0.01 mol/L Potassium-Sulfate
Gas Phase	Oil-free pressurized air
Solid Phase	Plexiglass (Polymethyl-Methacrylate, PMMA) particles, density 1200 kg/m^3, cubically shaped, hydraulic diameter 3 mm

velocity thus yielding a flow and holdup prediction tool useful for scale-up calculations as well. Implementation of the model should take place on a common PC workstation such as to show that CFD reactor design studies can be carried out on standard modern desktop hardware at reasonable computation times.

2 Multiphase Flow Fundamentals

2.1 Modeling Fundamentals: The Roots

Modern approaches to modeling of chemical process equipment draw their impetus from two distinct sources. On one side, empirical and semi-empirical reactor modeling approaches based on a long history of dimensional analysis can be found. On the other side, modern Computational Fluid Dynamics (CFD) that have been popular for quite a while in other fields of science (like air and space engineering) are becoming more and more interesting for chemical engineers. Both fields are still coexisting but with computational resources becoming cheaper and more widely available, they soon will develop into one stream of detailed reactor modeling. A first step in this direction has been taken by Bauer and Eigenberger [3] who in their so-called "Multiscale Approach" described the fluid dynamics via CFD computation and included chemical reaction and mass transfer by means of a zone model.

2.1.1 Empirical and Semi-Empirical Models for Bubble Columns

Before the advent of CFD techniques, reactor modeling for chemical and biotechnological purposes was mainly carried out by means of highly simplified, semi-empirical parameter-fitting models. This was due to the fact that with computational resources available until just a short time ago, calculations with more precise models would have taken up a prohibitive amount of time thus being way too expensive for any application of interest. However, if one's interests are limited to certain singular phenomena such as mixing, residence time distribution or averaged mass transfer coefficients for a tightly defined reactor type, a huge body of correlations can be found from the literature [27]. While the limited range of a model's applicability always has to be kept in mind, in the field of two- and three-phase bubble column and airlift loop reactor modeling (and the adjoining area of fluidized bed modeling) a number of approaches have gained large popularity due to their comparatively general validity [103]. Namely these models are:

- Cell models: These models assume circulation cells inside the reactor which are responsible for backmixing processes [26].

- The one-dimensional dispersion model: This model assumes that two- and three-phase flow processes can be modeled as a superposition of convective and dispersive flow where the latter is described in analogy to Fick's first law of diffusion [59, 62, 69, 73, 103, 110, 111]. It is often used in conjunction with gravity terms to model sedimentation effects [25, 101]. More refined versions of this model include sparger and degassing zone effects as well [35].

- Cascade models: These models describe real reactors such as bubble columns or airlift reactors in terms of cascades of ideal continuous stirred tank reactors (CSTRs). Main fitting parameter is the number of tanks in the cascade; backmixing effects can also be included by introducing partial backflow into the model [69].

- The two-dimensional dispersion model in cylindrical coordinates: This model includes radial effects in addition to axial dispersion. In cylindrical coordinates it can be formulated as follows [103]:

$$\frac{\partial \varepsilon_\alpha}{\partial t} = D_{ax,\alpha} \cdot \frac{\partial^2 \varepsilon_\alpha}{\partial x^2} - v_{ax,\alpha,c} \cdot \frac{\partial \varepsilon_\alpha}{\partial x} + \frac{1}{r} \cdot D_{rad,\alpha} \cdot \frac{\partial \varepsilon_\alpha}{\partial r} + D_{rad,\alpha} \cdot \frac{\partial^2 \varepsilon_\alpha}{\partial r^2} \tag{2.1}$$

  A similar equation can be put up for any continuous phase α or dispersed phase β. This model delivers – like its one-dimensional version – only reasonable results for phases which are continuously flowing through the reactor. A simpler model for bubble distribution in three-phase fluidized beds which only considers radial dispersion has been presented by Lee and de Lasa [65].

- Mechanical power balance models: These models calculate liquid circulation velocities from pneumatic power input into the reactor due to gas sparging. This is accomplished by solving force balances including pressure loss and gravitational terms [131].

With the application of the models listed above, great care has to be taken with respect to the areas of their validity. Empirical or semi-empirical models usually are verified only for a limited set of parameter variations. While interpolation between those given values may be viable, extrapolation will always yield results of questionable integrity. This also puts serious limitations to the models' scale-up capabilities.

2.1.2 Computational Fluid Dynamics

Computational Fluid Dynamics (CFD) are an engineering tool which has gained large popularity during the last years. As opposed to the semi-empirical models described above, CFD aims at solving the (complete or simplified) fundamental physical equations that describe a flow phenomenon. The most general form of these equations has been given by Navier and Stokes more than 150 years ago, therefore the set of equations has been aptly named Navier-Stokes equations [2, 120].

These equations encompass mass, momentum and energy balances; they have to be adapted to the specific problem under consideration by additional closure laws [34].

While CFD has been very popular among car manufacturers and in the air and space industry [38], chemical engineers have only recently become aware of the large potential it bears for the development and improvement of process equipment. This is mainly due to the fact that with modeling flow around a car body or an airplane wing, only single-phase flow has to be considered while in most applications in chemical reactors two- and three-phase flows are common. This poses a wealth of new questions and brings about serious difficulties in modeling and numerics.

2.2 Multiphase CFD

In multiphase flow, solving one single mass balance and three momentum balances is no longer sufficient to compute flow fields for all involved phases. While all multiphase CFD approaches do solve these balances for the continuous phase, different ways of treating the dispersed phases have been suggested. However, all models are still way from being reliable tools for the improvement of existing processes or for scale-up considerations. As Sundaresan [116] has pointed out, this is mainly due to the fact that most models have to be numerically solved on grids that are much coarser than the flow structures that one wants to resolve, simply because available computational power is by far not sufficient. This situation is worsened by the fact that unlike with single-phase flow, two-dimensional and steady-state calculations deliver no useful results making three-dimensional transient calculations unavoidable. While a lot of work has already been published on gas-liquid two-phase flow, three-phase flow modeling is still at the very beginning.

2.2.1 Basic Concepts

In multiphase CFD, two main approaches can be discriminated. While all models compute the flow field of the continuous phase using the Navier-Stokes equations, the dispersed phases can either be calculated in a Lagrangian manner as consisting of discrete entities (bubbles, particles or clusters) or as semi-continuous phases where all phases are regarded as interpenetrating continua (Euler-Euler or multi-fluid approach). The **Lagrangian approaches** can be divided according to their treatment of the dispersed phases as follows:

- The Euler-Lagrange Approach: With this concept, bubbles and particles are considered as having a fixed size and shape; computational particles always represent a certain number of real particles. In the numerical solution procedure, the transient Navier-Stokes equations for the continuous phase are solved first; particle velocity and new particle position for the next time step are then calculated using friction laws for every single computational particle

[24, 28, 48]. In an optional third step, two-way coupling effects can be considered where the particles' influence on the continuous-phase flow field are calculated and a new flow field is computed iteratively. Particle-particle or particle-wall interactions can be incorporated into the model as well [112]. As can easily be imagined, the computational effort for this calculation procedure increases drastically with increasing dispersed phase content, leaving its main use so far in the computation of dilute systems or for special applications like residence time distribution calculations which cannot be computed using multi-fluid approaches [64].

- Direct Numerical Simulation (DNS): With the standard Lagrange approach, a particle is considered as occupying only one grid cell at a time giving only one relevant velocity acting on it. In a more refined approach, particles can occupy more than one cell and subsequently experience different velocities simultaneously [30, 67]. In addition, turbulence is resolved directly without any modeling [8, 126]. This yields much more complex particle motions and calls for much finer numerical grids and shorter time steps resulting in an even larger computational demand. Since DNS in general gives very precise results, it is increasingly being used to verify other modeling approaches when experiments are infeasible [9]. A subdivision of DNS called Large Eddy Simulation (LES) tries to reduce computational demand by directly resolving only the larger turbulence eddies and modeling the smaller ones thus enabling calculations on a coarser grid and with larger time steps [126].

- Volume-of-Fluid Methods: In this even more refined approach for the modeling of gas-liquid two-phase flow, bubbles are considered as deformable; even free surfaces can be modeled [43, 68, 117]. One single field of flow vectors is computed; bubbles are distinguished from the liquid by their lower density which means that volume fractions are used to represent surfaces. The sharp density transition at the surface and the fact that rather coarse grids have to be used pose a number of questions related to bubble mass conservation and the calculation of smooth bubble surfaces; for numerical reasons, by now the density ratio between liquid and gaseous phase may not exceed a value of 20 which renders calculations of actual air bubbles in water (density ratio of approximately 800) impossible. While this class of methods has been successfully implemented for the calculation of free surface flows (e. g. bubbles rising to a surface and dissolving there inducing droplet formation [117]), it is still prohibitive for real-life reactor modeling with respect to its immense computational demand.

As can easily be seen from the model descriptions above, all Lagrangian particle-tracking models suffer from high demands on computational power; this renders them rather unsuitable for the computation of multiphase flows in real process applications where dispersed phase holdups are usually high. Therefore, in this project the Euler-Euler or multi-fluid approach will be imple-

mented which allows for the computation of three-phase flow fields even with high solid and gas holdups at reasonable computational expense.

With the **Euler-Euler** or **multi-fluid approach**, a set of Navier-Stokes equations has to be put up for every phase under consideration. This means that if no energy equations are solved (i. e. for isothermal flow conditions which are always assumed here), in three-phase flows 12 partial differential equations (PDEs) have to be solved simultaneously. Depending on which phase interactions are included in the model (e. g. particle-particle or particle-wall interactions or effects due to rotating particles and surface tension), these equations can take on very different appearances [36, 53, 85, 127]. A most complete survey of equation types including terms to even cover flow regime transitions in horizontal evaporator pipes is given by Lahey and Drew [63] and in the book by Drew and Passman [29].

The inclusion of mass transfer and chemical reactions into CFD calculations by means of species balances and reaction kinetic rate equations is fairly straightforward from a conceptional point of view but still suffers from numerical limitations due to the strong coupling of the resulting system of equations. Therefore, CFD approaches which include these effects so far have mainly used simplified semi-empirical models for the description of mass transfer and reactions; e. g. Bauer and Eigenberger [3] have investigated into the possibilities of a so-called "Multiscale Approach" for the description of a nonisothermal parallel-consecutive reaction. In this project, neither mass transfer nor chemical reactions have been included into the calculations.

Several authors have reported on attempts at solving the two-dimensional multiphase Navier-Stokes equations thereby hoping to be able to reduce computational demand [61, 81, 109]. What they found was, however, that no reasonable, grid-independent results could be obtained leaving three-dimensional computations as the only viable approach. The same outcome is reported on steady-state calculations [28, 79, 93, 109] which only proved that bubble column calculations have to be performed in a transient manner. All of these results are somewhat of a drawback to the initial hope that with multi-fluid calculations computational demand could be reduced drastically.

With these results in mind, the Navier-Stokes equations as used here can be put up in a manner following [83, 93]. The continuity equation without mass transfer and source terms (i. e. without consideration of chemical reactions) in multiphase formulation becomes for both continuous and dispersed phases:

$$\frac{\partial}{\partial t}(\rho_\alpha \varepsilon_\alpha) + \frac{\partial}{\partial x_i}(\rho_\alpha \varepsilon_\alpha u_{\alpha,i}) = 0 \tag{2.2}$$

The momentum balance in multiphase formulation can be written out slightly differently for continuous and dispersed phases. For the continuous phase, it becomes in general formulation:

$$\begin{aligned} \frac{\partial}{\partial t}(\rho_\alpha \varepsilon_\alpha u_{\alpha,i}) + \frac{\partial}{\partial x_j}(\rho_\alpha \varepsilon_\alpha u_{\alpha,i} u_{\alpha,j}) &= -\varepsilon_\alpha \frac{\partial p}{\partial x_i} + \frac{\partial}{\partial x_j} \varepsilon_\alpha \mu_\alpha \left(\frac{\partial u_{\alpha,i}}{\partial x_j} + \frac{\partial u_{\alpha,j}}{\partial x_i} \right) \\ &\quad + \rho_\alpha \varepsilon_\alpha g_i + M_{\alpha,i} \end{aligned} \tag{2.3}$$

Writing down momentum balances for the dispersed phases yields:

$$\frac{\partial}{\partial t}(\rho_\beta \varepsilon_\beta u_{\beta,i}) + \frac{\partial}{\partial x_j}(\rho_\beta \varepsilon_\beta u_{\beta,i} u_{\beta,j}) = -\varepsilon_\beta \frac{\partial p}{\partial x_i} + \frac{\partial}{\partial x_j} \varepsilon_\beta \mu_\beta \left(\frac{\partial u_{\beta,i}}{\partial x_j} + \frac{\partial u_{\beta,j}}{\partial x_i} \right) + \rho_\beta \varepsilon_\beta g_i + M_{\beta,i} \quad (2.4)$$

In the above equations, gas and liquid viscosity are given the actual values valid for the local conditions (temperature, pressure) in the reactor or – in case of the liquid phase – are modified to account for turbulence influence. With solid viscosity, no value or correlation for three-phase flow can be obtained from literature data (solid pressure approaches implementing kinetic theory for fluidized beds [36] can not be transfered in a straightforward manner). It is basically a fitting parameter which has been set constant to the value of water (10^{-3} Pas) for all calculations of this project. This is assumed a legal approximation since test calculations showed that a variation of solid viscosity between 10^{-4} Pas and 10^{-1} Pas did not yield a significant difference in computed time-averaged dispersed phase distribution and liquid flow fields.

Detailed formulation of turbulence and phase interaction terms will be given in section 2.2.4.2 and section 2.2.3, respectively. These terms are of crucial importance for the correct calculation of flow and holdup structure. Even with two-phase flows, laminar calculations cannot deliver grid-independent results [93, 109], thus turbulence models have to be implemented which account for sub-grid size flow structures. In three-phase flows, direct interactions between gas and solid dispersed phases have to be modeled as well in order to achieve correct solid fluidization.

To obtain a solvable system with as many equations as unknowns present, additional closure equations have to be implemented accompanying the 12 partial differential Navier-Stokes equations [29]. These may be algebraic equations or PDEs as well. Since adiabatic gas expansion with increasing vertical position in the bubble column is the main reason for the measured axial gas holdup profiles [31], a CFD model has to consider the gas phase compressibility as well; liquid and solid phases are assumed incompressible. This means that a relationship between gas density and static pressure has to be found; in this project, the ideal gas law has been used where gas constant and temperature are assumed as constant throughout the calculations:

$$\rho_g = \frac{p \cdot \tilde{M}_g}{\tilde{R} \cdot T} \quad (2.5)$$

Here, the molar mass of the gas phase is given the value of air ($\tilde{M}_g$ = 28.8 kg/kmol), the gas constant is set to $\tilde{R}$ = 8.315 kJ/(kmol K). Gravity effects are included in the body force terms of the momentum equations (e. g. $\rho_\beta \varepsilon_\beta g_i$ for dispersed gas or solid phase). While several authors have reported on bubble size models which account for coalescence and break-up effects [22, 66, 77, 78, 108], these effects are neglected here for the sake of simplicity and convergence and bubble size is set to a constant value of 0.008 m. Bubble-bubble interactions and wake effects are neglected as well [54]. Interactions between gas and solid phases, however, have to be modeled in order to obtain correct solids fluidization (see section 2.2.3.2).

Turbulence has an influence on the liquid viscosity μ_α in eqn. 2.3; therefore, a turbulence model has to be included yielding additional algebraic and partial differential closure equations. This will be discussed in detail in section 2.2.4.

2.2.2 Application Examples from the Literature

With the increasing popularity of CFD in the field of process engineering, a lot of interesting applications have been reported on both from university researchers and from industrial CFD users. Birthig et al. [7] give a very broad review of CFD modeling activities in the largest German chemical companies (including Degussa-Hüls, Axiva, Bayer and BASF) proving that these methods have been successfully implemented for apparatus modeling tasks ranging from gas spargers over extruders, impellers, pipe reactors, bubble columns, fixed-bed reactors to spray dryers and separation devices. It is interesting to mention, though, that all their examples consider at most two-phase flows. Further surveys of the current state of CFD modeling activities have been given by LaRoche [64] and Sundaresan [116].

Among the very first CFD applications in the field of process engineering to be reported were Stirred Tank computations [84]. This is due to the fact that even single-phase calculations can deliver interesting results about local velocities and mixing conditions inside the tank – without the numerical problems related to multiphase calculations. Kohnen and Bohnet [58] presented a two-fluid model of solid-liquid flow in a stirred tank and investigated especially into turbulent dissipation; with a very refined model they were able to reduce the error between power input of the stirrer and turbulent power dissipation to less than 20 %. Schütze et al. [105] focused on CFD modeling of Oxygen transfer in a stirred tank bioreactor and succeeded in even including the free surface into their mass transfer calculations.

Results on bubble column CFD calculations have been reported by many groups. Pfleger et al. [93] conducted investigations into the behaviour of a flat laboratory-scale rectangular two-phase bubble column using the Euler-Euler approach under CFX-4.2; main result of their work is that even a flat bubble column cannot be modeled two-dimensionally. This result is supported by the work of Sokolichin and Eigenberger [109] who used their own CFD code but had to implement three-dimensional calculations as well. Both of these projects were carried out at extremely low superficial gas velocities (below 0.01 m/s). Krishna et al. [60, 61] reported on CFD modeling of a pilot-plant size bubble column using CFX-4.2 with the Euler-Euler model as well at higher superficial gas velocities (up to 0.28 m/s). While one of their reports is entitled "*Three-Phase Eulerian Simulation*" [61], the reader would be misled to assume that they included solid particles into their considerations; moreover, two dispersed gas phases were calculated to include the different influences of large and small bubbles. In addition, they calculated integral gas holdups and derived a scale-up correlation for bubble columns of different sizes. Sparger influence on the flow

structure in two-phase bubble columns with a low height-to-diameter ratio of two was the aim of investigations carried out by Ranade and Tayalia [95]. Using the commercial code Fluent 4.5.2 with an Euler-Euler approach implementing the k-ε model and in agreement with measurement results they found that single ring spargers induce a characteristic liquid circulation which can not be observed in a double-ring sparger configuration. Three-dimensional calculations could not be avoided for a correct prediction of flow fields.

Three-phase CFD results were presented for bubble columns by Mitra-Majumdar et al. [79] and for airlift loop reactors by Padial et al. [88]. While the first group reports results obtained from two-dimensional calculations in cylindrical coordinates, the latter had to perform full three-dimensional calculations to achieve useful results. Details of Padial et al.'s model and its relevance for this project are given in section 2.2.3.2 below.

Cockx et al. [23] reported on CFD calculations for an industrial-scale drinking water ozonation tower. They included ozone mass transfer into their calculations and computed the ozone concentration in the liquid phase. By adding baffles and moving the contactor inlet to a different position, they could achieve a 100 % efficiency increase of the disinfection process.

CFD modeling results using CFX-4.2 for a randomly packed distillation column were presented by Yin et al. [130]. They compared their results to measurement data obtained at different operating conditions from a 1.22-m-diameter, 3.66 m high packed bed that was equipped with several sizes of Pall rings. Good agreement with the predictions was achieved giving rise to the hope that CFD will become a useful tool for the scale-up of this class of apparatus as well. Similar computations have been carried out for semi-structured catalytic packed beds by Calis et al. [18] using CFX-5.3. They found that pressure drop in such beds can be predicted with an error of less than 10 % compared to measurement results; still for such precision, very fine discretization grids (up to three million grid cells) and correspondingly high computational power is necessary.

Erdal et al. [33] reported on modeling of bubble behaviour in gas-liquid cyclone separators. Using CFX-4.1 they could determine the percentage of bubbles that unwantedly leave the reactor through the bottom liquid outlet and show the influence of correct modeling of turbulent dispersion on this so-called bubble carry-under effect.

Further applications of multiphase CFD techniques have been reported from nuclear reactor engineering; Morii and Ogawa [80] underlined the importance of modeling by quoting the fact that "*Multiphase flow frequently occurs in a progression of accidents of nuclear severe core damage*". Less alarming are reports on CFD applications in conventional power stations where coal is burned in a circulating bed process and dust is collected from flue gases by means of electrostatic precipitators [37].

2.2.3 Inter-Phase Momentum Exchange

When modeling multiphase fluid flow, great attention has to be paid to the correct setup of momentum exchange between the phases – these forces are most important for the resulting dispersed phase distributions and flow velocity fields [19, 21, 22, 29, 48, 85]. Therefore, this section will consider the different phenomena encountered when modeling inter-phase drag. Models for momentum exchange between continuous and dispersed phase (here: between liquid and gas or solids, respectively) will be reviewed and implemented from the literature. With direct momentum exchange between the two dispersed phases (gas and solids), only very little information can be gained from the literature [68, 88]. Therefore, several approaches have been developed and tested as part of this project. Interactions of the gas bubbles among themselves or particle-particle collisions as well as particle-wall interactions [112], virtual mass and lift forces [85] or forces due to particle rotation are neglected for the sake of reduced model complexity and enhanced convergence.

2.2.3.1 Momentum Exchange between Continuous and Dispersed Phase

For modeling of momentum exchange between a continuous and a dispersed phase, particle drag models have been implemented in many variations in the past. With single bubbles rising or particles settling in liquids, similar drag force approaches of the following kind are frequently being used [22, 83]:

$$D_P = \frac{1}{2} C_D \rho_\alpha (u_\alpha - u_\beta)^2 A \tag{2.6}$$

Starting considerations with the momentum balance for the continuous phase, the momentum exchange terms in eqn. 2.3 take on the general form of:

$$M_{\alpha,i} = \sum_{\beta=1}^{N_P} c_{\alpha,\beta}(u_{\beta,i} - u_{\alpha,i}) \tag{2.7}$$

Here, α represents the continuous phase while β denotes the dispersed phases. For the dispersed phases' momentum balances, similar terms can be derived where only the momentum exchange with the continuous phase is considered, i. e. no summation over β takes place:

$$M_{\beta,i} = c_{\alpha,\beta}(u_{\alpha,i} - u_{\beta,i}) \tag{2.8}$$

Since inter-phase forces have to be at an equilibrium, the sum of $M_{\alpha,i}$ (continuous phase) and the dispersed phases' respective $M_{\beta,i}$ have to add up to zero for each spatial direction.

In order to express eqn. 2.6 in a manner consistent with eqns. 2.7 and 2.8, the drag force formulation has to be expanded from single particles or bubbles to a given dispersed phase concentration ε_β. The number of particles per unit volume can be calculated from:

$$n_{P,V} = \frac{\varepsilon_\beta}{V_P} = \frac{6\varepsilon_\beta}{\pi d_P^3} \tag{2.9}$$

Rewriting eqn. 2.6 in vector notation and multiplying with $n_{P,V}$ yields the drag force per unit volume exerted by the dispersed phase on the continuous phase:

$$\mathbf{D}_{\alpha,\beta} = \frac{1}{2} n_{P,V} C_D \rho_\alpha A |\mathbf{u}_\beta - \mathbf{u}_\alpha| (\mathbf{u}_\beta - \mathbf{u}_\alpha) \tag{2.10}$$

$$= \frac{3}{4} \frac{C_D}{d_P} \varepsilon_\beta \rho_\alpha |\mathbf{u}_\beta - \mathbf{u}_\alpha| (\mathbf{u}_\beta - \mathbf{u}_\alpha) \tag{2.11}$$

A comparison of eqns. 2.7 and 2.11 serves to identify the momentum exchange parameter $c_{\alpha,\beta}$:

$$c_{\alpha,\beta} = \frac{3}{4} \frac{C_D}{d_P} \varepsilon_\beta \rho_\alpha |\mathbf{u}_\beta - \mathbf{u}_\alpha| \tag{2.12}$$

The friction factor C_D in eqn. 2.12 can be calculated from the particle Reynolds number using correlations appropriate for the flow regime; for a survey of drag correlations see e. g. [22]. Table 2.1 shows for the system of water, air and Plexiglass (Polymethyl-Methacrylate, PMMA) particles under consideration [31, 32] the flow parameters (bubble rise velocity, particle settling velocity) and resulting Reynolds numbers for bubbles and particles.

Table 2.1: Calculation of bubble and particle Reynolds numbers; values of $u_{B,\infty}$ and $u_{PMMA,\ settling}$ taken from [31]

Dispersed phase	μ_α	ρ_α	Diameter in Re	Velocity in Re	Re
Air	10^{-3} Pa s	1000 $\frac{\text{kg}}{\text{m}^3}$	0.008 m	$u_{B,\infty} = 0.23\ \frac{\text{m}}{\text{s}}$	1840
PMMA	10^{-3} Pa s	1000 $\frac{\text{kg}}{\text{m}^3}$	0.003 m	$u_{PMMA,\ settling} = 0.109\ \frac{\text{m}}{\text{s}}$	327

At a Reynolds number of 327, the PMMA particles fall into the viscous flow regime where the drag coefficient can be calculated from the following correlation [52]:

$$C_D = \frac{24}{\text{Re}} (1 + 0.1 \cdot \text{Re}^{0.75}) \tag{2.13}$$

With a higher Reynolds number of 1840, the bubbles are already within the range of validity of the Newton or inertial flow regime where the friction factor becomes independent of the Reynolds number:

$$C_D = \text{constant} = 0.44 \tag{2.14}$$

2.2.3.2 Momentum Exchange between two Dispersed Phases

In three-phase flow with dispersed gas and solid phases, direct interactions between the two dispersed phases have to be considered in addition to the indirect interactions with the continuous phase as an intermediate; not much attention has been paid to this point so far. Koh et al. [57] have investigated into bubble-particle collisions in flotation devices by determining kinetic

relationships for the probability of such collisions, the probability of attachment of particles to bubbles and the probability of the particle detaching from the bubble again. In their calculations, however, they considered liquid and solid phase as one slurry phase leading to a simplified two-phase model. Padial et al. [88] have included direct interactions into their model for an airlift loop reactor; their modeling is based on the assumption that the same drag laws can be applied as with the liquid-solid or liquid-gas interactions (i. e. assuming the gas phase to be continuous).

In this work, three simplified approaches have been developed and tested. They will be presented in a manner of increasing model complexity, starting with introducing constant sink or source terms into gas and solid momentum balance and ending with a slip-velocity based model developed from the approach presented by Padial et al. [88]. Implementation of these models into the appropriate momentum balances (eqn. 2.4 written for gas and solid phase, respectively) took place by means of additional body forces (see also section 2.2.7) which were specified by user-supplied Fortran-subroutines. Results of sample calculations with these three models are compared in section 3.2.1.

Interaction Modeling with Constant Source Terms

The most simple approach to modeling the acceleration exerted on the solid particles by the gas bubbles consists of including a constant sink term into the gas phase momentum balance and a constant source term into the solid phase momentum balance. The momentum exchange terms $M_{\beta,i}$ in eqn. 2.4 are then complemented with the following direct momentum exchange terms for the gas and solid phase, respectively:

$$M_{g,i,d} = c_{g,s,c} \tag{2.15}$$

$$M_{s,i,d} = -c_{g,s,c} \tag{2.16}$$

These terms need only to be included for the main flow direction, i. e. the vertical velocity component. The value of the interaction constant $c_{g,s,c}$ has been determined by fitting computational results to measurement data from the work by Dziallas [31] and Dziallas et al. [32] for the model system of air, deionized water and Plexiglass (PMMA) particles. It has been set constant to a value of 1796.5 N/m^3 during all calculations using this model.

The greatest advantage of this model is that it shows no adverse effects on solution convergence and numerical stability. A serious shortcoming lies in the fact that since local phase holdups are not included in the source terms, this model may show non-physical effects. If for example a grid cell contains a high gas fraction and only little solid, the constant exchange term will mean that only little momentum per volume of gas is taken from the gas phase but a very large amount of momentum per volume of solid is added to the solid phase.

Interaction Modeling with Hold-up Dependent Source Terms

A more refined approach to modeling direct interactions between gas and solid phase includes local gas and solid holdup into the momentum exchange terms. In comparison to the model with constant momentum sink and source terms presented above, this refinement means that momentum conservation is not only ensured on a global, reactor-wide scale but also for every single grid cell. Interphase forces are again included into gas and solid momentum balances (given in general formulation in eqn. 2.4) as additional body forces (source terms). The additional terms complementing the $M_{\beta,i}$ in eqn. 2.4 take on the following shape for the gas and solid momentum balance, respectively:

$$M_{g,i,d} = c_g \cdot \varepsilon_g \tag{2.17}$$

$$M_{s,i,d} = -c_s \cdot \varepsilon_s \tag{2.18}$$

The gas phase exchange coefficient c_g has to be prescribed by fitting modeling results to measured local solid holdups taken from [31, 32]. The value obtained in this way has to be kept constant during all three-phase calculations carried out with this model. The solid phase exchange coefficient c_s can then be determined by setting eqns. 2.17 and 2.18 to be equal:

$$c_s = c_g \cdot \frac{\varepsilon_g}{\varepsilon_s} \tag{2.19}$$

The gas and solid volume fractions in this case are local values which are readily available during the calculations; since they are not constant, the coefficient c_s will not be constant either but vary from grid cell to grid cell.

Interaction Modeling with Slip-Velocity Dependent Source Terms

Further model refinement calls for an inclusion of the slip velocity between gas and solid phase into the momentum exchange terms, giving the modeling strategy a heading towards a real drag-law formulation. The approach developed here is based on the work by Padial et al. [88] but includes some simplification and parameter fitting. Taking eqn. 2.11 (interactions between continuous and dispersed phase) as a starting point, the direct momentum exchange terms complementing the $M_{\beta,i}$ in eqn. 2.4 take on the following shape for the gas and solid momentum balance, respectively:

$$M_{g,i,d} = \frac{3}{4}\frac{c_{g,s}}{d_P}\varepsilon_s\rho_g \underbrace{|\mathbf{u_s} - \mathbf{u_g}|}_{u_{slip,g,s}}(u_{s,i} - u_{g,i}) \tag{2.20}$$

$$M_{s,i,d} = -\frac{3}{4}\frac{c_{g,s}}{d_P}\varepsilon_s\rho_g \underbrace{|\mathbf{u_s} - \mathbf{u_g}|}_{u_{slip,g,s}}(u_{s,i} - u_{g,i}) \tag{2.21}$$

These terms are included into the momentum balances for all three spatial directions. The particle diameter d_P in this case was fixed to a value of 3 mm, the gas density ρ_g was assumed constant at 1.22 kg/m^3. Fitting parameter was the combination of $c_{g,s} \cdot u_{slip,g,s}$, the value of which was – as with the above models – determined by fitting modeling results to measured local solid holdups taken from [31, 32] and was set constant to 118 m/s during all calculations with this model. The value of this parameter may not be physically interpreted as a settling velocity but merely is a result of the numerical parameter fitting lumping together all possible interaction effects.

2.2.4 Turbulence Modeling

As has been mentioned before, turbulence modeling is of crucial importance for the correct description of multiphase flows in CFD modeling. Several authors have compared laminar and turbulent two-phase flow computations only to find that in the laminar case, the calculated flow structure will not agree with measurements even at low velocities and gas holdups [93, 109]; moreover, the computed laminar liquid flow fields showed more detailed eddy structures with decreasing mesh width (for more details on grids see section 2.2.5). Grid size dependency is very unwanted in CFD calculations; the implementation of turbulence models can reduce these effects by accounting for the sub-grid size eddy dissipation phenomena that in the laminar case would have to be computed explicitly making a very small mesh width and thus huge computational demand unavoidable.

The identification of turbulence phenomena in multiphase flow started more than 2 decades ago. Brauer [11] gave one of the first surveys of different turbulence sources and formulations. His qualitative discrimination of turbulence production types for multiphase flow lists the following:

- Reynolds turbulence: Turbulence intensity is defined from fluctuational velocities as in the single-phase case [120]; this holds for multiphase flows as well, but other effects will have to be superimposed.
- Interface turbulence: This kind of turbulence is due to surface tension differences at an interface that occur when mass transfer takes place at the interface.
- Deformation turbulence: This turbulence is induced by stochastic motions of bubble surfaces.
- Swarm turbulence: This turbulence type accounts for interactions of particles or bubbles moving in a swarm [102, 121].

The experimental discrimination of turbulence contributions of the effects described above is rather tedious. Thus, for the inclusion of turbulence effects into single phase and multiphase CFD models, a different approach has been used. Over the years, many models for the inclusion of turbulence effects into single-phase CFD calculations have been developed [98, 126]; some of these

have only recently been adapted to multiphase flow situations. All turbulence considerations will only deal with the continuous liquid phase; dispersed gas and solid phase are computed laminar.

Turbulence modeling in general starts from the observation that in turbulent flow velocities can be decomposed into mean and fluctuating parts:

$$\mathbf{u} = \bar{\mathbf{u}} + \mathbf{u}' \tag{2.22}$$

Since continuity equation and momentum balance have to be written in terms of mean velocities, these have to be determined using Reynolds averaging [29] over a time scale δt which has to be large compared to the time scale of turbulent fluctuations but sufficiently small compared to the time scale of transient processes that are supposed to be modeled:

$$\bar{\mathbf{u}}(\mathbf{t}) = \frac{\mathbf{1}}{\delta \mathbf{t}} \int_{\mathbf{t}}^{\mathbf{t}+\delta \mathbf{t}} \mathbf{u}(\tau) \mathrm{d}\tau \tag{2.23}$$

Introducing the momentary velocity $\mathbf{u}$ as given in eqn. 2.22 into the laminar momentum balance as shown in non-vectorial notation in eqn. 2.3, additional stress terms (Reynolds stresses $\overline{u_i u_j}$ where i and j give the directions x, y and z in tensor notation) appear in the turbulent momentum equation which usually are not solved directly but have to be modeled. A variety of models has been developed the most popular of which will be introduced in the subsequent sections briefly.

2.2.4.1 Overview of Common Turbulence Models

Starting with single-phase flow settings, historical development of turbulence models for CFD purposes may roughly be organized into a family tree as given in Fig. 2.1.

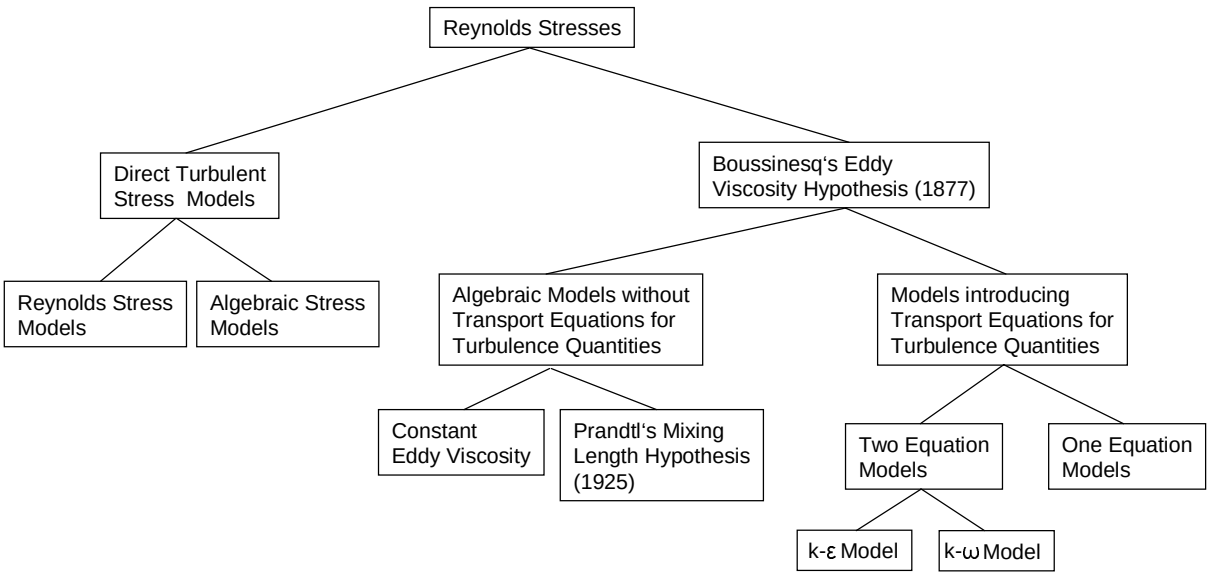

Figure 2.1: (Incomplete) Family tree of common turbulence models, based on [45, 98, 126]

As the oldest approach to modeling Reynolds stress terms $\overline{u_i u_j}$, Boussinesq's Eddy-viscosity concept starts from the assumption that as with the viscous stresses in laminar flow, turbulent stresses are proportional to the mean flow velocity gradients [98]. Since in the laminar case the proportionality constant between stress and velocity gradient is named viscosity, Boussinesq's hypothesis introduces a turbulent viscosity. However, this is not a fluid property but depends on the local turbulence state, thus additional models are needed for the computation of turbulent viscosity. With turbulent viscosity assumed to be a scalar, only isotropic turbulence can be modeled by Boussinesq's hypothesis and the models based on it.

The most basic formulations for turbulent viscosity assume that it is constant for the whole flow domain under consideration or that it (as e. g. in Prandtl's mixing length hypothesis) depends only on the local velocity gradient [98]. The first approach clearly can not account for any spatial variations in turbulence and thus has not gained any importance. The second approach has proved viable only for limited applications since it does not account for the transport of turbulence quantities through the flow domain which obviously is not physically reasonable (e. g. eddies generated in the wake of a body are transported downstream and certainly do show effects far from the location of their creation).

In order to account for downstream effects, turbulence models introducing transport equations for turbulence quantities have been formulated which may be grouped as follows:

- One-Equation Models: These models give up the idea of a constant proportionality factor between turbulent viscosity and velocity gradient as introduced by Prandtl's mixing length hypothesis and revert to determining the local value of this factor from a transport equation. The most reasonable quantity to determine this factor from is the local kinetic energy k of the turbulent motion. Therefore, a transport equation for k has been introduced.

- Two-Equation Models: With these models, the length scale that describes the size of the largest eddies is subjected to a transport equation as well. Reason for this can be found in the fact that for example eddies generated at a grid are transported downstream where their size will very much depend on their initial size. Transport equations for the length scale itself are, however, not very common; instead, other quantities like for example turbulent dissipation are transported.

  - k-ε Model: Here, turbulent dissipation ε is transported in addition to turbulent kinetic energy k. This is due to the fact that the size of the eddies strongly depends on dissipation which eliminates the smallest eddies thus effectively increasing the average eddy size. Since the k-ε model has proved to be the most versatile especially with respect to multiphase extensions, it has gained large popularity and has been implemented for this project as well (see section 2.2.4.2 for more details).

– k-ω Model: This model is implemented especially at low Reynolds numbers; it still solves a transport equation for turbulent kinetic energy k but replaces the equation for turbulent dissipation ε with a transport equation for the turbulence frequency $\omega = \varepsilon/k$ [126].

In order to account for effects like anisotropy or rotational flow that cannot be captured correctly by models based on Boussinesq's Eddy Viscosity Hypothesis, direct models for the individual Reynolds stresses have been implemented [98]:

- Reynolds Stress Models: These models implement direct transport equations for the turbulent stresses $\overline{u_i u_j}$. An exact form of this transport equation may be derived analytically from the Navier-Stokes equations. However, this partial differential equation again includes many terms which cannot be solved directly but have to be approximated by models. Approaches of this kind have led to turbulence models with 15 or more fitting parameters [98]. Erdal et al. [33] have compared calculations with a Reynolds Stress model and the k-ε model for two-phase flow in a hydrocyclone; they found that the additional expense in computation did not yield improved results over the k-ε model.

- Algebraic Stress Models: In this class of models, the partial differential transport equations of the Reynolds Stress model have been replaced with algebraic relations by neglecting or approximating the gradient terms. This is advantageous especially with respect to numerical efficiency but yields satisfactory results only for a limited number of applications.

2.2.4.2 The k-ε Turbulence Model

Even though it can only model isotropic turbulence, the k-ε model is by far the most wide-spread and accepted turbulence model [93, 109, 113, 126]. As a two-equation model, it introduces two additional transport equations into the calculation, one for the computation of turbulent kinetic energy and one for turbulent dissipation. From these two additional variables, a third equation serves to calculate local turbulent viscosity. In multiphase flow, these equations are usually only implemented for the continuous phase. Because of its wide acceptance in the scientific community, the k-ε turbulence model has been chosen for inclusion into this project.

Since in the computations carried out here the liquid phase is the continuous one, the conservation equation for the liquid turbulent kinetic energy k may be written down as follows:

$$\begin{aligned} &\frac{\partial}{\partial t}(\varepsilon_l \rho_l k) + \frac{\partial}{\partial x_i}(\varepsilon_l \rho_l u_{l,i} k) \\ -\frac{\partial}{\partial x_i}&\left(\varepsilon_l \left(\mu_{l,lam} + \frac{\mu_{l,turb}}{\sigma_k}\right)\frac{\partial k}{\partial x_i}\right) \quad = \quad \varepsilon_l (G - \rho_l \varepsilon) + S_{l,k} \end{aligned} \tag{2.24}$$

Here, G is a turbulence production term and $S_{l,k}$ is a source term; both of these may be used to e. g. implement turbulence effects of bubbles or particles but are not considered here and thus

set to zero. The conservation equation for the liquid turbulent dissipation ε takes on the following shape:

$$\begin{aligned} &\frac{\partial}{\partial t}(\varepsilon_l \rho_l \varepsilon) + \frac{\partial}{\partial x_i}(\varepsilon_l \rho_l u_{l,i} \varepsilon) \\ -\frac{\partial}{\partial x_i}&\left(\varepsilon_l \left(\mu_{l,lam} + \frac{\mu_{l,turb}}{\sigma_\varepsilon}\right)\frac{\partial \varepsilon}{\partial x_i}\right) = \varepsilon_l \frac{\varepsilon}{k}(C_{\varepsilon 1} G - C_{\varepsilon 2}\rho_l \varepsilon) + S_{l,\varepsilon} \end{aligned} \tag{2.25}$$

The source term $S_{l,\varepsilon}$ in eqn. 2.25 is set to zero as with $S_{l,k}$ in eqn. 2.24. The effective liquid dynamic viscosity μ_α in eqn. 2.3 is combined for the turbulent case from a laminar and a turbulent part:

$$\mu_\alpha = \mu_{\alpha,lam} + \frac{\mu_{\alpha,turb}}{\sigma_k} \tag{2.26}$$

Where the turbulent viscosity $\mu_{\alpha,turb}$ is computed from:

$$\mu_{\alpha,turb} = C_\mu \rho_l \frac{k^2}{\varepsilon} \tag{2.27}$$

In effect, this means that with the k-ε model, three additional unknowns (k, ε and $\mu_{\alpha,turb}$) and three equations (two partial differential equations, one algebraic equation) have been introduced into the calculation yielding a closed model.

In the shape presented above, the k-ε model does not account for particle- or bubble induced turbulence yet. These effects can be included by defining additional fluctuational velocities due to bubble presence or by introducing additional source terms. For modeling particle- or bubble-induced turbulence, several models have been suggested:

- Sato's Eddy Viscosity Model for bubble-induced turbulence [100]: This model assumes that in two-phase gas-liquid flow, the liquid velocity can be decomposed according to an extension of eqn. 2.22 into a mean velocity $\bar{\mathbf{u}}$, a fluctuational velocity due to inherent liquid turbulence $\mathbf{u}'$ and an additional superimposed fluctuational velocity $\mathbf{u}''$ due to the presence of bubbles in the flow:

  $$\mathbf{u} = \bar{\mathbf{u}} + \mathbf{u}' + \mathbf{u}'' \tag{2.28}$$

  Introducing this definition of $\mathbf{u}$ into the laminar momentum balance as shown in non-vectorial notation in eqn. 2.3 yields an equation that in addition to the common Reynolds stresses $\overline{u_i u_j}$ contains new terms due to the bubble effects. These new terms again have to be modeled appropriately, aiming at an additional component in the turbulent viscosity expression.

- Turbulent Dispersion: This model introduces additional source terms into the continuity equation for the continuous and dispersed phases (eqn. 2.2) thus describing diffusional motion due to turbulence; it can be used in combination with e. g. the k-ε model. Modeling formally follows Fick's first law of diffusion by assuming proportionality of the source term to volume

fraction gradient of the respective phase and a dispersion coefficient [51, 93]. In the literature, this effect has often been found to be hidden by larger numerical dispersion due to coarse computation grids [53, 93].

- Direct Numerical Simulation: As described on page 7, Direct Numerical Simulation (DNS) does not model turbulence terms in the Navier-Stokes equations but actually solves them directly. In order to cover turbulence effects completely, grid size for the numerical solution procedure has to be much smaller than the smallest turbulence eddies. Introduction of particle turbulence effects is rather straightforward but has so far only been tested at very low particle volume fractions because of the prohibitive computational demand associated with this strategy [8, 24, 126]. No results of DNS have so far been used to improve e. g. the k-ε model with respect to particle effects.

- Large Eddy Simulation (LES) as described on page 7 only calculates the largest turbulence eddies directly and uses models for the sub-grid scale effects. This strategy also accounts for particle effects but underlies similar limitations as DNS with respect to the particle volume fraction that can be considered [9, 126].

For the modeling calculations performed as part of this project, none of the above models for particle- or bubble-induced turbulence has been included. Test calculations have been performed with Sato's eddy viscosity model for bubble-induced turbulence [100] but did not yield any improvement in results over the standard case; thus, particle- and bubble-induced turbulence have been neglected for the sake of model simplicity and convergence. Turbulent dispersion has been reported in the literature to be of minor influence especially with computations on coarse grids since numerical dispersion can not be neglected [93]; thus, turbulent dispersion has been disregarded as well since all calculations of this project where performed on coarse grids.

Summing up, the parameters in the k-ε model have been chosen with their standard values as given in the literature (e. g. [93]) and may be seen from table 2.2.

Table 2.2: Standard values of parameters used in the k-ε turbulence model as implemented here [83, 93]

C_μ	$C_{\varepsilon 1}$	$C_{\varepsilon 2}$	σ_k	σ_ε	κ
0.09	1.44	1.92	1.0	$\frac{\kappa^2}{(C_{\varepsilon 2}-C_{\varepsilon 1})\sqrt{C_\mu}}$	0.4187

2.2.5 Geometry Grid Generation

Correct modeling of the flow domain is of crucial importance for the numerical solution procedure in CFD calculations. Since literature research and own experience showed that two-dimensional calculations were not viable for the computation of local velocities and phase holdups in multiphase flows [61, 81, 109], a fully three-dimensional bubble column model had to be generated. The numerical solution procedure implemented here (Finite-Volume-Scheme, see section 2.2.7) makes a discretization of the flow domain into sufficiently small grid cells necessary. "Sufficiently small" in this context means that the mesh width (or grid cell size) must not be too large in order not to adversely affect convergence; on the other hand, too small grid size yields large numbers of cells for which the discretized equations have to be solved leading quickly to an immense computational demand with respect to processor time and memory usage: In a three-dimensional calculation, reducing grid cell size to one half its original value means an eightfold increase in the number of equations to be solved – which is proportional to computational demand. For the bubble column under consideration here, the values given in table 2.3 have proved to be a reasonable compromise between accuracy and computational demand.

Table 2.3: Reactor geometry used for the CFD calculations of this project

Bubble column diameter	0.63 m
Bubble column height	5.0 m
Average mesh width / grid cell edge length	5.9 cm
Approx. number of grid cells	13,600
Typical computation time (800 MHz AMD-K7)	48 hours

With an average cell edge length of 5.9 cm, this grid is still extremely coarse, keeping in mind that bubbles in the calculations are assumed to have a diameter of only 8 mm. Therefore, great care has to be taken in mesh generation. Due to the limitations of the solver, all grid cells have to be topologically cube-shaped (having 6 surfaces); no arbitrary shapes are allowed. In addition, the grid has to be regular, i. e. it must be guaranteed that every cell surface connects to only one neighbouring cell surface. In addition, no geometry distortions may occur between neighbouring cells; this leads to the formulation of a well structured nine-block grid for the bubble column geometry used here. All grid generation was carried out using the commercial pre-processor CFX-Build 4.3 [83]. Fig. 2.2 shows as an example the bubble column geometry with the nine-block grid structure used for modeling the plate sparger.

From Fig. 2.2 it can be seen that the actual grid size varies over the reactor cross section and is smallest in the reactor center. This can not be avoided even if a finer grid at the reactor edge

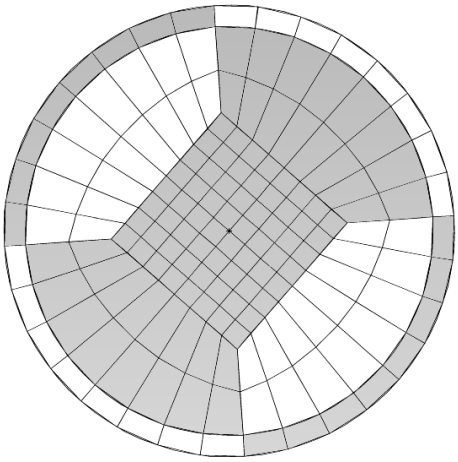

Figure 2.2: Nine-block grid structure for a three-dimensional bubble column geometry with plate sparger

would be more desirable due to the above mentioned demand that the grid be regular, i. e. every grid cell surface must have only one neighbour.

Test calculations with finer grids have shown that no improvement in convergence and accuracy of the results could be achieved. Increasing cell number from 13,600 to 22,880 and 50,895 only yielded massive increases in computation time but did not significantly change modeling results or bring about a better fit to measurement results. In agreement with literature results [92], reducing time step width from 0.4 s to 0.1 s did not change the time averaged results significantly either but only caused a fourfold increase in computation time demand.

As in the experiments that build the base for these modeling calculations [31, 32], three types of spargers were considered, namely plate, ring and single nozzle sparger. Sparger modeling was done via patches at the bottom of the bubble column. This means that a section of the reactor bottom area was defined as gas inlet and an inlet velocity was prescribed for this area. While this is a valid approximation for plate sparger and central nozzle, it can only to a limited extent model the ring sparger that was used during measurements: The ring was mounted inside the bubble column approximately 70 mm above the reactor bottom and released the air at its bottom side inducing local downflow thus yielding efficient solid fluidization. However, due to the coarse grid, this effect could not be included into the CFD calculations. With the plate sparger as shown in Fig. 2.2, it was of crucial importance to model the inlet patch as somewhat smaller in diameter than the actual reactor diameter since otherwise severe convergence problems could occur (no stable downflow would develop at the reactor wall). The central nozzle could not be modeled as circular but due to the coarse grid had to be considered as rectangular covering the four center cells in Fig. 2.2. Table 2.4 shows the sparger geometries for the three investigated cases of plate, ring sparger and central nozzle.

Table 2.4: Sparger geometries used for the CFD calculations of this project

Reactor diameter	0.63 m
Plate sparger diameter	0.57 m
Ring Sparger inner diameter	0.42 m
Ring sparger outer diameter	0.48 m
Central nozzle edge length	0.053 m

2.2.6 Initial and Boundary Conditions

In order to obtain a well-posed system of equations, reasonable boundary conditions for the computational domain have to be implemented. With the three-dimensional calculations carried out in this project, no symmetry conditions as with 2D models were needed. At the walls, no-slip boundary conditions were implemented for all phases; for liquid and solid phase, reactor bottom and top were considered as walls as well, while the gaseous phase was allowed to enter through a patch at the reactor bottom the shape of which depended on the sparger geometry that was supposed to be modeled (see section 2.2.5).

Attention has to be paid to the correct choice of inlet gas velocity and inlet gas holdup. Due to the coarse grid, e. g. the plate sparger can not be modeled with all its holes but has to be modeled as a flat surface where a constant normal gas velocity and gas holdup can be prescribed. Since the model's sparger area is large, the gas velocity is rather low. In reality, however, the local gas velocity at the small sparger holes is substantially higher leading to a better fluidization of solid particles than in the model case. With the central nozzle, the original diameter could not be modeled either due to the coarse grid; it had to be modeled as a square with edge length corresponding to twice the actual grid size in the reactor center. Thus, in sparger modeling additional assumptions have to be made; in special, local gas and solid holdup at the sparger are decisive parameters which have to be chosen from experience and from comparison of computational to measurement results of solid fluidization and have to be prescribed for the calculations. Here, results from Dziallas et al. [31, 32] have been taken for parameter validation. Table 2.5 shows for all three sparger types under consideration a comparison of free sparger cross-sectional areas.

From table 2.5 it can be seen that with the measurements, the central nozzle actually had the largest free cross-sectional area while with the computations, it had the smallest of all three sparger types. This model-implicit error can only to a limited extent be compensated by selecting inlet gas holdup appropriately; really realistic sparger modeling could only be achieved on much finer computational grids where e. g. the plate sparger holes could be modeled one by one. The actual gas velocity at the inlet as given on the bottom line of table 2.5 was computed from the

Table 2.5: Comparison of free sparger cross-sectional areas for measurement [31] and modeling cases

Sparger Type	Plate Sparger	Ring Sparger	Central Nozzle
Hole diameter (measurements)	1 mm	4 mm	22 mm
Number of holes (measurements)	335	12	1
Cross-sectional area (meas.)	$0.2631 \cdot 10^{-3}\text{m}^2$	$0.1507 \cdot 10^{-3}\text{m}^2$	$0.3801 \cdot 10^{-3}\text{m}^2$
Cross-sectional area (model)	0.255m^2	0.042m^2	$2.809 \cdot 10^{-3}\text{m}^2$
Chosen gas holdup at sparger	5 Vol.-%	5 Vol.-%	100 Vol.-%
Chosen solid holdup at sparger	10 Vol.-%	10 Vol.-%	0 Vol.-%
Modeling gas inlet velocity for a superficial gas velocity of 0.02 m/s	0.3258 m/s	1.980 m/s	1.480 m/s

desired superficial gas velocity in the following manner:

$$u_{g,inlet} = u_{G,0} \cdot \frac{1}{\varepsilon_{g,inlet}} \cdot \frac{A_{Reactor}}{A_{Sparger}} \cdot \frac{p_0}{p_{inlet}} \tag{2.29}$$

Since the superficial gas velocity is set with respect to the upper edge of the reactor, a pressure correction term $p_0/p_{inlet} = 1.0$ bar/1.5 bar has been introduced which is assumed to be constant for all calculations even if gas or solid holdup change and subsequently the actual pressure at the reactor bottom is not really a constant. This pressure correction is also used to compute the density of air at the reactor bottom.

At the reactor top, a special degassing boundary was set up where air and excess liquid or solid were allowed to leave the reactor ("overflow"). Transient calculations started from assuming fully fluidized state with an integral gas holdup of 5 Vol.-% and integral solid loading according to the desired value in the calculation (i. e. 0, 5 or 10 Vol.-%).

2.2.7 Numerical Solution Procedure

For an efficient numerical solution of the equation system resulting from all the modeling described above, a finite volume discretization scheme [40] is employed. As has been explained above, the transient equations had to be solved thus one has to start considerations on the solution procedure by picking an appropriate time increment and calculation time. As with the spatial grids described in section 2.2.5, limited computational resources lead to a rather coarse temporal resolution of the calculations. For all calculations presented in this report (except where marked differently), a time increment δt of 0.4 s and a total computed time of 320 s have been found to give a reasonable compromise between accuracy and computation time demand; in the literature it has been reported

that even after 1400 s of computed time, perfect rotational symmetry of time-averaged velocity and gas holdup profiles could not be achieved [92].

A simultaneous solution of the discretized equation system under consideration here is not viable due to the high degree of non-linearity of the equations. Thus, a sequential approach has to be chosen where each of the balance equations 2.2 to 2.4, 2.24 and 2.25 is discretized, linearized and solved for one variable. In this approach, every variable is considered to belong to one equation, e. g. would gas volume fraction belong to gas mass balance as in eqn. 2.2 and gas velocity in x-direction would belong to gas momentum balance in x-direction (eqn. 2.4). In a three-phase calculation, this yields twelve equations for the twelve unknown volume fractions and velocity components plus two equations for turbulent kinetic energy and dissipation plus one equation for turbulent viscosity plus the ideal gas equation for calculating gas density as compressible, leaving only pressure as remaining unknown. Since no transport equation is solved for pressure, a special treatment for the calculation of pressure has to be introduced; in this work, the SIMPLE scheme ("Semi-Implicit Method for Pressure-Linked Equations")[19, 91] has been used where computation of the discretized balance equations is started with an estimated pressure field which is subsequently corrected iteratively to fulfill momentum and mass conservation.

As an iterative solution procedure for the discretized transport equations, an algebraic multigrid (AMG) solver has been used [12, 20, 39, 125]. This has proven especially advantageous since the AMG solver is capable of an internal grid adaptation (coarsening the grid where this is possible without loss of accuracy) delivering high convergence rates. In all the calculations presented here, convergence to the desired accuracy was achieved in 20 or less iteration steps.

Time averaging was started at 20 s of computed time and was continued to the end of the calculation (computed time 320 s). Fig. 2.3 shows for sample calculations that after 20 s of computed time, integral gas holdup has reached more than 90 % of its final value for all superficial gas velocities; thus, time averaging from this point on will deliver reasonable results without perturbations due to start-up effects. Similar results have been found with all the model variations described above.

Computed integral solid holdup showed a tendency to decrease with time during all calculations carried out in this project even though no outlet for solid was specified. Fig. 2.4 shows for the same settings as in Fig. 2.3 that especially at higher superficial gas velocities this process continues for up to 80 s of computed time yielding a solid loss of more than 12 % of the initial content.

Reason for this unwanted behaviour may probably be found in the coarse grid that has been used during these calculations which makes it hard for the numerical solution algorithms to ensure absolute mass conservation. However, test calculations on finer grids (22,880 and 50,895 instead of 13,600 cells) did not yield any improvement with respect to solid holdup decreasing with computed time; actually, at a cell number of 50,895 and a superficial gas velocity of 0.09 m/s, solid loss was even higher than in corresponding runs with the coarser grids as may be seen from table 2.6.

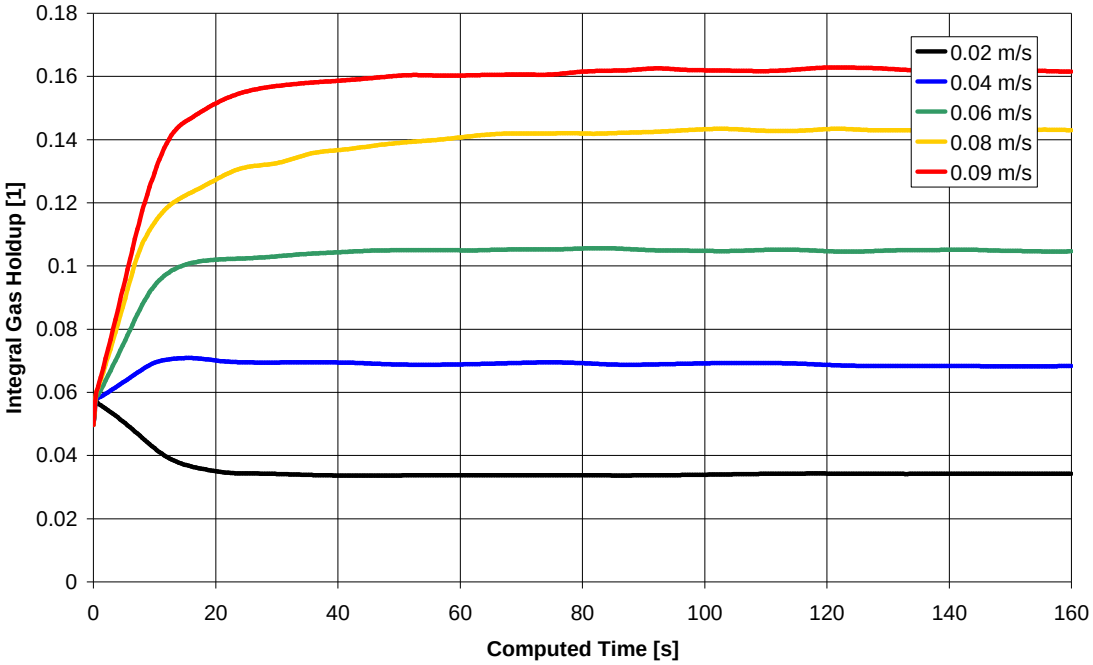

Figure 2.3: Calculated integral gas holdup over computed time for different superficial gas velocities; values for this example have been taken from the calculations shown in Fig. 3.14 (plate sparger, solid loading 10 Vol.-%).

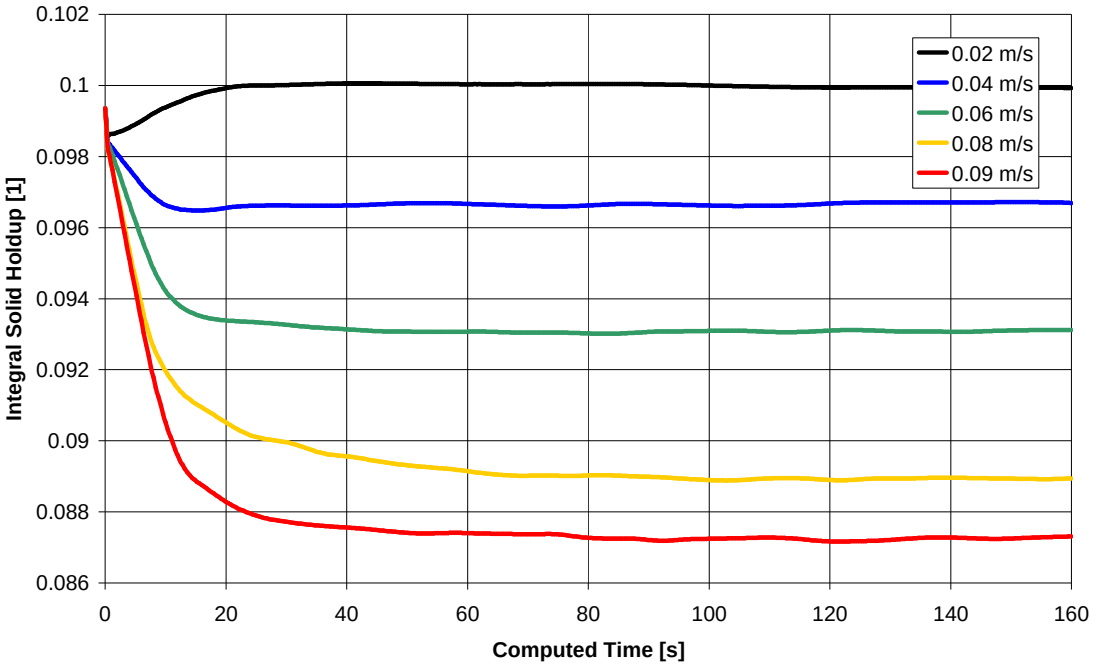

Figure 2.4: Calculated integral solid holdup over computed time for different superficial gas velocities (settings as in Fig. 2.3); initial value which was supposed to remain constant over the calculation was 10 Vol.-%.

Table 2.6: Solid loss during calculations (settings as in Fig. 2.3, 320 s of computed time, superficial gas velocity 0.09 m/s, initial solid loading 10 Vol.-%)

Number of grid cells	13,600	22,880	50,895
Steady state solid holdup [Vol.-%]	8.7	8.6	8.4

Reducing time step width from 0.4 s to 0.1 s did not reduce solid losses either. Another possible reason for the solid loss may be found with the degassing boundary at the reactor top which has to let a certain amount of liquid and solid escape from the reactor to account for the increase of dispersion level in the column and probably is somewhat "leaky". When solid density is increased, the effect may even switch its sign and a slight increase in solid holdup can be observed.

All calculations were performed using the commercial solver CFX-4.3 from AEA Technology [83] on PC workstations and an SGI Power Challenge. A typical run with the 13,600 cell grid took about 48 hours of processor time and 80 MBytes of Memory on an 800 MHz AMD-K7 workstation. Non-standard model additions like calculation of integral dispersed phase holdup, ideal gas law for compressibility considerations or direct momentum exchange between gas and solid phase (see section 2.2.3.2) were implemented by means of user-defined Fortran subroutines. At this point it is important to mention that forces resulting from direct gas-solid interaction models have to be included into the calculations as additional body forces and not as momentum sources. Even if this means the same in a physical sense, the numerical treatment that is applied to the body forces includes additional steps to suppress oscillatory behaviour which are not applied to the source terms [83].

2.3 Recent Results of Measurement Technique Developments

For the verification of CFD modeling results, measurements of local dispersed phase holdups and local liquid velocities are needed. Therefore, the dynamic development in the field of multiphase CFD in the last years has boosted new developments in the field of multiphase flow measurement techniques as well. Before the advent of detailed local modeling techniques, measurement methods were mostly limited to overall or spatially averaged parameters which were needed for empirical scale-up correlations. Good surveys of these methods have been given by Schügerl et al. [104] and Onken and Buchholz [86]. New techniques are mostly aimed at high spatial and temporal resolution of measurement data. A brief synopsis of recent developments in multiphase flow measurements may be found in [94].

2.3.1 Determination of Local Dispersed Phase Holdups

Measurement techniques for local dispersed phase holdups can be divided mainly into invasive and non-invasive techniques. Furthermore, a dividing line can be drawn between methods which only measure gas or solid holdup and methods which simultaneously determine both dispersed phase holdups. A short survey of methods common in scientific applications should list the following:

- Needle conductivity probes for the determination of local gas holdup: This technique uses glass needles with thin wires at the tip which are connected to a conductivity measurement device. When a rising bubble contacts the needle tip, conductivity will for a short period decrease to zero; these signals can be evaluated to determine the time-averaged local gas holdup [1, 16, 92]. A more refined version of this technique uses 4- and 5-point microelectrodes which additionally allow for the determination of bubble rise velocity and direction [14, 50, 115]. Due to their fragile glass body, these probes are only of limited use when solids are present in the flow.

- Fiberoptical probes for local gas holdup determination: These probes measure light reflection and refraction in gas-liquid or gas-solid flow and compute the local dispersed phase holdup and one-dimensional particle or bubble velocity [75, 118]. While they are operable at solids loadings up to 60 Vol.-%, they have only scarcely been used in three-phase flow due to the difficult signal discrimination. Schweitzer et al. [106] have described measurements of radial gas holdup profiles in bubble columns taken with dual fiber optic needle probes. They found that the presence of solid does not interfere with the measurements and that moreover this measurement technique can even be employed for the study of void fractions in fluidized beds.

- Sampling probes for the measurement of local solids concentration: This measurement technique taps the reactor system at a desired position and determines dispersed phase content either online or offline [4, 82]. While the simplicity of the method makes it attractive, its downside lies in strong disturbances of the flow field due to the bypass stream.

- Ultrasonic technique for solid holdup determination: Soong et al. [114] presented a method which uses measurements of velocity and attenuation of sound to determine solid holdup in three-phase flows. So far, only radially-averaged solid holdup values can be determined with the transmitter and receiver flush-mounted to the reactor wall (making this a non-invasive method).

- Tomographic methods for two- and three-phase applications: Initially having been created for medical applications, computer tomography has received increasing interest in multiphase flow applications recently [90, 96, 99, 123, 124]. As an invasive or non-invasive technique,

tomography can be based on different measurement principles such as x-ray, conductivity, ultrasonic or capacitance measurements; in bubble columns, tomography can deliver time-averaged two-dimensional cross-sectional images of local dispersed phase holdup in two- and three-phase systems. So far, however, effort and costs of these measurements are prohibitively high for a more frequent application.

An approach different from all others presented above has been followed in the work of Dziallas et al. [31, 32]. Based on results from Lindert et al. [69, 70] and Kochbeck et al. [56], they developed a combined differential pressure and conductivity respectively time domain reflectometry (TDR) probe with which they were able to simultaneously determine local gas and solid holdups at gas holdups up to 20 Vol.-% and solid loadings up to 10 Vol.-%, aiming at bubble columns operated under conditions relevant in real industrial applications. Measurements taken with this system encompass a complete set of two- and three-phase holdup data for the model system under consideration in the project presented here; therefore, measurement results from Dziallas [31] are taken for the verification of CFD holdup computation as well as for the explanation of liquid flow phenomena determined with the Electrodiffusion measurement technique described below.

2.3.2 Measurement Techniques for Local Liquid Flow Velocities

The determination of local velocities in multiphase flows has been subject to experimental investigation for many years. A large number of measurement principles have been tested in laboratory scale, a few are considered standard for low dispersed phase contents today but so far no reliable system for everyday use in research and industrial application is available [24]. Especially at high dispersed phase contents, most measurement principles fail.

2.3.2.1 Overview: Common Measurement Methods

Measurement principles for the determination of local liquid velocities in multiphase flows include optical, mechanical, thermal and mass transfer effects. In addition, measurement techniques can be divided into invasive and non-invasive methods, as with the holdup measurements techniques described above. A good overview of measurement principles and applications is given by Crowe et al. [24].

Among the optical methods, Laser Doppler Anemometry (LDA) has become a standard widely accepted in multiphase research. As a non-invasive optical measurement technique, LDA is based on the Doppler signals induced by liquid flowing through a control volume generated by two intersecting Laser beams [24]. Main advantage of this method is the complete absence of flow disturbance during measurements; most serious downside is the fact that no measurements can be performed in opaque media or when particles or more than very little gas content is present.

Becker et al. [5, 6] have studied liquid flow structure inside a flat (thickness 0.04 m) laboratory two-phase bubble column using LDA at very low gas flow rates (corresponding to a superficial gas velocity of 0.0016 m/s) and thus very low gas holdup. Due to the high data rate delivered by LDA, they could clearly resolve high-frequency turbulence from low-frequency bubble plume oscillations inside the bubble column. While these results give interesting insight into fundamental turbulence phenomena, they cannot readily be transferred to a technical scale where superficial gas velocity and gas holdup are at least one order of magnitude higher. Even if e. g. Vial et al. [122] have taken measurements at gas holdups of up to 20 Vol.-%, their bubble column had a diameter of only 0.1 m. Pfleger and Becker [92] report a maximum penetration depth of 0.15 m for LDA measurements in two-phase bubbly flows at superficial gas velocities of less than 0.02 m/s corresponding to data acquisition rates as low as 1 Hz and a very long measurement period of up to 1 hour. This implies that high-frequency turbulence measurements are completely out of range.

For simultaneous measurements of liquid and bubble velocities as well as local bubble size distributions, Phase Doppler Anemometry (PDA) has been developed [13]. The model system for the measurements has to be chosen carefully because refraction and reflection have to be known for a correct evaluation and a proper discrimination of bubble and seeding particle signals. An extension of the PDA technique to cover three-phase flows is the so-called Enhanced Phase Doppler Anemometry (EPDA) [10]. This method uses special evaluation algorithms to discern dispersed bubbles and solid particles. For this method to work correctly, optical properties of the dispersed materials like refractive index or extinction coefficient have to be known; this restricts the method's applicability to model systems in reactors of laboratory scale.

Another optical, non-invasive method which not only can determine liquid velocities but also covers bubble or particle motions is known as Particle Image Velocimetry (PIV)[72]. Seeding particles are added to the liquid the motions of which can be traced with high speed video cameras. In comparison to LDA, the control volume for this method is rather large; the video cameras deliver images from a light sheet that has to be projected into the liquid by means of an oscillating Laser beam. Full three-dimensional flow vectors can be obtained using 3D-Scanning-Particle-Image-Velocimetry which uses a non-stationary light-sheet scanning through the reactor volume of interest [15]. The high data rate from the large control volume (or rather control area in two-dimensional measurements) calls for very sophisticated evaluation algorithms and large computational power. By means of a special phase-masking method it is possible to visualize the liquid motion in the wake of a rising bubble at high local and temporal resolution [15, 71, 72]. As with the LDA, this method delivers interesting results for the fine-scale bubble flow phenomena but is not viable at high gas holdups.

A non-invasive method that delivers results even at high gas and solid holdups has been presented by Seeger et al. [107]. X-Ray Particle Tracking Velocimetry (XPTV) uses buoyant seeding particles with a lead core that are supposed to follow the liquid flow closely enough to actually

represent the liquid flow field. The motions of these particles are recorded three-dimensionally by a high-speed X-Ray apparatus (standard device for medical applications) and can be evaluated to deliver the liquid flow field inside the bubble column. Since X-Rays are not subject to dispersion and reflection as visible light, bubbles or solid particles do not interfere with the measurements. For large-scale applications, however, this technique is not viable yet due to the prohibitive costs of the X-Ray setup and the limited size of bubbles columns that can be investigated.

A somewhat similar method which uses radioactively marked tracer particles has been presented by Sanyal et al. [99]. Because of the high safety precautions that have to be taken and the long measurement times (typically 20 hours for one set of data), this method does not seem viable for real-life applications so far.

Invasive measurement methods are often more appropriate for multiphase flows occurring in practical applications. Since these applications often include larger reactor geometries, flow disturbance by a probe can be neglected. With the probe inside the multiphase mixture, measurements can be taken independently from media opacity; still, data evaluation procedures must account for bubble or particle effects on the measurement.

The invasive method that has found the most wide-spread use in multiphase flow is the Constant Temperature Anemometry (CTA)[42, 76, 86, 118]. The measurement probe consists of an electrically heated wire section which is exposed to the fluid flow under investigation. Heat transfer from the wire to the fluid is dependent on the flow velocity; when the electrical current is controlled quickly enough to keep the wire at a constant temperature, the electrical current value gives an information about the momentary flow velocity. This implies that careful calibration procedures have to be followed for every new system that this technique is implemented for; especially the presence of solids leads to a fast degradation of the probe surface making frequent recalibration unavoidable. With split-film probes, even 3D flow vectors can be determined [17].

A method well known from single-phase flow but rarely used in multiphase flow has been presented by Krishna et al. [60]. Their method is based on a modified Pitot tube which measures the difference between local static and total pressure and computes the liquid velocity from the dynamic pressure. Careful purging procedures have to be carried out before each measurement to avoid errors due to bubbles entering the Pitot tube; only one-dimensional velocities can be determined.

2.3.2.2 The Electrodiffusion Measurement Technique

An evolving measurement technique for the two-dimensional determination of liquid flow velocities in dispersed systems even at high gas and solid holdups is the so-called Electrodiffusion Measurement technique (EDM). This method has been developed at the University of Dortmund / Germany [44, 87, 89] and has successfully been implemented at University of Bremen / Germany

[41, 102] for three-phase flows in bubble columns and loop reactors. Hashiba and Kojima [46] have used a similar method and have even suggested an extension of the principle to the measurement of three-dimensional flows [47].

The EDM presented here and used for all liquid flow measurements of this project is – somewhat similar to Constant Temperature Anemometry described above – based on the influence of liquid flow velocity on the mass transfer boundary layer at a silver electrode. A highly constant voltage is applied between measurement electrode (made from thin silver wire) and a reference electrode made from platinum. An increase in liquid flow velocity leads to a decreasing boundary layer thickness resulting in increased mass transfer and electric current at constant voltage. When this system is operated at an appropriate voltage ensuring that diffusion is the limiting factor for the electric current and when careful calibration procedures are followed, three-wire needle electrodes allow for the two-dimensional measurement of liquid flow velocities up to 2 m/s [89]. Bubbles hitting the electrode induce characteristic signals which can be identified and eliminated by a special algorithm which is part of the general data postprocessing routine. Solid particles have no adverse effect on the measurements; actually, the abrasive effect of the particles helps keeping the electrode surface from degenerating thus increasing the unavoidable electrode polishing intervals. Fig. 2.5 shows the EDM three-wire needle electrode as used in this project.

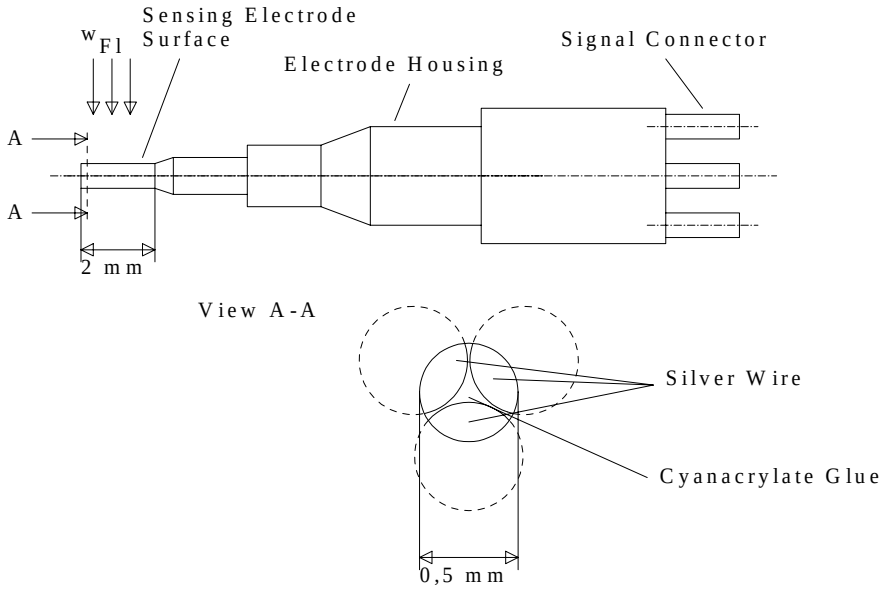

Figure 2.5: Three-film electrodiffusion measurement electrode [87]

The three-film electrode is made from three silver wires glued together with a special Cyanacrylate glue. During calibration, the electrode tip is given its final shape in an iterative procedure of grinding and measuring the electric currents of the 3 wires under defined flow conditions in a calibration canal.

EDM as used here can only resolve two-dimensional flow vector in a plane perpendicular to the

electrode axis. Therefore, in order to resolve axial and radial flow velocities, the electrode has to be mounted inside the bubble column using a special 90° probe. Fig. 2.6 shows the measurement setup with the probe mounted inside the bubble column.

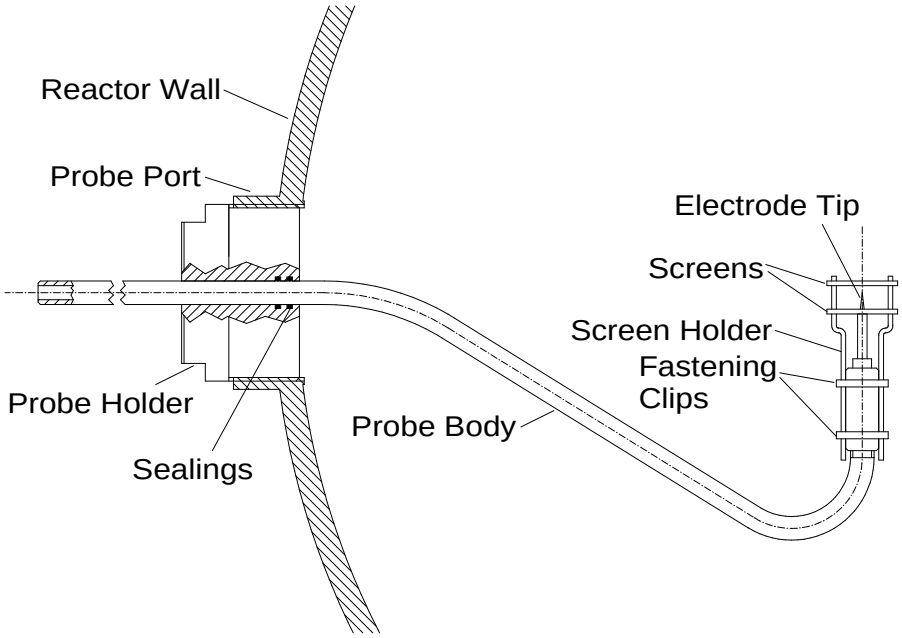

Figure 2.6: Electrodiffusion measurement setup with protective screens at the electrode tip

Since EDM can only measure two-dimensional velocities, the electrode tip has to be shaded from the third component (parallel to the electrode needle axis) in order to avoid errors: The third component contributes to the measured electrical current but cannot be evaluated because calibration can only be carried out for two-dimensional flow. This poses no problem in loop reactors where a main flow direction always can be detected and the probe position be adjusted accordingly. In bubble columns, however, the fluctuational velocities are about the same order of magnitude as the mean velocities or even larger for all three dimensions and no main flow direction can be set. Thus, protective screens have been set up in front of and behind the electrode tip as can be seen from Fig. 2.6. These screens do influence the radial and axial components as well but the flow field disturbance is small compared to the gain in accuracy due to the elimination of third-dimension errors.

The probe body has a sufficient length to allow for measurements being taken from the reactor center to the wall opposite to the probe port thus delivering a radial flow profile of half the reactor. Since previous measurements showed that rotational symmetry of the time-averaged flow inside the bubble column is a legal assumption [31], profiles can be mirrored at the reactor axis to deliver velocities over the whole cross-section. Radial profiles could be measured over the complete reactor height at a vertical spacing of 0.5 m starting 0.35 m above the sparger level. Measurements were taken at 7 radial positions (spacing 0.05 m) starting in the reactor center for a series of 5 superficial gas velocities (0.02, 0.04, 0.06, 0.08 and 0.09 m/s), then moving to the reactor edge,

then switching back to the second position from the center and so on thus minimizing possible drift effects. Measurement of one such series of radial profiles at a giving vertical position took about 150 Minutes (7 radial positions, 5 superficial gas velocities each; approximately 5 minutes per measurement were needed to obtain reliable time averages) and yielded some 70 Megabytes of raw data. After completion of one such series, the measurement which was taken first in the series was repeated to ensure that no overly large drift had occurred in the meantime.

During all EDM measurements, great care has to be taken to keep the liquid phase from slowly degrading yielding a slow drift in measurement results. For measurements to work correctly, the liquid phase must not be pure tap water but has to consist of a 0.01-molar Potassium-Sulfate solution yielding a defined conductivity of the liquid. Other ions may have severely adverse effects on the electrode tips leading to the formation of a black deposit layer on the silver wires and subsequently too low measured electric currents. Therefore, all metal parts of the experimental setup that get into contact with the liquid (fittings, valves, pumps) have to be made completely from sea-water resistant stainless steel (V4A). Additionally, a slow wear of the probe surface may occur due to the abrasive influence of the solids; however, with the measurements taken as part of this project, this was not the case: After a measurement time of approximately 100 hours, a recalibration of the measurement electrode in a flow channel showed no serious deviation from the initial calibration.

2.3.3 Flow Velocity Measurement Results from the Literature

Employing the multitude of measurement principles described above, many researchers have reported on the influence of dispersed phases on the continuous phase flow field. It is, however, very difficult to quantify effects since experimental setups and flow situations under investigation differ very much from project to project. While some workers focused on gas-solid flow, others investigated into liquid-solid or liquid-gas flow; some reports are on vertical flow, some on horizontal; measurements taken in bubble columns can hardly be compared with measurements taken in pipe flow; particle loading, density and size under investigation also differ in a wide range. Only particle influence on the continuous phase will be considered; influence of the continuous phase on particles introducing effects like particle aggregation and floc break-up is described e. g. in [74].

2.3.3.1 Mean Flow Velocity

Most reports on continuous phase velocity in particle-laden flow find that mean velocity decreases markedly with the addition of particles. In his overview, Hetsroni [49] presented measurement results which show that in gas-solid flow, radial velocity profiles flatten out when particles are added; moreover, mean gas-phase velocity decreases by up to 50 % when 3 mm particles are added. The measurements also indicate that further addition of particles again leads to a slight increase

in mean continuous-phase velocity. Guder and Räbiger [42] found that with loop reactors, the addition of particles led to an increase in pressure loss for the liquid circulation and subsequently to a decrease of mean liquid velocity.

Measurements of centerline velocity in two-phase bubble columns have been presented by several research groups. Riquarts [97] has collected measurement results from the literature gained at column diameters of up to 0.6 m and superficial gas velocities of up to 1.43 m/s. His correlation for maximum centerline axial liquid velocity depending on reactor diameter, superficial gas velocity, liquid viscosity and density should therefore very well cover the two-phase measurements taken as part of this project; it is given as:

$$u_{l,ax,max} = 0.21 \cdot \sqrt{D \cdot g} \left(\frac{u_{G,0}^3 \cdot \rho_l}{\mu_l \cdot g} \right)^{1/8} \tag{2.30}$$

The validity of Riquarts's correlation has been confirmed by investigations carried out by Krishna et al. [62] who compared it to their own measurements in bubble columns of up to 0.63 m in diameter and to newer literature data. Thus, eqn. 2.30 is used for the verification of measured and computed two-phase liquid flow velocities of this project as well.

Correlations for the prediction of radial profiles of axial liquid velocity have been presented by several research groups. Wu and Al-Dahhan have derived a complex equation which accounts for the influence of gas holdup on the liquid flow velocity as well as for liquid and gas phase properties [129]. Kawase and Moo-Young [55] have presented a rather simple correlation for radial profiles of axial liquid flow velocity in two-phase bubble columns fit to a wide range of data from the literature:

$$\frac{u_l}{u_{l,ax,max}} = -2 \left(\frac{r}{R} \right)^2 + 1 \tag{2.31}$$

This equation corresponds to a parabolic velocity profile where the maximum downflow velocity at the reactor edge equals the maximum upflow velocity in the reactor center. This is also used to qualitatively verify own measurement and modeling results of this project.

2.3.3.2 Influence of Dispersed Phases on Liquid Turbulence

With the addition of particles to gas and liquid flow situations, measurements of both turbulence increase and turbulence attenuation have been reported in the literature. Main parameters in this context are particle size, density and loading. Hanratty et al. [45] reported on the turbophoretic phenomenon where small drops behaving like particles in a horizontal gas flow tend to move from regions of high turbulence to regions of low turbulence. Hetsroni [49] compared particle relaxation time (based on particle diameter, fluid viscosity and density difference between particle and fluid) to eddy turnover time in order to determine whether particles of a given size are able to follow the continuous phase flow or not. He reports that with the addition of 3 mm particles to gas flow,

turbulence intensity increases with increasing particle loading; reason for this effect may be found in the production of eddies in the wake forming downstream of particles of this size. Triesch and Bohnet [119] found that the addition of 150 μm glass particles to a gas flow leads to turbulence attenuation.

For loop reactors, Guder and Räbiger [42] reported that particle addition initially leads to a turbulence increase but that with a further increase in particle loading, turbulence intensity will decrease again; the maximum value of turbulence intensity and the particle loading at which it occurs they found to depend on particle size, volumetric energy dissipation and particle shape. Wolff [128] focused on the influence of particle diameter and solid concentration on hydrodynamic parameters like integral gas holdup and mass transfer coefficient which are strongly dependent on liquid phase turbulence in bubble columns and loop reactors. From his detailed literature survey he stated that small particles lead to turbulence attenuation mainly due to an increase of apparent suspension viscosity. His own measurement results support the thesis that larger particles increase liquid phase turbulence.

For the measurements performed as part of this project at particle diameters of 3 mm, the evaluation of the abovementioned literature gives rise to the expectation that with increasing particle loading, mean liquid flow velocity should decrease while turbulence intensity should increase.

3 Results of Measurement and Modeling

3.1 Liquid Flow Velocity Measurements

Systematic measurements of local liquid velocities have been performed for a variation of parameters in analogy to the measurements of local dispersed phase holdups presented by Dziallas et al. [31, 32]. Employing the Electrodiffusion Measurement technique, radial as well as centerline velocity profiles have been measured in two- and three-phase flow at different solid loadings with the plate sparger; only Plexiglass (PMMA) has been used as suspended model solid. With the ring sparger and the central nozzle, flow field measurements have been carried out in two-phase flow.

3.1.1 Mean Liquid Velocity in Two-Phase Flow

For an attempt to explain measured time-averaged local dispersed phase distributions, time-averaged local liquid velocities are of primary importance. The mean liquid flow structure gives valuable insight into flow phenomena relevant to both two- and three-phase flow. For the sake of better comparability and to get a first impression of flow fields developing in a pilot-plant size bubble column, flow profiles in two-phase flow are presented first.

3.1.1.1 Radial Profiles of Axial Velocities

The "undisturbed" flow structure that develops in a bubble column far away from sparger and degassing area influences is expected to mainly consist of a parabolic radial profile of axial liquid velocity. This is due to the fact that large bubbles are rising quickly in the center of the reactor dragging liquid with them; continuity considerations then lead to a downflow area close to the reactor wall. Fig. 3.1 shows that 2.35 m above the plate sparger (i. e. in the vertical center of the reactor) this expectation is fulfilled in the pilot-plant size bubble column even for the lowest superficial gas velocity of 0.02 m/s where flow is still in the homogeneous regime and backmixing is mainly due to backflow around the single bubble and not a large-scale liquid circulation.

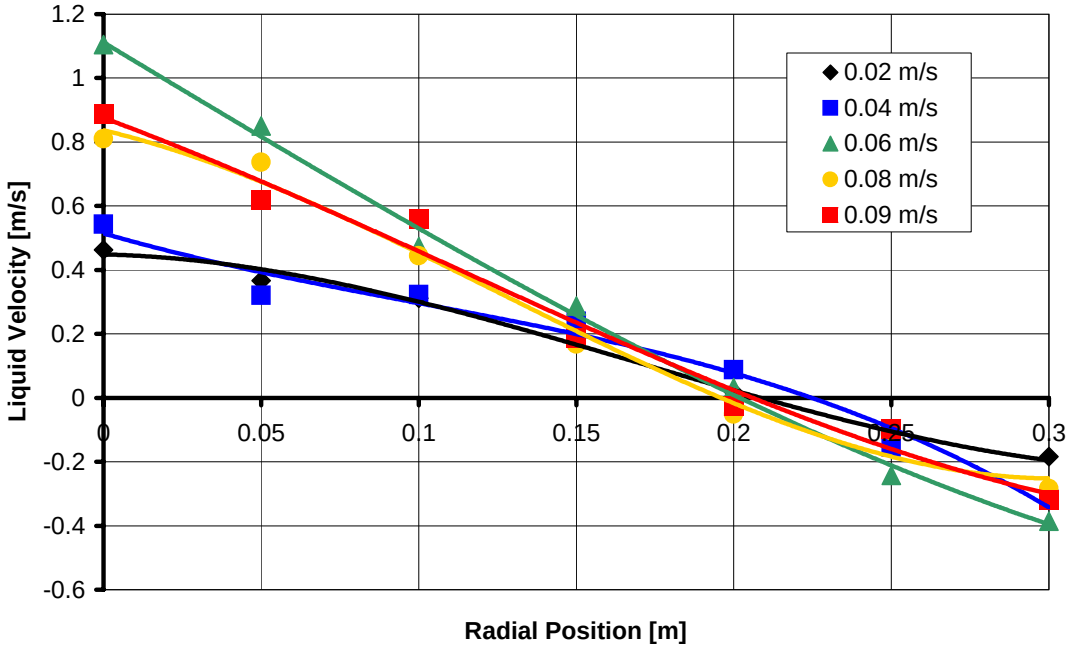

Figure 3.1: Measured axial liquid velocities for different superficial gas velocities, 2.35 m above plate sparger, two-phase flow

It can be seen that in the homogeneous and transition regime at superficial gas velocities of 0.02 and 0.04 m/s, liquid flow profiles are rather flat and an increase in superficial gas velocity in this range does not lead to a substantial increase in liquid velocity. Increasing superficial gas velocity to a value of 0.06 m/s leads to a drastic increase in liquid velocity marking the beginning of the heterogeneous flow regime; at this setting, the highest values are measured (more than 1 m/s in the reactor center). A further increase of superficial gas velocity does not lead to an increase in mean liquid velocity; rather, the additional energy input leads to increased fluctuational velocities and finally to increased turbulent dissipation as will be shown in section 3.1.3.

Comparing measured profiles from Fig. 3.1 to postulated profile shape according to eqn. 2.31 shows that measured downflow velocities close to the reactor edge do not reach the same values as upflow velocities in the reactor center but are significantly lower. This is most likely due to the fact that the gas holdup in the reactor center is much higher than at the reactor edge; thus, higher liquid velocities are necessary in the center to achieve the same volumetric liquid flow rate as at the reactor edge.

Another observation gained from Fig. 3.1 is that profiles in two-phase flow are rather steep especially for higher superficial gas velocities; at gas velocities of 0.06 m/s and higher, profiles are linear rather than parabolic hinting at large bubbles rising in the reactor center at extremely high velocities. In practical operation of bubble column reactors, this effect is unwanted since large bubbles lead to poor mass transfer and short gas residence times in the reactor.

The influence of the sparger's geometry on the local flow field just above the sparger level is shown in Fig. 3.2 for plate sparger and central nozzle.

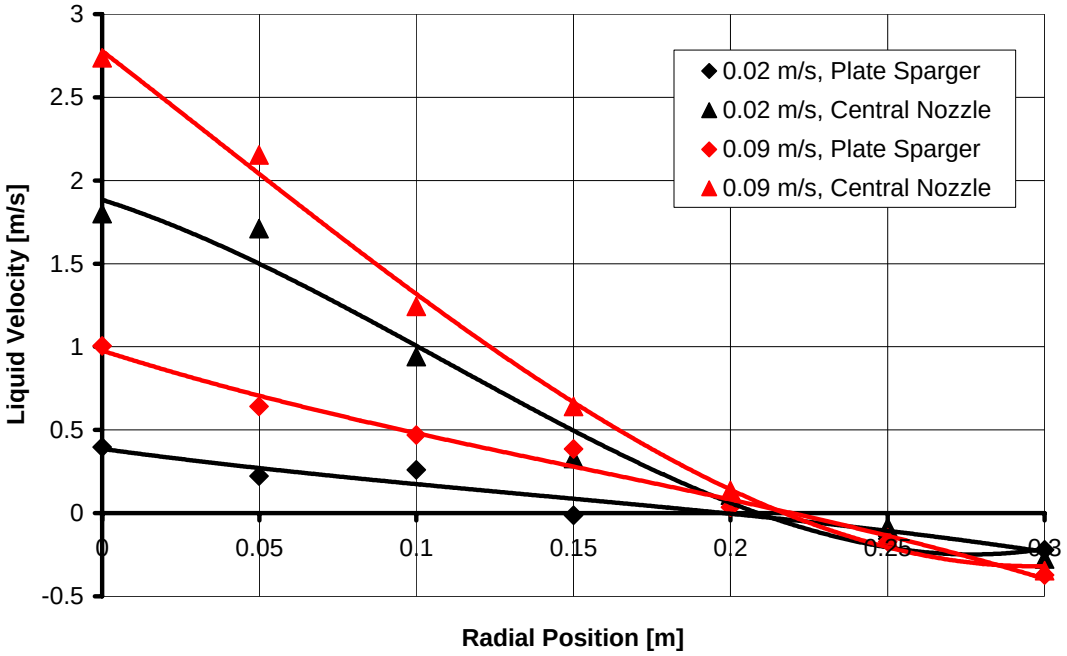

Figure 3.2: Sparger influence on radial profiles of measured axial liquid velocities 0.85 m above sparger for 2 different superficial gas velocities, two-phase flow

As can be seen, 0.85 m above the sparger the central nozzle leads to extremely high upflow velocities in the center of the reactor even at the lowest superficial gas velocity of 0.02 m/s. The measured maximum value of more than 2.5 m/s in the center of the reactor at a superficial gas velocity of 0.09 m/s is far beyond the actual calibration range of the EDM probe (which in this case was only calibrated for measurements of up to 1.2 m/s). Still, the fairly linear relationship of electric current and actual liquid velocity admits for a certain amount of extrapolation even at the extremely high gas holdups found above the nozzle, thus the values plotted in Fig. 3.2 should give a realistic impression of the order of magnitude of liquid velocities encountered in the environment of a central nozzle sparger.

With the ring sparger, most interesting effects on the flow field can be found a little further above at a distance of 1.35 m from the sparger level. Fig. 3.3 shows radial profiles of axial liquid velocities for increasing superficial gas velocities.

For reason of better solid fluidization in three-phase flow, the ring sparger ejects air at its bottom side directed to the reactor wall. This induces gas and subsequently liquid upflow at the reactor wall and downflow in the center of the reactor for the bottom part of the bubble column. Further up, these flow profiles shift to the usual parabolic shape with upflow in the center and downflow close to the wall as encountered with the plate sparger (see Fig. 3.1). Fig. 3.3 shows that the extension of the flow field transition zone strongly depends on superficial gas velocity: At a vertical position 1.35 m above the ring sparger, central downflow occurs only at superficial gas velocities of 0.02 and 0.04 m/s. With increasing superficial gas velocity, the maximum upflow velocity shifts to the reactor center; at a superficial gas velocity of 0.09 m/s, the liquid flow profile

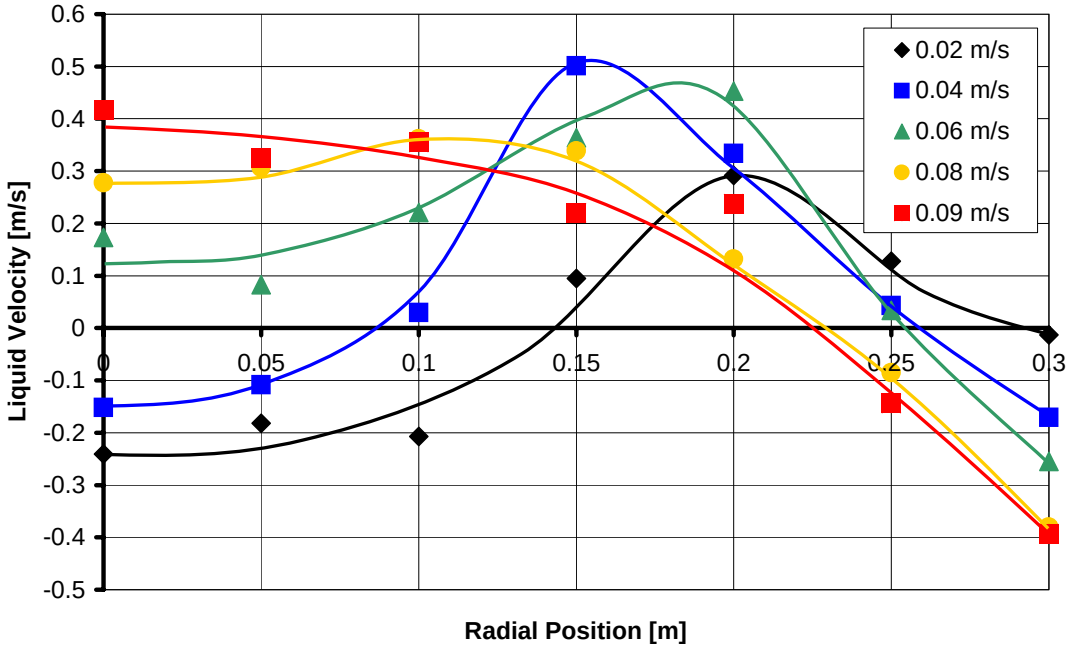

Figure 3.3: Radial profiles of measured axial liquid velocities 1.35 m above sparger for different superficial gas velocities; ring sparger, two-phase flow

takes on the common parabolic shape. This means that at higher superficial gas velocities, the transition zone at the reactor bottom becomes considerably smaller.

3.1.1.2 Centerline Axial Velocities

A good impression of the liquid circulation over the whole reactor height can be gained from an evaluation of the axial liquid velocities on the reactor centerline. Fig. 3.4 shows centerline profiles of axial liquid velocities for superficial gas velocities of 0.02 and 0.09 m/s with the plate sparger as well as with the central nozzle.

With the plate sparger, influence of the sparger and degassing zone is limited to areas approximately 1 m above the sparger and below the upper dispersion level. In these areas, axial liquid velocity decreases to almost zero while radial velocity increases due to liquid being transported to or from the downflow area close to the reactor wall. With the remainder of the reactor, liquid centerline velocity is fairly constant and depends only on superficial gas velocity.

As could already be seen from Fig. 3.2, in comparison to the plate sparger the central nozzle induces a distinct velocity peak in the bottom section of the column. No velocity measurements could be taken 0.35 m above the nozzle as the fragile probe was in danger of being destroyed by the high velocities in this area; additionally, the high gas holdup just above the nozzle renders evaluation and bubble signal filtering of the raw measurement data impossible.

At the lowest superficial gas velocity of 0.02 m/s, the influence of the central nozzle is most eminent in comparison to the plate sparger flow field. Over the whole reactor height, the nozzle

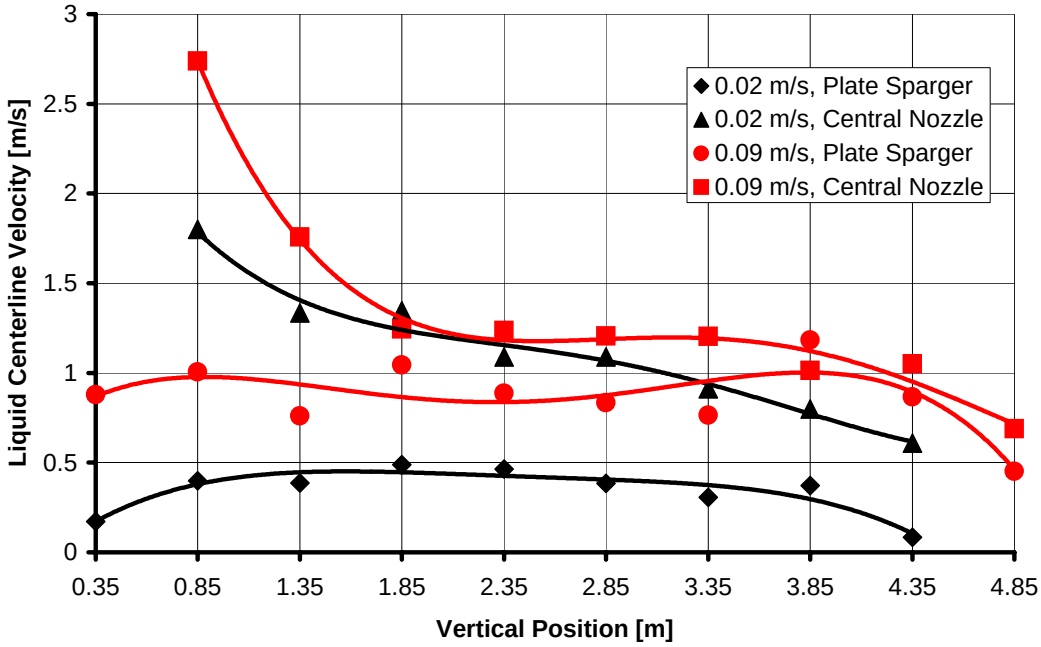

Figure 3.4: Sparger influence on centerline profiles of measured axial liquid velocities for 2 different superficial gas velocities, two-phase flow

yields a more than twofold increase in centerline velocity compared to the plate sparger. Reason for this can be found in the generation of large bubbles at the nozzle even at this low superficial gas velocity which quickly rise through the reactor. At high superficial gas velocities, large bubbles are forming in the reactor center with the plate sparger as well; thus, at a superficial gas velocity of 0.09 m/s, the increase of centerline velocity with the central nozzle compared to the plate sparger values is not as distinct as at 0.02 m/s.

Centerline profiles of axial liquid velocity with the ring sparger in two-phase flow are shown in Fig. 3.5 for superficial gas velocities ranging from 0.02 m/s to 0.09 m/s.

The effect of increasing superficial gas velocity on the extension of the transition zone at the reactor bottom that has already been deduced from Fig. 3.3 can be seen very clearly from Fig. 3.5. While at a superficial gas velocity of 0.02 m/s, the switching from downflow to upflow in the reactor center occurs at a position approximately 1.85 m above the sparger, at higher gas velocities this switching point moves down reaching 0.85 m above the sparger at a gas velocity of 0.09 m/s. The influence of the ring sparger on liquid flow reaches even higher – the maximum of the centerline velocity profiles is not reached before a position 2.85 m above the sparger, while the plate sparger's influence only extended for about 1 m above the sparger level and even the central nozzle's peak has disappeared 2.35 m above the sparger (compare Fig. 3.4).

In general, the values of centerline velocities in the upper half of the reactor with the ring sparger are significantly higher in the heterogeneous flow regime than the corresponding values with the plate sparger and even somewhat higher than with the central nozzle. In comparison to the plate sparger, this effect can be explained with the larger fraction of large bubbles being

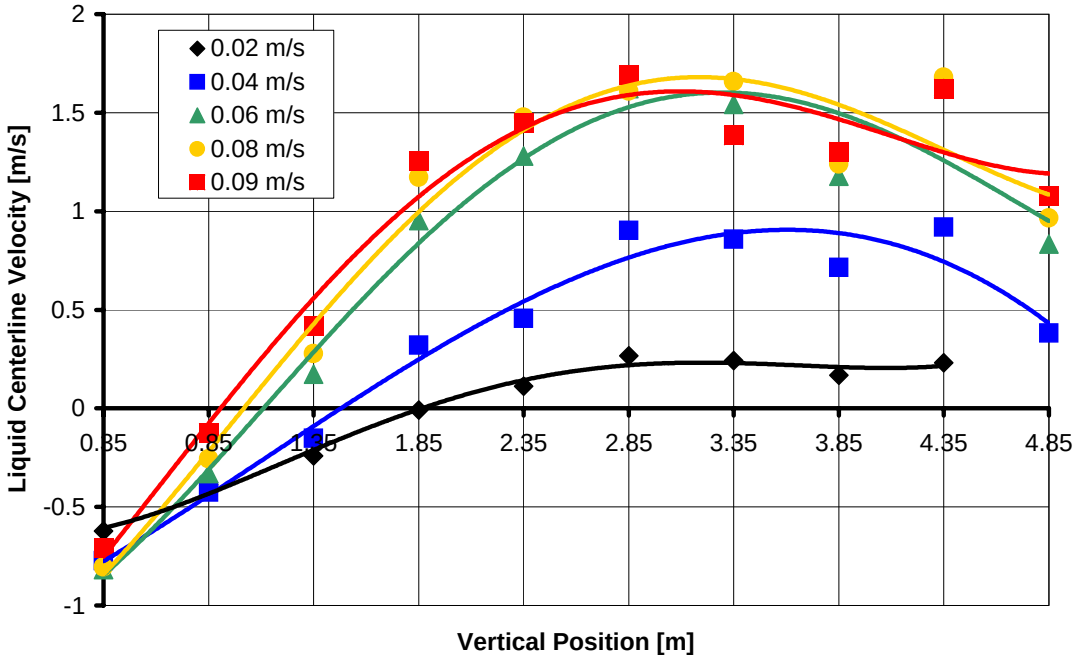

Figure 3.5: Measured axial liquid velocities on the reactor centerline for different superficial gas velocities; ring sparger, two-phase flow

ejected from the ring sparger. With the central nozzle, possible reason for the comparably low centerline upflow velocities in the upper half of the reactor can be found in the high turbulent dissipation above the sparger; for more detailed investigations on this issue, see section 3.1.3.

3.1.2 Mean Liquid Velocity in Three-Phase Flow

Adding solids to two-phase flow poses a large number of additional tasks and questions regarding flow fields and fluidization. On one hand, the influence of solids on liquid velocity and mixing inside the reactor is of interest; on the other hand, liquid velocity's influence on solid fluidization is of importance in determining optimum operating conditions for reactors with respect to gas and solid distribution.

3.1.2.1 Radial Profiles of Axial Velocities

The general influence of adding 10 Vol.-% of PMMA solids to the contents of the bubble column reactor can be seen for a vertical position 2.35 m above the plate sparger (i. e. for the same position as in Fig. 3.1) in the radial profiles of axial liquid velocity shown in Fig. 3.6.

Velocity profile shape and range of velocity values in Fig. 3.6 show significant differences compared to the two-phase flow case from Fig. 3.1. The velocities especially in the reactor center are about 40 % lower than in two-phase flow probably owing to the large attenuating influence of the solid particles resulting in an increase of liquid-solid mixture viscosity. A more detailed assessment of the influence of gradually adding solids to the reactor contents will be given for centerline liquid

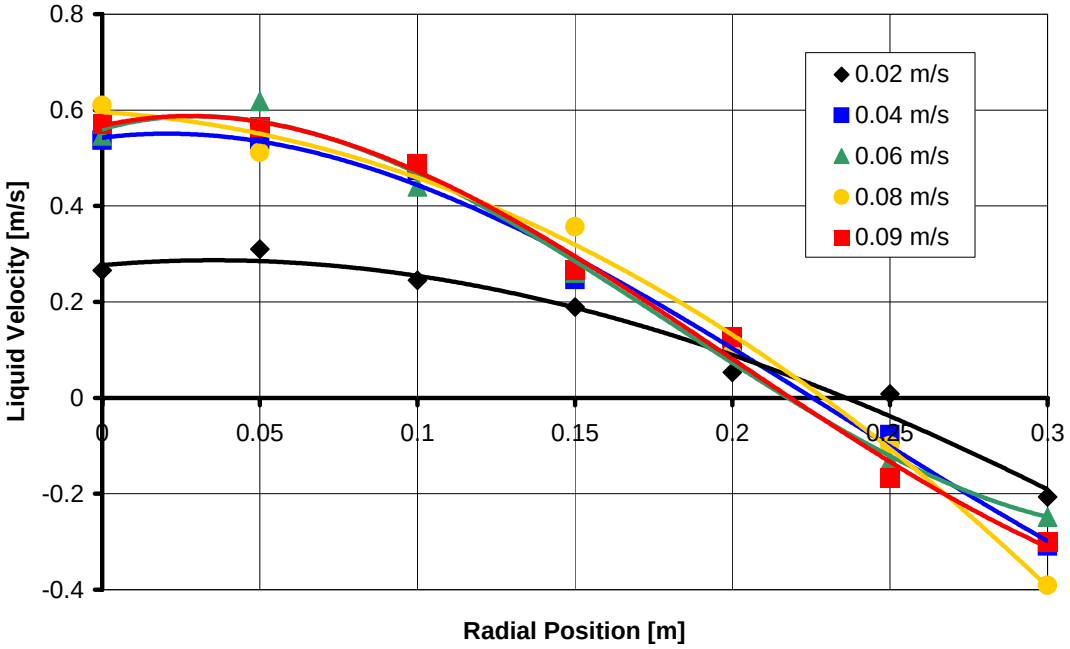

Figure 3.6: Measured axial liquid velocities for different superficial gas velocities, 2.35 m above plate sparger, 10 Vol.-% PMMA

velocity profiles in section 3.1.2.2.

The radial velocity profiles measured in three-phase flow are in general significantly flatter than in the two-phase flow case. While in Fig. 3.1 profiles are almost linear, those in Fig. 3.6 take on a distinct parabolic shape. This basically means that velocities in the reactor center are decreasing overproportionally upon adding solids compared to the remainder of the reactor. Reason for this may probably be found in the reduced formation of fast-rising large bubbles due to the presence of solids.

Among the most interesting aspects in the work of Dziallas et al. [31, 32] is the adverse effect of increasing superficial gas velocity on solid fluidization in the bubble column. When due to rather small density differences between solid and liquid a system is already homogeneously fluidized at low superficial gas velocities, an increase of gas velocity will yield demixing instead of more homogeneous solid distribution. Especially at the upper reactor edge a large area develops where hardly any solid can be encountered. Among the possible reasons for this effect, gas-liquid mixture density is definitely of important influence on fluidization; this will be investigated in more detail in section 3.2.5. The following will look closely at the liquid flow structure in the upper reactor region and explain the influence of superficial gas velocity on liquid flow and the resulting demixing effect in the reactor wall area.

Fig. 3.7 shows radial profiles of axial liquid velocities at superficial gas velocities of 0.02 m/s and 0.09 m/s for the three upper levels of the reactor (10 % PMMA, plate sparger). The topmost level (4.85 m above the sparger) has not been included in these considerations because no data are available for the superficial gas velocity of 0.02 m/s due to an insufficiently high liquid level.

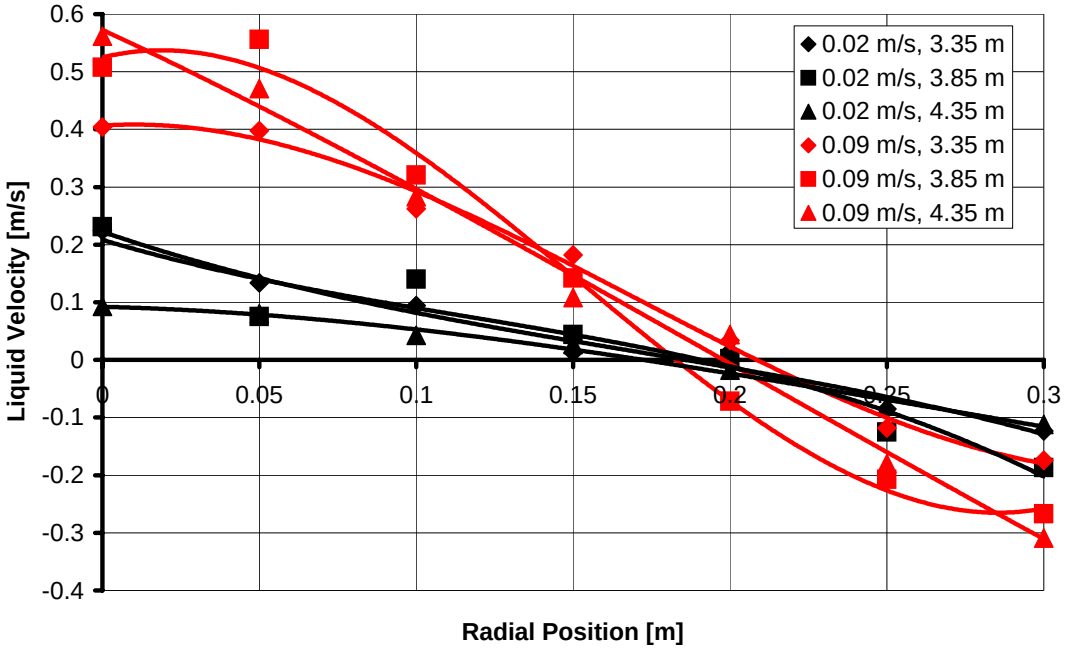

Figure 3.7: Measured flow structure in the upper reactor area: Radial profiles of axial liquid velocities for the 3 upper levels and 2 different superficial gas velocities; plate sparger, 10 Vol.-% PMMA

At the low superficial gas velocity of 0.02 m/s, radial profiles of axial liquid velocity are almost linear. With increasing vertical position, a decrease in upflow velocity in the reactor center can be found only for the highest position (4.35 m). Downflow velocities near the wall do not differ much and are rather moderate; thus, no significant solid transport to the bottom of the reactor takes place here. At the high superficial gas velocity of 0.09 m/s, upflow velocity in the reactor center as well as downflow velocity close to the wall increase with increasing vertical position. Since gas holdup in the reactor center is much higher than close to the wall corresponding to a much lower gas-liquid mixture density in the center (see section 3.2.5), not as much solid is transported upward in the center as can be transported downward close to the wall. From this effect results the development of the low-solid holdup area near the upper reactor wall as observed by Dziallas et al. [31, 32].

3.1.2.2 Centerline Axial Velocities

As with two-phase flow, also in three-phase flow the liquid circulation over the whole reactor can best be assessed by looking at centerline axial velocities. Fig. 3.8 shows the influence of solids on the measured liquid centerline velocity inside the bubble column for 2 different superficial gas velocities.

At the low superficial gas velocity of 0.02 m/s as well as at the highest value of 0.09 m/s, highest liquid centerline velocities are found in two-phase flow. At 0.02 m/s, adding 5 Vol.-% of PMMA granules yield a distinctive decrease in liquid velocity to almost one half the corresponding

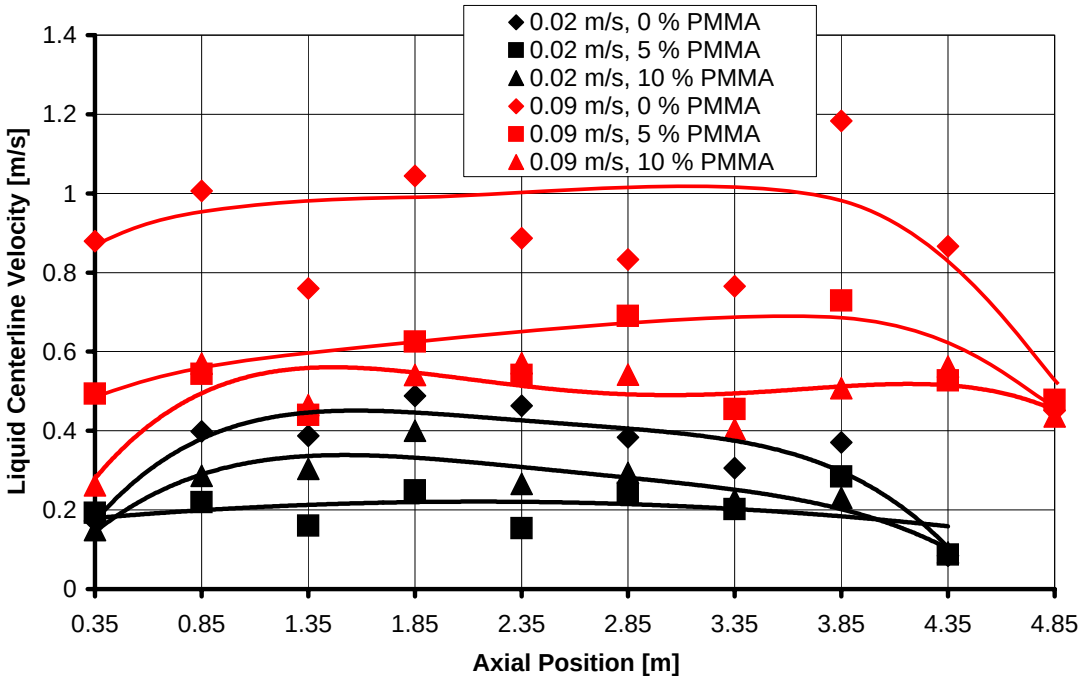

Figure 3.8: Measured axial liquid velocities on the reactor centerline for different solid loadings and 2 different superficial gas velocities, plate sparger

two-phase flow values. The velocity profile becomes almost flat hinting at a reduced influence of sparger and degassing area on the flow field in three-phase flow. Increasing solid loading to 10 Vol.-% of PMMA leads to a marked increase in measured centerline liquid velocity values reaching about three quarters of the two-phase flow values. Also, the influence of sparger and degassing area becomes more distinctive again.

At the high superficial gas velocity of 0.09 m/s, large scatter in data makes interpretation somewhat tedious but in general, the same trends can be found as with the low gas velocity. Adding 5 Vol.-% of PMMA leads to almost half as high liquid velocities and rather flat vertical velocity profiles. The increase in liquid velocities obtained when increasing solid loading to 10 Vol.-% is not confirmed for all vertical positions at the high gas velocity; on average, liquid velocity decreases slightly when additional solid is added to the reactor contents.

3.1.3 Fluctuational Liquid Velocity in Two-Phase Flow

In addition to liquid mean velocities, evaluation of EDM measurements also yields information on local fluctuational velocities in axial as well as in radial direction. Regrettably, the evaluation algorithm did not give any information on frequency spectra of the turbulent motion, thus no detailed investigation of turbulence quantities is possible. Still, an evaluation of the mere fluctuational velocity yields interesting insights into liquid flow structure and allows for at least a qualitative assessment of turbulence phenomena inside the bubble column.

Fig. 3.9 shows radial profiles of measured axial and radial liquid fluctuational velocities in two-

phase flow at superficial gas velocities of 0.02 and 0.09 m/s at a vertical position 2.35 m above the plate sparger (i. e. in the vertical center of the reactor where influence of sparger and degassing area are minimal; the corresponding mean axial liquid velocities are shown in Fig. 3.1).

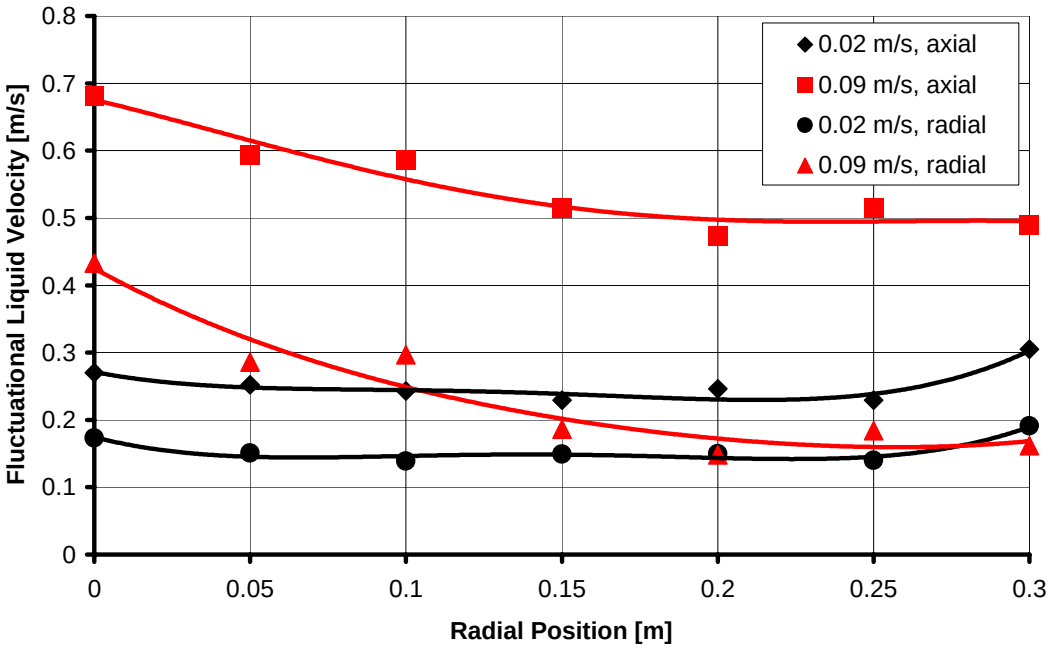

Figure 3.9: Radial profiles of measured axial and radial liquid fluctuational velocities at 2 different superficial gas velocities 2.35 m above the plate sparger; two-phase flow (for corresponding mean axial liquid velocities see Fig. 3.1)

For the low superficial gas velocity of 0.02 m/s, it can be seen that axial and radial fluctuational velocity reach their maximum in the areas of highest mean velocities, i. e. in the reactor center and in the downflow area close to the wall. The values of the fluctuational velocities are in the same order of magnitude as those of the mean velocities confirming the highly chaotic and turbulent fluid motion inside the bubble column even at this low superficial gas velocity. Still, at this low gas velocity, profiles of fluctuational velocities are rather flat showing that the bubble column is operated in the homogeneous flow regime. Radial fluctuational velocities are about 40 % lower than axial ones; this lets questions arise as to whether an isotropic turbulence model like the k-ε model is actually correct for flow predictions in this kind of bubble column.

At the high superficial gas velocity of 0.09 m/s, the discrepancy between axial and radial fluctuational velocity becomes even larger; close to the wall, the radial fluctuational velocity is about 60 % smaller than the axial one. The maxima of both fluctuational velocities at this high gas velocity can be found in the reactor center where large bubbles are rising; this means that again, largest fluctuational velocities are found in the area of largest mean velocities.

The local distribution of axial fluctuational liquid velocity over the whole flow domain can be seen from Fig. 3.10 for ring sparger and central nozzle in two-phase flow at increasing superficial gas velocities. The isolines were obtained by spline-interpolating the original data which were

available on a grid of 7 radial times 10 vertical measurement positions.

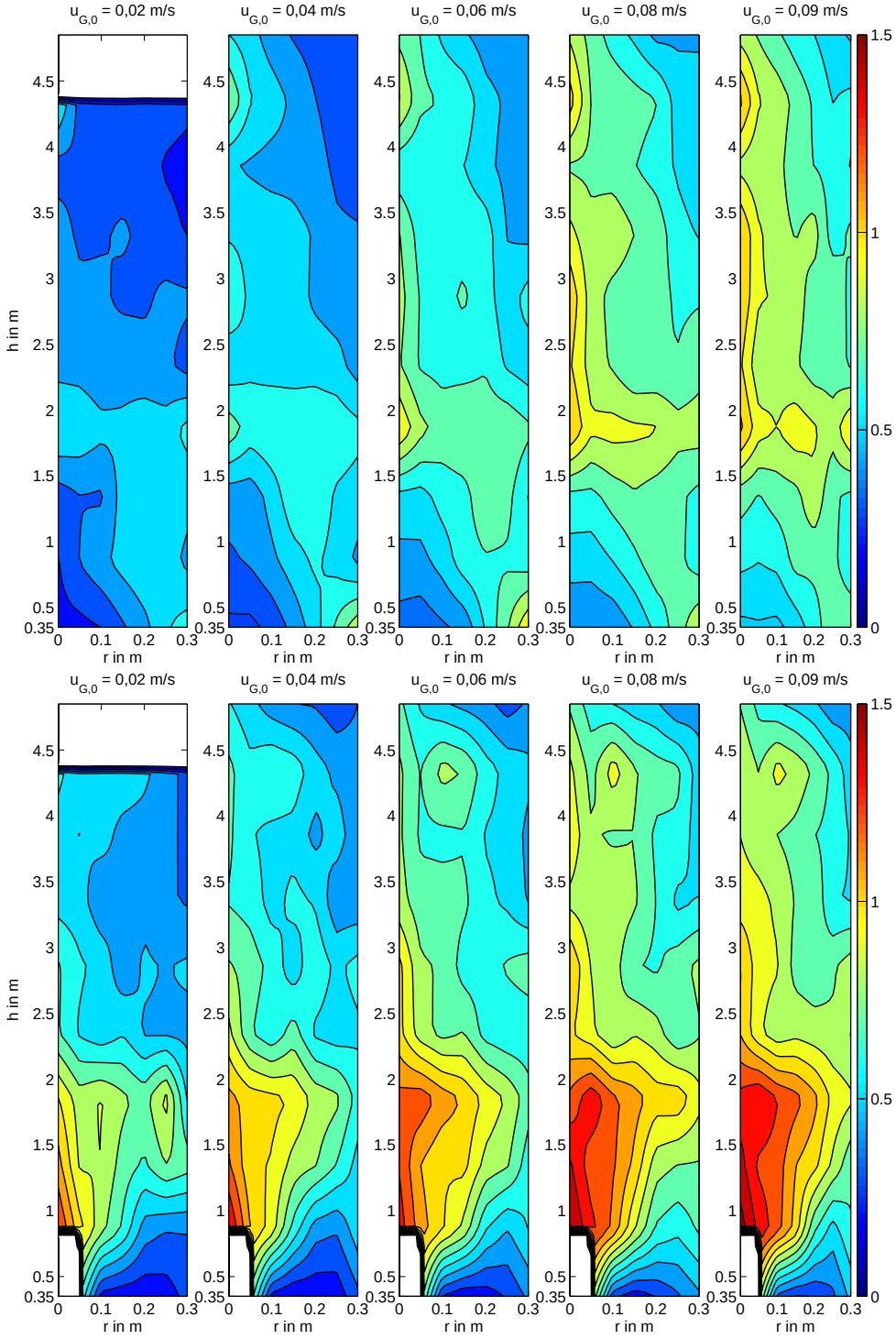

Figure 3.10: Measured axial fluctuational velocity in m/s in two-phase flow for ring sparger (top) and central nozzle (bottom)

It has been shown previously (e. g. for the ring sparger in Fig. 3.5) that the additional energy input upon increasing superficial gas velocity from 0.04 m/s to 0.06, 0.08 and 0.09 m/s does not lead to a further increase in mean liquid velocities. Fig. 3.10 now clearly shows that the additional

energy input only increases the fluctuational velocities finally leading to increased turbulent dissipation. A comparison of fluctuational velocities with the ring sparger and the central nozzle shows that the sparger influence is limited to the bottom half of the reactor. In this region, very high fluctuational velocities are measured with the central nozzle while the ring sparger only induces a zone with slightly increased fluctuational velocities in the region 1.3 to 2.3 m above the sparger (depending on superficial gas velocity) where the upflow region shifts from the reactor wall to the center.

In the upper half of the reactor, fluctuational velocity distributions look very similar for ring sparger and central nozzle (as well as for the plate sparger, here not shown). This is in good agreement with measurements by Dziallas et al. [31, 32] who have found qualitatively similar local distributions of gas and solid phase in the upper half of the reactor for all three sparger configurations under consideration here thus also coming to the conclusion that sparger influence is limited to the bottom part of the reactor.

3.1.4 Fluctuational Liquid Velocity and Turbulence Intensity in Three-Phase Flow

The measured influence of solid loading on local fluctuational velocities in the bubble column follows the same general trends as with the mean velocities described in section 3.1.2. Fig. 3.11 shows the influence of solid loading on radial profiles of axial liquid fluctuational velocities at superficial gas velocities of 0.02 and 0.09 m/s measured 2.35 m above the plate sparger.

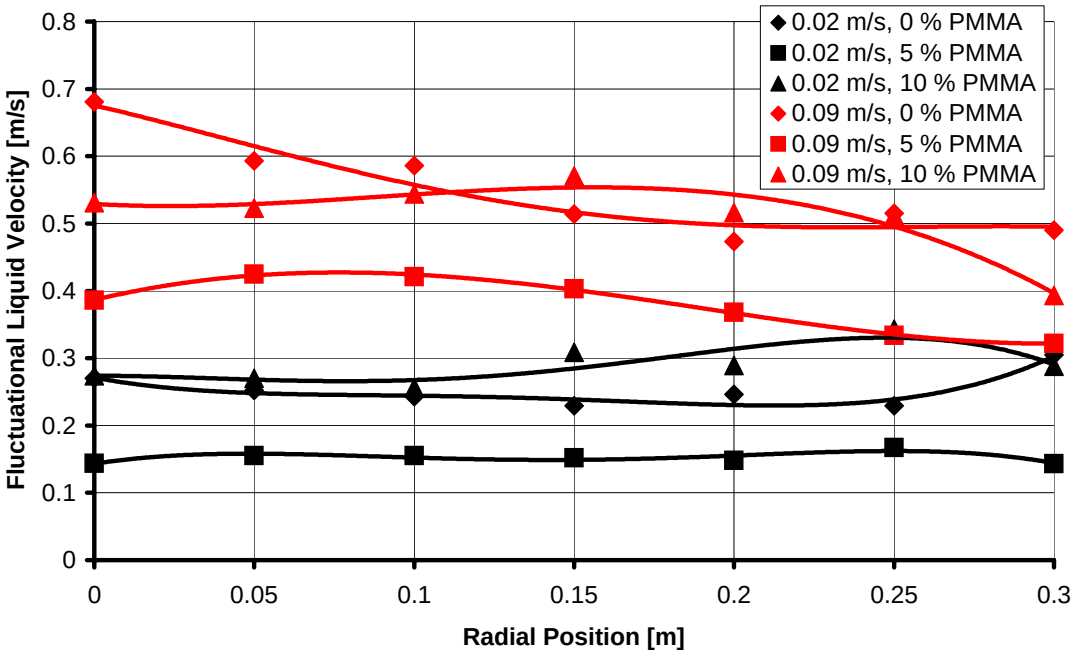

Figure 3.11: Radial profiles of measured axial liquid fluctuational velocities for 2 different superficial gas velocities and different PMMA solid loadings 2.35 m above the plate sparger

At the lowest superficial gas velocity of 0.02 m/s, the addition of 5 Vol.-% PMMA to the reactor contents leads to a marked decrease in fluctuational velocities. The fluctuational velocity profile becomes very flat even not showing the small maxima in the center and close to the wall that were encountered in two-phase flow but moreover decreasing slightly at these locations. This effect clearly shows the attenuating influence that adding solids of this density and size (1200 kg/m^3, 3 mm particle diameter) can have on the flow in bubble columns. However, a further addition of solids up to an integral loading of 10 Vol.-% does not lead to a further decrease in fluctuational velocities but actually yields a distinct increase of velocities up to values which are even higher than in the two-phase case. From the literature review in section 2.3.3.2, this should be expected for this size of particles. Reason for the initial attenuating effect is hard to be found but may probably be caused by the increased suspension viscosity of the solid-liquid mixture. Superimposed on this influence may be the turbulence intensification due to vortex generation in the wake of the particles – an effect that possibly gains influence at higher solid loadings.

At the highest superficial gas velocity of 0.09 m/s, the same effects can be observed. Adding 5 Vol.-% of solid leads to a marked decrease in fluctuational velocity which is compensated almost completely when solid loading is increased further to 10 Vol.-%. Only in the reactor center, fluctuational velocities are always highest in two-phase flow.

In this context of greater interest than the mere fluctuational velocities is probably the ratio of fluctuational to mean velocity (i. e. the relative turbulence intensity). The influence of solid addition on radial profiles of axial relative turbulence intensity for the same settings as for the fluctuational velocities in Fig. 3.11 is given in Fig. 3.12.

It can be observed that for most radial positions, mean and fluctuational velocity are of the same order of magnitude yielding relative turbulence intensities ranging between 1 and 3. Only at locations where the mean velocity is very low (i. e. at a radius of approximately 0.2 m where the parabolic mean velocity profile switches from upflow to downflow), relative turbulence intensity reaches peak values of up to 18 and higher. Most noticeable is the fact that while at this peak position the highest relative turbulence intensities can be found in two-phase flow, the influence of solid loading on relative turbulence intensity at all other positions is negligible: No trends can be made out in the general data scatter.

As a first conclusion from these observations it may be stated that while solid loading has a definite influence on measured mean velocities (even if no clear trend in one direction can be deduced), relative turbulence intensity is not influenced in a significant manner. Furthermore, peak values of relative turbulence intensity are not found in regions of high mean liquid velocity but rather in those areas where the mean velocity goes to zero. Thus, considering relative turbulence intensity as a measure of local stress seems to be inappropriate since highest stress values will definitely be found in areas of high fluctuational velocities which are more likely to be found in areas of high mean velocities (see Fig. 3.11).

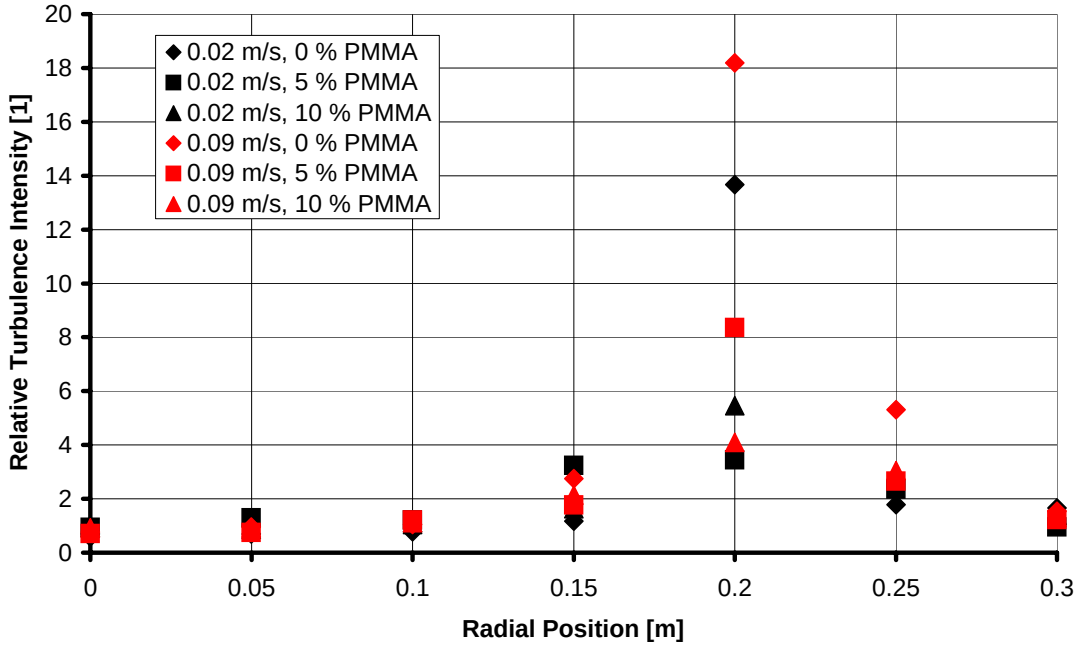

Figure 3.12: Radial profiles of measured axial liquid relative turbulence intensities (ratio of fluctuational to mean velocities) for 2 different superficial gas velocities and different PMMA solid loadings 2.35 m above the plate sparger

3.2 CFD Results and Model Validation

3.2.1 Comparison of Direct Dispersed Phase Interaction Models

As modeling experience showed, most influential effects on computed phase holdup distribution and liquid flow fields were given by the choice of direct dispersed phase interaction. Without the inclusion of such effects, in three-phase calculations no reasonable solid fluidization could be achieved – the solid would settle forming a sediment layer at the reactor bottom. In order to find a numerically efficient and physically sensible model for the momentum exchange between gas and solid phase, test calculations have been performed with the three interaction models presented in section 2.2.3.2 for the case of a bubble column equipped with a plate sparger and operated at an integral solid loading of 10 Vol.-% of PMMA (density 1200 kg/m^3, diameter 3 mm). As result of these calculations, modeling parameters giving best accordance of computational results and measurements as presented by Dziallas et al. [31, 32] could be determined.

Fluidization results obtained implementing the model with constant source terms as presented on page 14 are shown for several superficial gas velocities in Fig. 3.13. From left to right, each of the five parts gives a two-dimensional vertical cross-section image of local solid holdup in the reactor flow domain (diameter 0.63 m, height 5.0 m) for increasing superficial gas velocities.

Fig. 3.13 shows that the interaction model with constant source terms is capable of capturing the experimentally proven [31, 32] adverse effect of increasing superficial gas velocity on solid

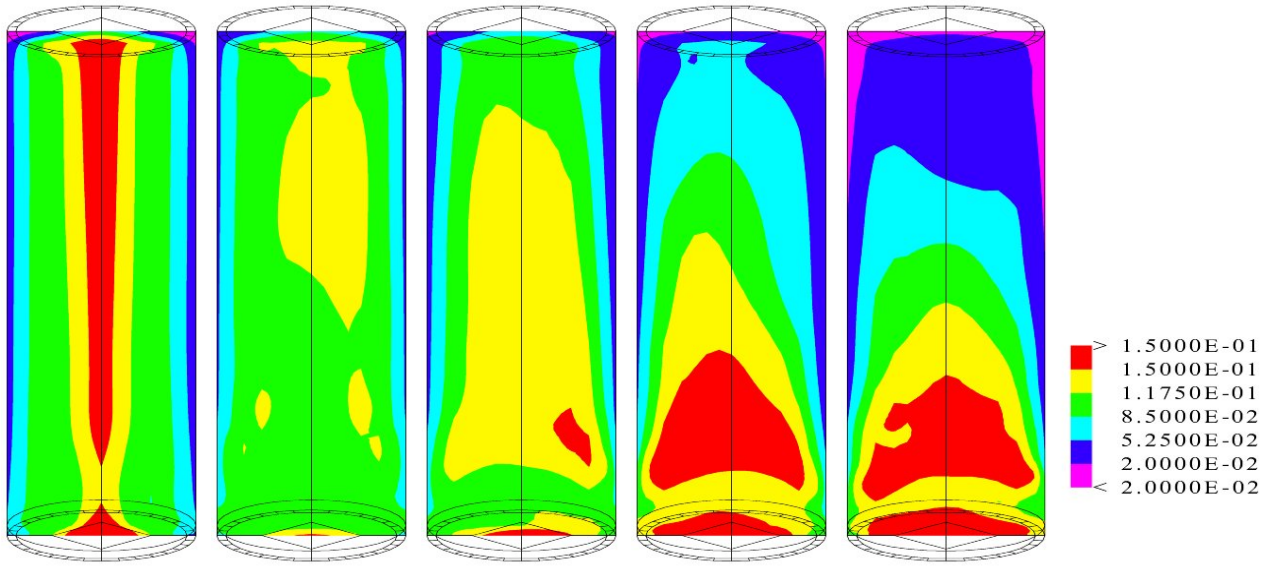

Figure 3.13: Computed solid holdup (volume fraction) with the plate sparger at an integral solid loading of 10 Vol.-% PMMA; reactor diameter 0.63 m, reactor height 5.0 m; increasing superficial gas velocities from left to right (0.02, 0.04, 0.06, 0.08, 0.09 m/s, respectively); direct dispersed phase interaction modeling with constant source terms; averaging time 140 s

fluidization when homogeneous fluidization has already been achieved. Obviously, even at the lowest superficial gas velocity of 0.02 m/s, the rather lightweight solid (PMMA) is almost homogeneously distributed in the reactor; an increase of superficial gas velocity does not lead to an increased homogeneity but only yields the formation of a large region with low solid content at the upper reactor edge (an attempt at clarifying the physical background of this effect which is of vital importance for the industrial operation of this kind of reactors can be found in section 3.2.5). Marked deviation from the measured solid holdup distributions of [31, 32] can only be found for a superficial gas velocity of 0.02 m/s where the computations predict a radial solid holdup profile with a distinctive maximum in the reactor center which is not found in the measurements. Still, if the simplicity of the modeling approach is taken into account, model performance is remarkable. The computed time in this calculation was 160 s where time-averaged values were computed over the last 140 s; this corresponds to a computation time of 24 hours on an 800 MHz PC workstation.

Calculations with the more refined interaction model with holdup-dependent source terms as introduced on page 15 did not yield results as satisfactory as with the simpler model. Considering solid fluidization, no realistic profiles could be obtained – during fitting of the parameter c_g in eqn. 2.17, no range of values could be found where solids did not form a sediment layer at the reactor bottom and at the same time gather in a flotation layer at the reactor top. Therefore, this model has not been used for further calculations.

Results from model calculations implementing the interaction model with slip-velocity depen-

dent source terms as presented in eqns. 2.20 and 2.21 are shown in Fig. 3.14.

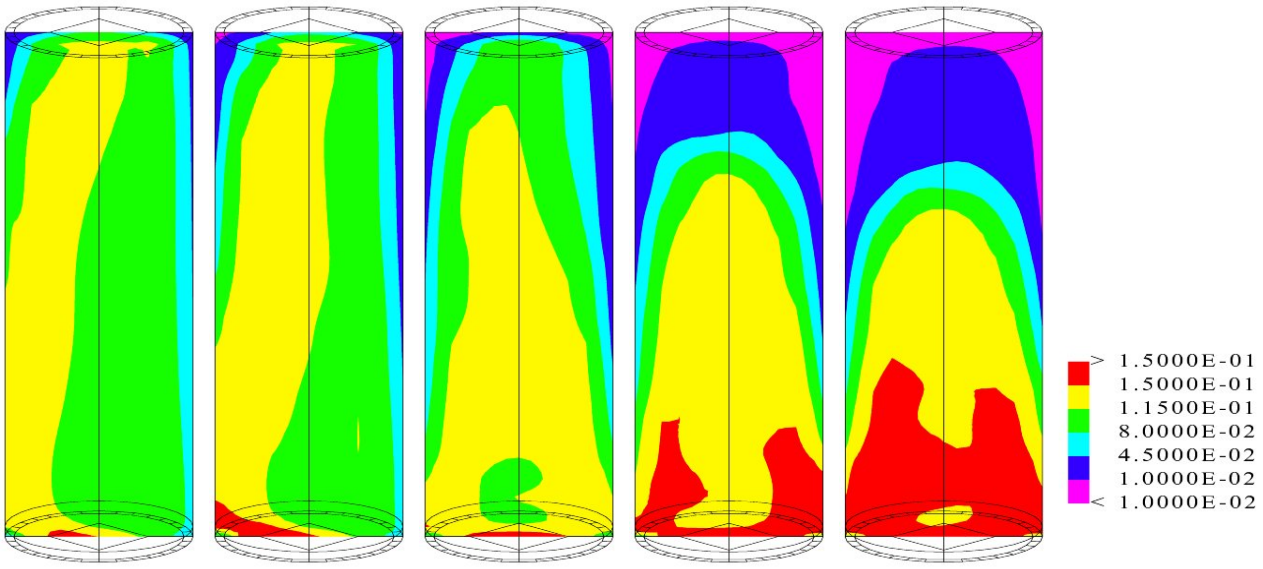

Figure 3.14: Computed solid holdup (volume fraction) with the plate sparger at an integral solid loading of 10 Vol.-% PMMA; increasing superficial gas velocities from left to right (0.02, 0.04, 0.06, 0.08, 0.09 m/s, respectively); direct dispersed phase interaction modeling with slip-velocity dependent source terms; averaging time 300 s

It can be seen that with the value of $c_{g,s} \cdot u_{slip,g,s}$ set to 118 m/s by fitting computational results to the same set of experimental data [31, 32] as used for the model with constant source terms, good accordance between measurement and modeling results can be achieved. The model with slip-velocity dependent source terms is even better in capturing the adverse effect of increasing superficial gas velocity on solid fluidization; especially the homogeneous fluidization at a superficial gas velocity of 0.02 m/s is computed without the distinct solid maximum in the reactor center that has been obtained with the simpler model.

It has to be noted, however, that the improvement in modeling consistency comes at the expense of additional computational demand: After a computed time of 160 s (140 s of time-averaging), no reasonable steady-state holdup-profiles could be obtained – results still showed serious unsymmetry. Therefore, averaging time had to be increased to a period of 300 s (total computed time 320 s) which means that a typical run with this model consumes 48 hours of processor time (800 MHz PC workstation) instead of 24 hours as with the model with constant source terms.

Due to the improved accordance of measurement and computational results and in spite of the additional computational demand, the direct dispersed phase interaction model with slip-velocity dependent source terms in the momentum balances has been used for all subsequent calculations presented in this report. Fig. 3.15 shows local gas holdups as computed with the slip-velocity

dependent model for different superficial gas velocities.

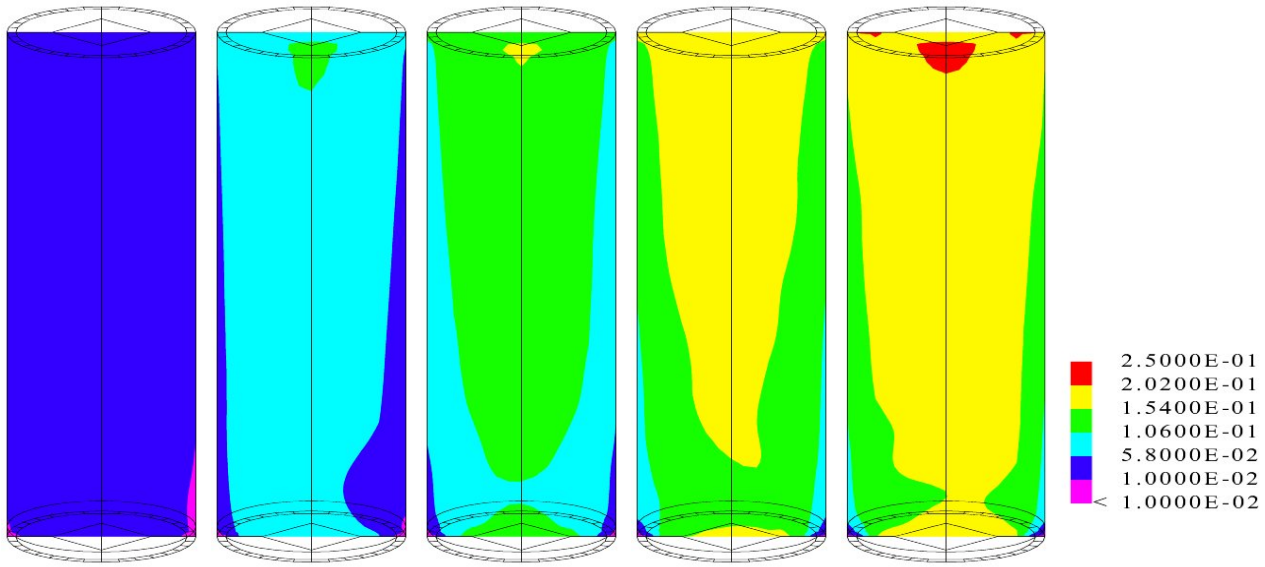

Figure 3.15: Computed gas holdup (volume fraction) with the plate sparger at an integral solid loading of 10 Vol.-% PMMA; increasing superficial gas velocities from left to right (0.02, 0.04, 0.06, 0.08, 0.09 m/s, respectively); direct dispersed phase interaction modeling with slip-velocity dependent source terms; averaging time 300 s

From Fig. 3.15 it clearly can be seen that the local gas distribution inside the bubble column can be regarded as a superposition of a radial parabolic holdup profile and the axial gas expansion with increasing vertical position in the reactor. Compared to measured values, the radial profile is overpredicted by the model at lower superficial gas velocities; especially at 0.02 m/s (leftmost image in Fig. 3.15), a higher colour resolution would reveal a distinct parabolic radial profile where measurements showed that no radial profile develops and only axial gas expansion occurs. Still, the overall tendency of increasing gas holdup with increasing superficial gas velocity and the general gas distribution are very well captured by the model.

3.2.2 Integral Gas Holdup

For a better quantitative assessment which more clearly shows possibilities and limitations of the model, integral gas holdup has been computed for all the calculations presented as well and can easily be compared to measurement results [31, 32]. Fig. 3.16 shows a comparison of computed and measured integral gas holdups for the same settings as in Fig. 3.15 (plate sparger, solid loading 10 Vol.-% PMMA).

General agreement between measurement and modeling results with respect to integral gas holdup is quite good. While the model is very well capable of capturing the right order of magnitude of gas holdup and general dependency of gas holdup on superficial gas velocity, it can not

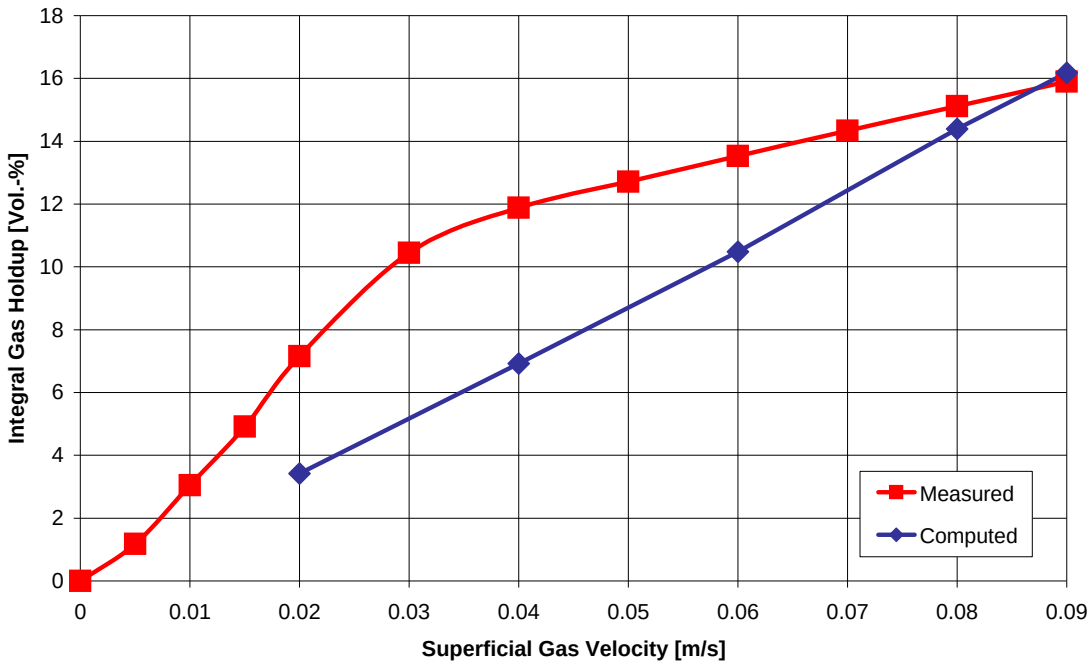

Figure 3.16: Comparison of computed and measured integral gas holdup; plate sparger, integral solid loading 10 Vol.-% PMMA; measured values taken from [31]

account for the different flow regimes observed in the measurements. While measurement data clearly show the division line between homogeneous and heterogeneous flow regime at a superficial gas velocity of approximately 0.03 m/s (marked by a distinct decrease of the graph's slope), the modeling calculations yield a linear relation between superficial gas velocity and integral gas holdup for the whole range under consideration. Quantitative agreement between measurement and computation results is only good for the high superficial gas velocities of 0.08 m/s and 0.09 m/s. Still, one has to keep in mind that at these high superficial gas velocities, the model has difficulties with computing the correct integral solid holdup (see section 2.2.7 and especially Fig. 2.4). Calculations for other sparger types (ring sparger, central nozzle) showed similar agreement with measurements and confirmed the general tendency of the model towards underpredicting integral gas holdup by up to 50%.

Fig. 3.17 shows the influence of solid loading on the computed integral gas holdup for the same settings as before (plate sparger, solids PMMA).

As can be seen, the influence of solid loading on computed integral gas holdup is rather small compared to the influence of superficial gas velocity. Increasing solid loading yields a slight increase in gas holdup. This result is completely opposed to measurements [31, 32] which show that at higher superficial gas velocities above 0.02 m/s, integral gas holdup decreases drastically upon addition of solid particles; only at very low gas velocities (0.02 m/s and less), no influence of solids on measured integral gas holdup was found.

This inconsistent computation of gas holdup dependency upon solid loading poses a severe downside of the implemented interaction modeling especially for the direct interactions of gas and

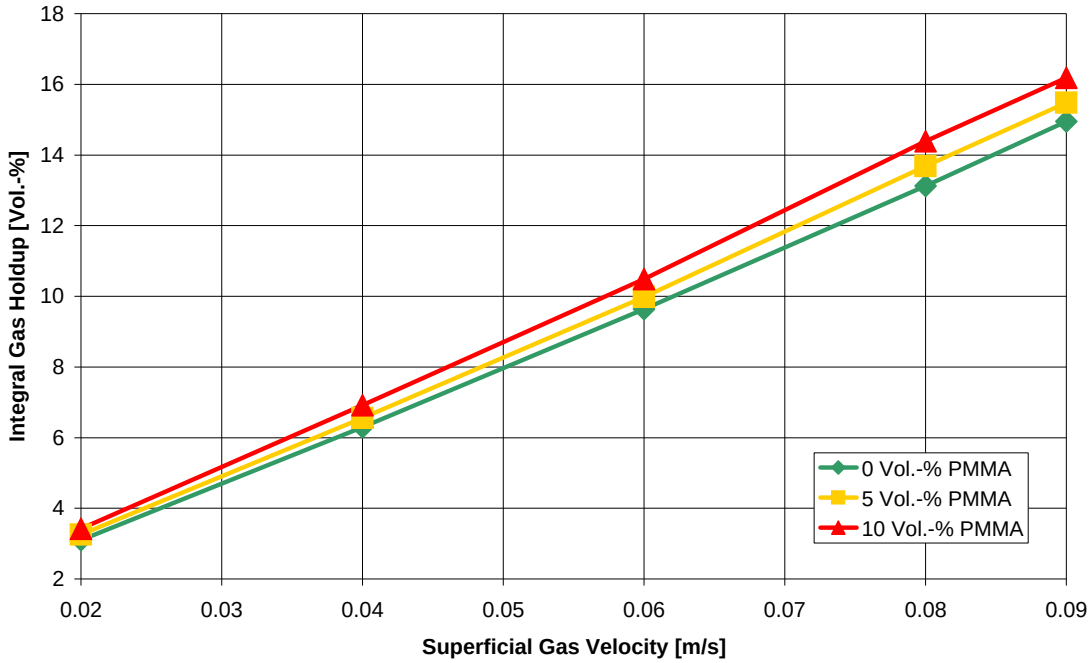

Figure 3.17: Computed integral gas holdup for different solid loadings; plate sparger, solids PMMA

solid phase. Further model improvement will be needed to correctly cover the measured effects.

3.2.3 Local Gas Holdup

3.2.3.1 Sparger Influence in Three-Phase Flow

The influence of the sparger geometry on local gas distributions has been studied experimentally in detail by Dziallas et al. [31, 32]. Fig. 3.18 and Fig. 3.19 now give an impression of how sparger modeling as described in sections 2.2.5 and 2.2.6 can capture gas distribution phenomena inside the bubble column for ring sparger and central nozzle, respectively. Three-phase flow settings are the same as with the plate sparger results presented in Fig. 3.15, i. e. 10 Vol.-% PMMA loading.

From Fig. 3.18 it can clearly be seen that with the coarse grid that has been implemented here, no satisfactory modeling of the ring sparger's influence on flow structure and dispersed phase distribution is possible. Measurement results by Dziallas et al. [31, 32] showed that the ring sparger only influences the gas distribution in the bottom half of the reactor; in the upper part, parabolic radial profiles of local gas holdup can be expected. The computational results obtained here overemphasize the sparger's influence by far yielding a local minimum of gas holdup in the reactor center that extends up to the top of the reactor. Moreover, this local gas holdup minimum corresponds to a large downflow area computed in the reactor center which at low superficial gas velocities extends to the very reactor top as well and is in clear disagreement with measurement results presented in Fig. 3.5 which show that the transition zone does at no setting extend further than for 2 m above the sparger level. Improvement of this situation can only be achieved by better modeling the actual physical effects taking place in the sparger region – the sparger ejects the air

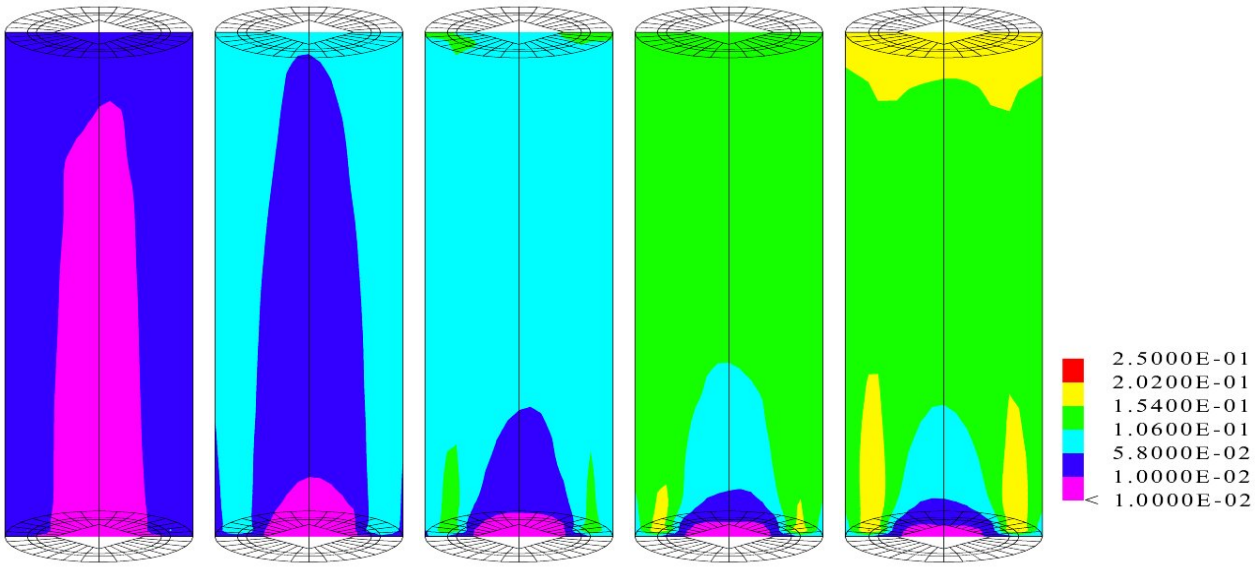

Figure 3.18: Computed gas holdup (volume fraction) with the ring sparger at an integral solid loading of 10 Vol.-% PMMA; increasing superficial gas velocities from left to right (0.02, 0.04, 0.06, 0.08, 0.09 m/s, respectively)

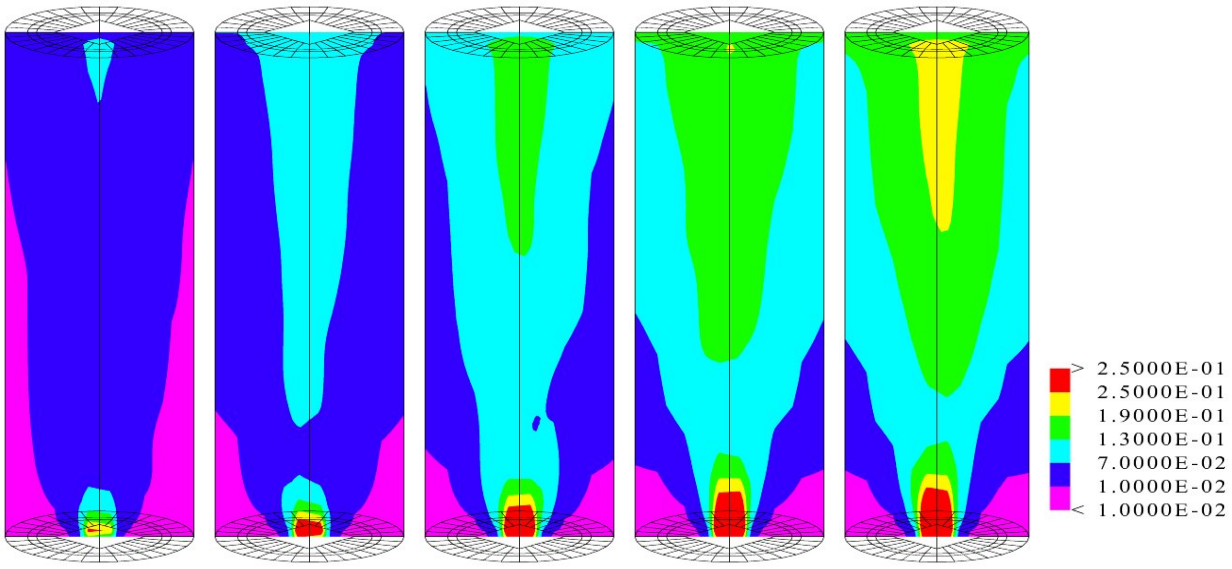

Figure 3.19: Computed gas holdup (volume fraction) with the central nozzle sparger at an integral solid loading of 10 Vol.-% PMMA; increasing superficial gas velocities from left to right (0.02, 0.04, 0.06, 0.08, 0.09 m/s, respectively)

to the bottom of the reactor directed outwards to the wall in order to improve solid fluidization. This cannot be captured by the simple patch that has been implemented in the model; for a more precise sparger modeling, though, a significantly finer grid structure is necessary.

Modeling results for local gas distribution as induced by the central nozzle sparger are given in Fig. 3.19 for different superficial gas velocities and show a much better agreement with measurement results. The model very well captures the formation of an area of extremely high gas holdup just above the sparger and a region with almost no gas between nozzle and the bottom part of the reactor wall which has been experimentally determined by Dziallas et al. [31, 32]. The development of a parabolic radial gas holdup profile higher above the plate sparger and the superimposed increase of local gas holdup with increasing vertical position due to gas expansion is very well captured by the model. This means that for simple sparger geometries, the model implemented here can very well describe the dependency of local gas holdup on superficial gas velocity. Results on solid fluidization for the same sparger geometries as considered here will be given in section 3.2.4.

3.2.3.2 Solids Influence in Three-Phase Flow

Investigations on the influence of solid loading on computed integral gas holdup have already been presented in section 3.2.2 (Fig. 3.17) and have shown that in disagreement with measurement results the effect of increasing solid loading on integral gas holdup is very small. Fig. 3.20 shows that the almost equal computed integral gas holdups shown in Fig. 3.17 for different solid loadings are the result of almost equal local gas distributions.

From Fig. 3.20 it can be seen that the slight increase in integral gas holdup with increasing solid loading is mainly due to an increase in local gas holdup at the bottom section of the reactor. This result is hard to explain and rather unsatisfactory showing that interaction modeling between gas and solid phase as implemented here obviously is not yet able to cover all phenomena necessary to correctly model not only the influence of the gas bubbles on solid fluidization but also the reverse influence of solid loading on gas holdup.

3.2.4 Local Solid Holdup

Correct prediction of local solid holdups is one of the central issues in three-phase flow calculations. The direct gas-solid phase interaction model implemented here has been developed for the plate sparger (see section 3.2.1). The influence of the ring sparger on solid fluidization with varying superficial gas velocities is shown in Fig. 3.21.

The general effect of decreasing solid fluidization with increasing superficial gas velocity that has been measured [31, 32] and computed for the plate sparger (see Fig. 3.14) can also be found with the ring sparger. Here, fluidization is fairly good at the lowest superficial gas velocity of

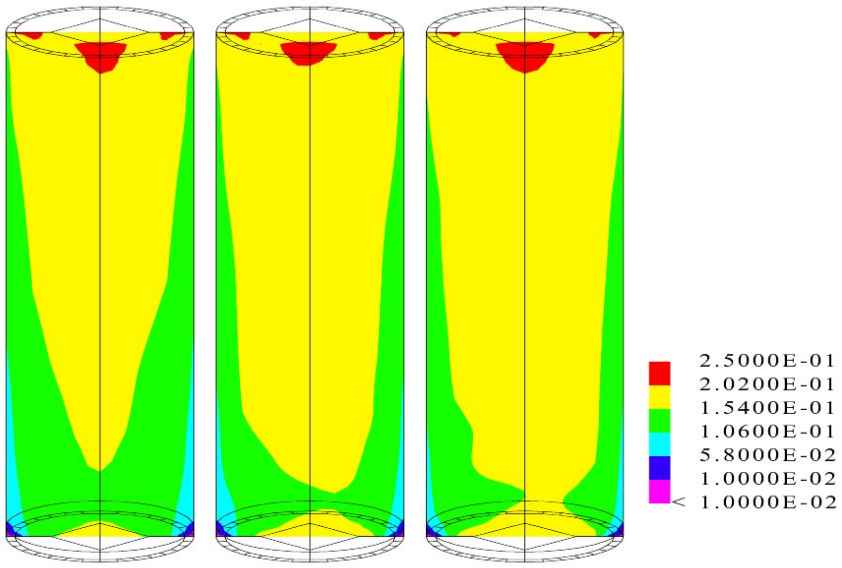

Figure 3.20: Computed gas holdup (volume fraction) with the plate sparger at a superficial gas velocity of 0.09 m/s and increasing integral solid loadings (0, 5, 10 Vol.-% PMMA from left to right)

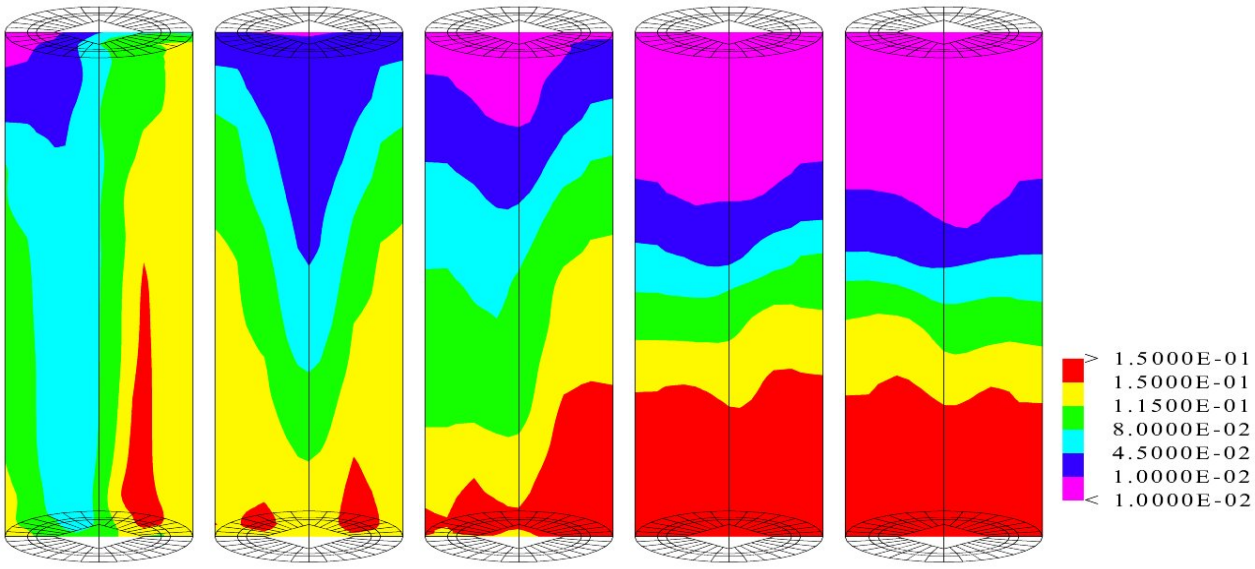

Figure 3.21: Computed solid holdup (volume fraction) with the ring sparger at an integral solid loading of 10 Vol.-% PMMA; increasing superficial gas velocities from left to right (0.02, 0.04, 0.06, 0.08, 0.09 m/s, respectively)

0.02 m/s; the large degree of unsymmetry found at this gas velocity is due to insufficient averaging time. At a superficial gas velocity of 0.04 m/s, the oscillation frequency of the bubble hose is probably somewhat higher than at 0.02 m/s leading to a larger number of oscillation periods being included in the time averaging thus yielding a better symmetry. Most significant here is that a local minimum of solid holdup develops in the upper center of the reactor. This is opposed to measurement results by Dziallas et al. [31, 32] who found lowest values of solid holdup at the upper edge of the reactor and a local maximum in the upper center (with the ring sparger as well as with the plate sparger). Reason for this wrong-computed solid distribution can be found in the wrong-computed flow field (downflow in the reactor center almost to the top of the reactor) due to the insatisfactory sparger modeling. In general, especially with higher superficial gas velocities, computed fluidization with the ring sparger is not as good as with the plate sparger and also not as good as measured fluidization.

The opposite occurs with respect to computed fluidization with the central nozzle. Fig. 3.22 shows local solid holdups for varying superficial gas velocities in the bubble column equipped with the central nozzle at an integral solid loading of 10 Vol.-% PMMA.

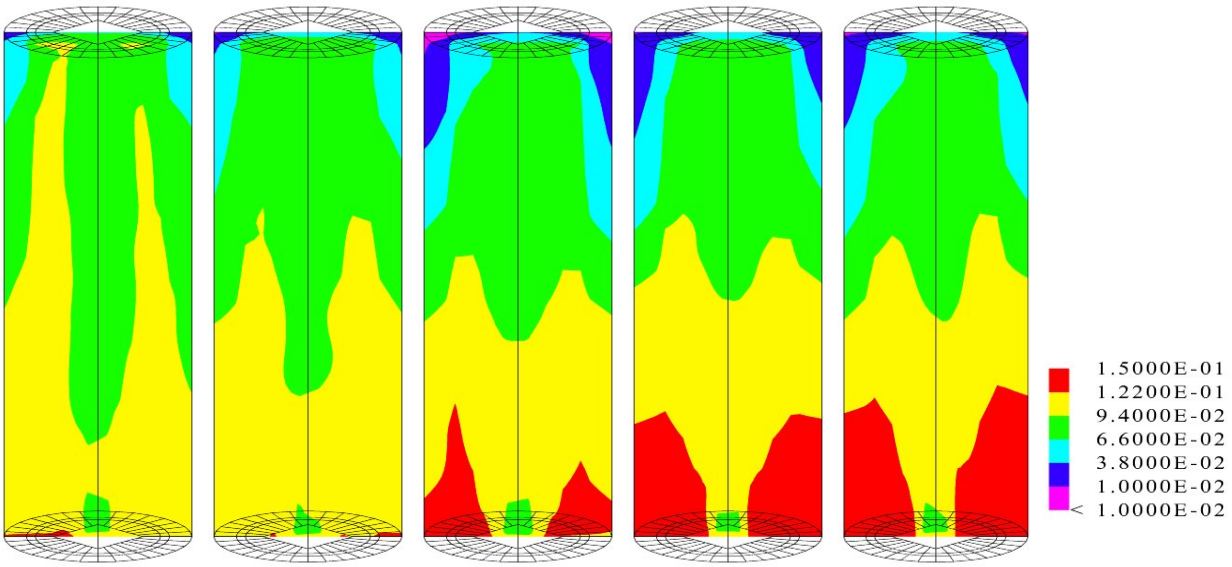

Figure 3.22: Computed solid holdup (volume fraction) with the central nozzle sparger at an integral solid loading of 10 Vol.-% PMMA; increasing superficial gas velocities from left to right (0.02, 0.04, 0.06, 0.08, 0.09 m/s, respectively)

In comparison to measurement results, computed fluidization especially at the low superficial gas velocities of 0.02 and 0.04 m/s is far too good. Measurements showed [31, 32] that at these low gas velocities, hardly any PMMA solid is fluidized at all and even at 0.09 m/s, a lot of solid is left unfluidized at the reactor bottom.

Conclusion from these observations on solid fluidization has to be that probably one fixed

model for the momentum exchange between gas and solid phase is not sufficient for the correct computation of flow fields with different sparger geometries. The interaction model implemented here has been fitted to measurement results obtained with the plate sparger; for correct modeling of solid fluidization with ring sparger and central nozzle, a re-fitting of the exchange parameter $c_{g,s} \cdot u_{slip,g,s}$ is probably unavoidable.

3.2.5 Density of Gas-Liquid Mixture

In section 3.2.1, the adverse influence of increasing superficial gas velocity on solid fluidization was described when fluidization was almost homogeneous already at low superficial gas velocities. This effect occurred in measurements of local solid holdup in bubble columns [31, 32] and was reproduced by modeling calculations as well. A possible reason for this unexpected and usually unwanted effect may be found in the density of the gas-liquid mixture inside the reactor.

An important parameter in solid fluidization is the terminal settling velocity of the particles. It depends on particle size, shape and density as well as on parameters like density and viscosity of the surrounding continuous phase. In three-phase flow, this surrounding continuous phase consists of a mixture of gas and liquid; the particles no longer sink in pure liquid but effective continuous phase viscosity and density are reduced by the presence of gas. This effect increases with increasing gas holdup and leads to a higher effective terminal settling velocity at higher gas holdups. Fig. 3.23 shows local gas-liquid mixture density for increasing superficial gas velocities (corresponding to increasing gas holdups) computed from the measured holdup values of [31] for the case of the plate sparger at an integral solid loading of 10 Vol.-% PMMA.

It is evident that with increasing superficial gas velocity, the gas-liquid mixture density decreases. Especially in the upper regions of the reactor center, mixture density decreases with increasing superficial gas velocity to values as low as 700 kg/m^3. In these areas of low mixture density, particles will settle faster yielding a deterioration of fluidization. Fig. 3.24 shows that the same tendency is given by the corresponding modeling results.

From Figs. 3.23 and 3.24 it can be concluded that gas-liquid mixture density is of important influence for solid fluidization. Still, certain effects can not be explained solely from this parameter: Measurements and computation show that decrease in solid holdup with increasing superficial gas velocity is especially drastic at the upper reactor edge. This does not correspond to the mixture density observations which would indicate a most significant decrease in solid holdup in the upper reactor center. Liquid velocity measurements as presented in section 3.1.2.1 indicate that a region of high downflow velocities exists at the upper reactor edge. Low gas holdup in this area means that much solid can be transported downwards; yet, due to the high gas holdup in the upper reactor center, not as much solid is transported upwards. This effect increases with increasing superficial gas velocity leading to the observed almost solid-less region at the upper reactor edge.

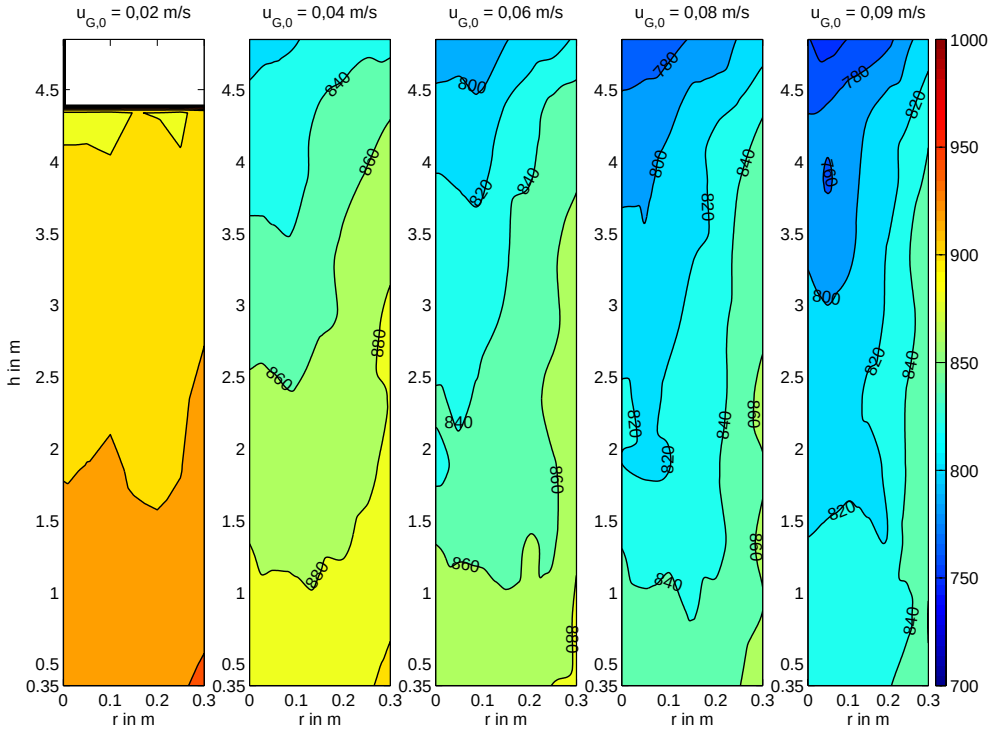

Figure 3.23: Measured gas-liquid mixture density in kg/m^3 with the plate sparger at an integral solid loading of 10 Vol.-% PMMA; increasing superficial gas velocities from left to right; values computed from [31]

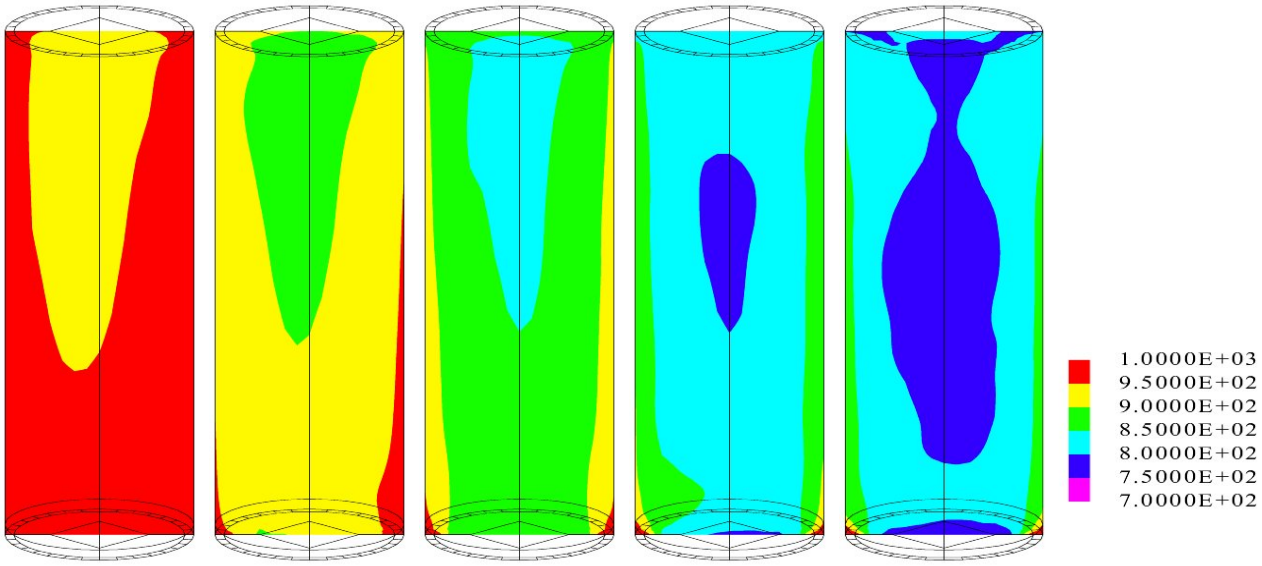

Figure 3.24: Computed gas-liquid mixture density (kg/m^3) with the plate sparger at an integral solid loading of 10 Vol.-% PMMA; increasing superficial gas velocities from left to right (0.02, 0.04, 0.06, 0.08, 0.09 m/s, respectively)

3.2.6 Local Liquid Flow Velocities

As with the measurements presented in section 3.1, emphasis in the evaluation of computed liquid velocities will mainly be put on radial and centerline profiles of mean axial velocity.

3.2.6.1 Radial Profiles of Axial Velocities

Fig. 3.25 shows radial profiles of computed mean axial liquid velocities in three-phase flow for the same settings as with the measurement results presented in Fig. 3.6, i. e. superficial gas velocities ranging from 0.02 to 0.09 m/s, 10 Vol.-% PMMA loading, vertical position 2.35 m above the plate sparger.

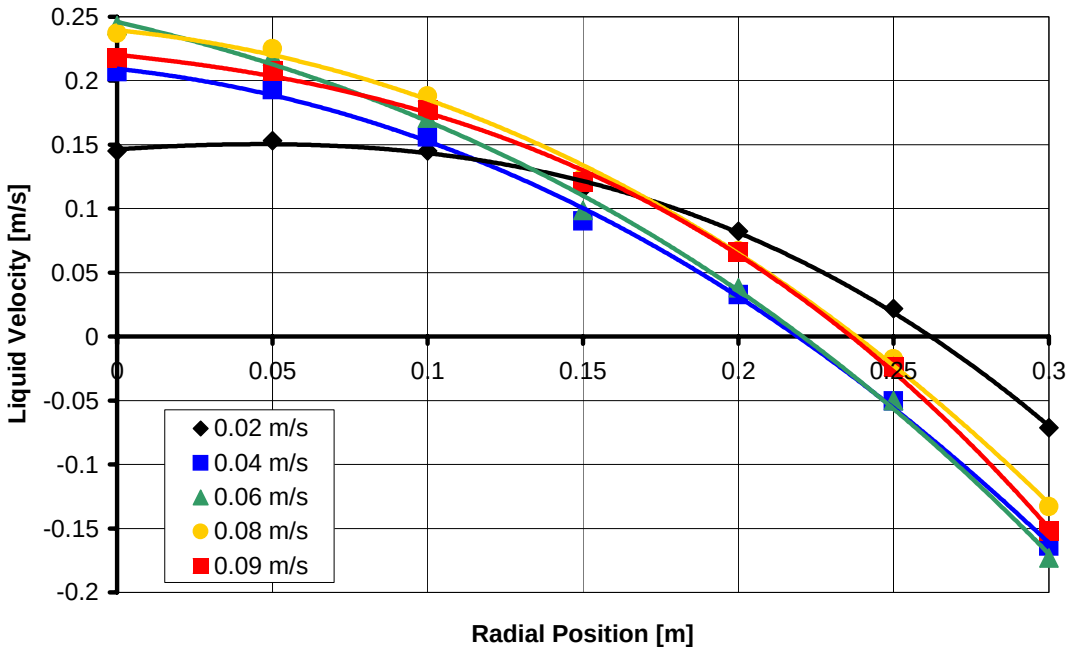

Figure 3.25: Computed axial liquid velocities for different superficial gas velocities, 2.35 m above plate sparger, 10 Vol.-% PMMA (corresponding measurements see Fig. 3.6)

It can be observed that the general trend of increase in liquid velocity with increasing superficial gas velocity that has been found with the measurements in Fig. 3.6 can well be reproduced by the CFD model. An increase in superficial gas velocity beyond 0.04 m/s does not lead to a further increase in mean liquid velocity but rather to increased fluctuational velocities and turbulent dissipation. Still, the order of magnitude of the computational results is unsatisfactory; computed velocity values are only about half as high as measured ones. Possible reasons for this behaviour can most likely be found in several model assumptions made here. For example, bubble size is of large influence on the rise velocity of bubbles which in turn influences liquid velocity; in the model as implemented here, formation of large bubbles in the heterogeneous flow regime has been neglected completely yielding too low bubble rise velocities. The chosen turbulence model also has

large influence on liquid velocities via the computed turbulent viscosity; this quantity is possibly computed too high by the model leading to low mean liquid velocities.

3.2.6.2 Centerline Axial Velocities

As with the measurements presented above, a good overview of the computed liquid circulation over the whole height of the bubble column can be gained from the centerline liquid velocities. Fig. 3.26 shows centerline velocities for the same settings as with the radial profiles considered in the previous section (Fig. 3.25, plate sparger, 10 Vol.-% PMMA).

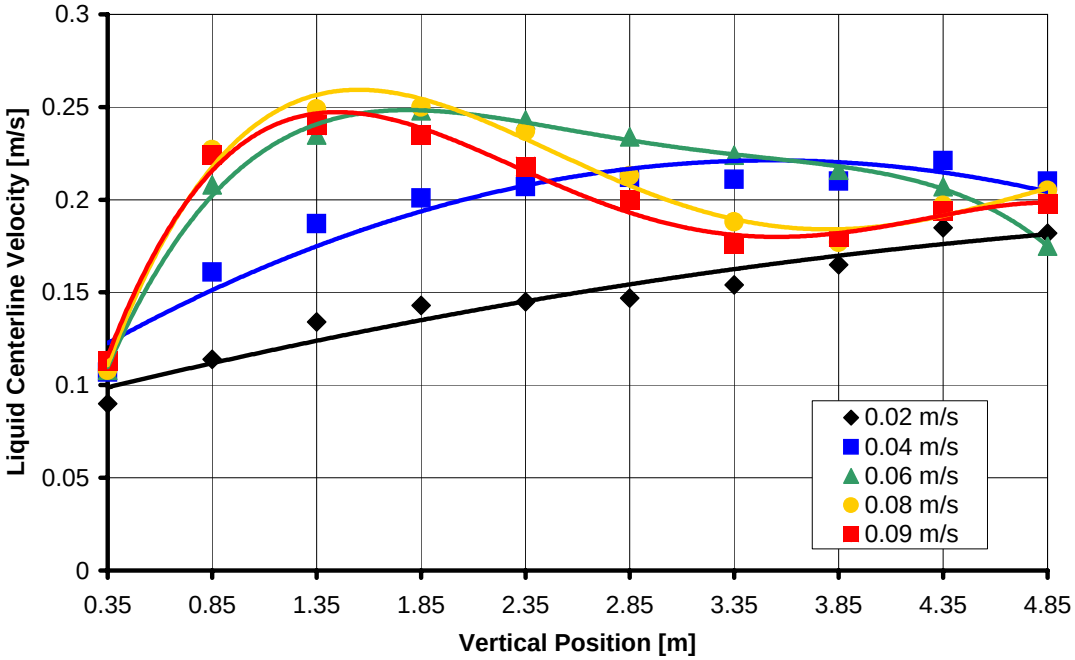

Figure 3.26: Computed axial liquid centerline velocities for different superficial gas velocities, plate sparger, 10 Vol.-% PMMA

The insufficient computed averaging time clearly manifests itself in the s-shaped or (at a superficial gas velocity of 0.02 m/s) with increasing vertical position in the reactor almost linearly increasing velocity profiles. Only the graphs for the superficial gas velocities of 0.04 m/s and 0.06 m/s show the expected shape with a maximum in the vertical reactor center and minima at the sparger and the degassing area. At the other gas velocities, oscillation frequencies of the bubble plume are such that during the averaging time, no sufficient number of periods has been covered to achieve axisymmetry. Still, basic trends that have been deduced from the radial profiles in Fig. 3.25 can be confirmed here. Most important, at no location in the reactor the upflow velocity exceeds a value of approximately 0.25 m/s which is only 50 % of the value that would have been expected from the measurements (compare Fig. 3.8 for measured values at superficial gas velocities of 0.02 m/s and 0.09 m/s). Possible reasons for this have already been discussed in the previous section.

The computed influence of solid loading on centerline profiles of axial liquid velocity can be seen from Fig. 3.27 for 2 superficial gas velocities with the plate sparger (as before).

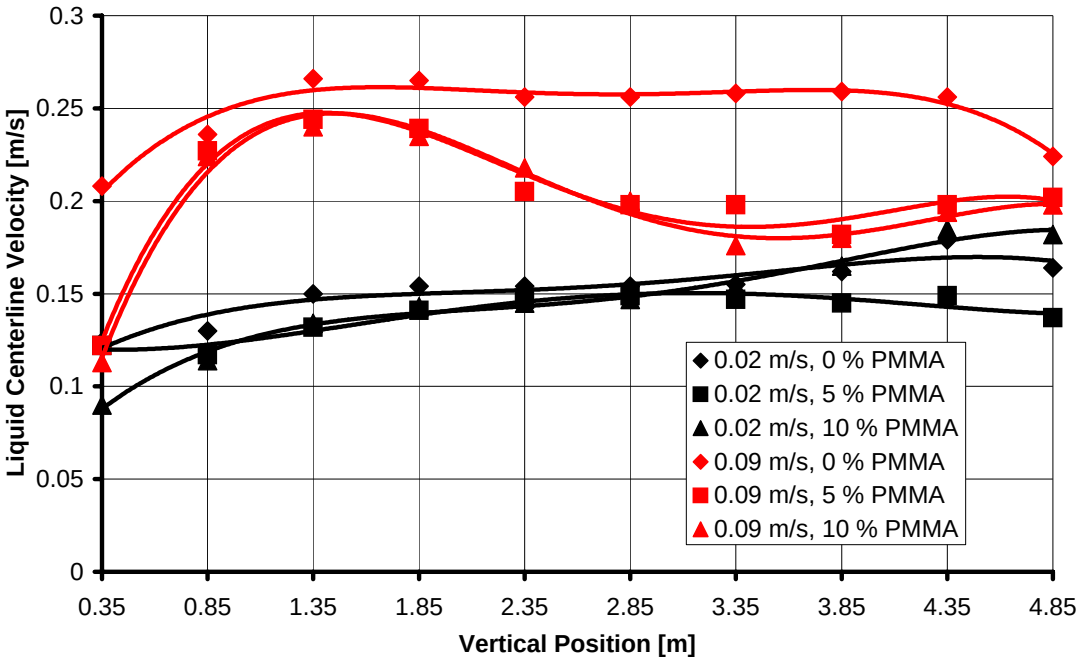

Figure 3.27: Computed axial liquid centerline velocities for different superficial gas velocities and solid loadings, plate sparger (corresponding measurements see Fig. 3.8)

In general, it can be seen from Fig. 3.27 that the computed influence of solid addition on liquid phase velocities is rather small. In comparison to measurement data in Fig. 3.8, maximum values of computed liquid centerline velocities especially in the two-phase case reach only about 30 % of the expected ones which is even worse than in three-phase flow. Since the reason for this cannot be found in the implementation of the gas-solid interaction modeling, other error sources like bubble sizes or turbulence modeling appear to be of pre-eminent importance for further model improvement.

Quantitatively, influence of solid addition on computed liquid velocity is smallest for the smallest superficial gas velocity of 0.02 m/s. While in two-phase flow the highest velocities can be observed, no clear trend can be found with gradually adding solids due to the insufficient long-time averaging of the computed values leading to intersecting graphs of the flow profiles. At the highest superficial gas velocity of 0.09 m/s, the same observation can be made. Two-phase flow delivers highest liquid velocities (even if they are still too low) and the most reasonable profile shape: Obviously, bubble plume oscillation frequency in this case was such that the averaging time was long enough to deliver useful steady-state values (constant over a wide range of vertical positions, decreasing only in the sparger and degassing area). In three-phase flow, velocity profiles are s-shaped due to insufficient time-averaging with maximum values slightly below the two-phase ones; graphs for 5 and 10 % solid loading are almost identical.

For a quantitative verification of measurement and modeling results, Riquarts's correlation

as introduced for two-phase flow in section 2.3.3.1 (eqn. 2.30) has been used. Since Riquarts's correlation is assuming constant centerline velocities not depending on vertical position in the reactor, its values are compared to measured and computed values at a vertical position 2.35 m above the sparger, i. e. in the vertical center of the reactor where sparger and degassing area influences should be vanishing. Fig. 3.28 shows measured and computed values of axial liquid centerline velocities in two-phase flow with the plate sparger compared to values given by eqn. 2.30.

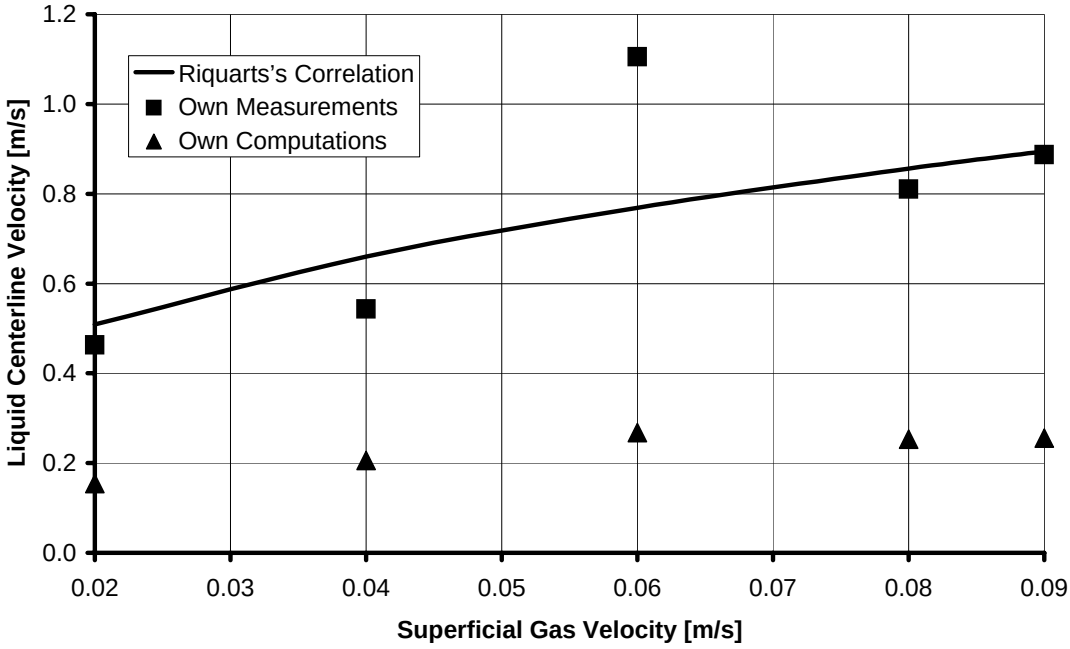

Figure 3.28: Computed and measured axial liquid centerline velocities 2.35 m above the plate sparger for different superficial gas velocities in two-phase flow compared to Riquarts's correlation [97]

From Fig. 3.28 it can be seen that measured values agree very well with values delivered by Riquarts's correlation while the computed values are significantly lower. This gives reason for the assumption that values measured using the Electrodiffusion Method (EDM) are actually representative for the flow structure in two- and three-phase bubble columns even if scatter in the data is somewhat high. With the modeling, these measured values can thus be used as a good basis for the verification of further refined approaches.

4 Conclusions and Discussion

Measurement and computational results presented in this project report show that only a reasonable combination of these two approaches can deliver new insights into physical phenomena and finally yield tools helpful in reactor design and scale-up. Measurement results of local dispersed phase holdups and liquid velocities delivered a strong foundation for CFD model development and verification documenting possibilities and limitations of implemented modeling strategies.

In two-phase flow, EDM measurements of liquid flow velocities clearly showed the influence of sparger geometry and superficial gas velocity on liquid circulation in the reactor. The common radial profile of axial liquid velocity far away from sparger and degassing zone influence exhibits a parabolic to almost linear shape with an upflow maximum in the center and a downflow region near the wall. Mean velocities are almost independent from superficial gas velocity in the heterogeneous flow regime at superficial gas velocities beyond 0.04 m/s; there, additional energy input with increasing superficial gas velocity only yields increasing fluctuational velocities finally leading to increased turbulent dissipation. Sparger influence is very distinct with ring sparger and central nozzle where the influence on radial profile shape can be observed over the complete bottom half of the reactor; yet, the ring sparger and central nozzle influence the upper regions as well by means of introducing fast rising large bubbles in the reactor center leading to sustainedly increased axial centerline velocities in comparison to the plate sparger.

Measurements of liquid velocities in three-phase flow showed that the formation of large bubbles is suppressed when solids are added to the reactor contents leading to drastically reduced liquid velocities especially in the reactor center and thus to parabolic rather than linear radial velocity profiles. Adding 5 Vol.-% of solids yielded this significant decrease in liquid velocities while adding a further 5 Vol.-% to obtain a total solid loading of 10 Vol.-% did not lead to a further decrease of liquid velocity but rather induced a slight increase in liquid velocities over the 5 Vol.-% solid values. Fluctuational velocities were found to be ranging in the same order of magnitude as mean velocities for all solid loadings under investigation at most positions inside the reactor (except for those where mean velocities were close to zero).

CFD calculations have proved the necessity of three-dimensional, transient computations including a turbulence model and accounting for direct momentum exchange between all three

involved phases. Implementation of a rather simple drag law approach for the direct momentum exchange between gas and solid phase introducing just one parameter fitted to measured local solid holdups gave correct solid fluidization even at low superficial gas velocities. It also yielded correct computation of the adverse influence of increasing superficial gas velocity on solid fluidization when solid was almost homogeneously fluidized already at low gas velocities. Shortcomings of the model as implemented here are still to be found with its inability to correctly account for the flow regimes characteristic for bubble columns and with the serious underprediction of liquid velocities in general.

With measurements as well as with computations, thus, a lot of room for improvements is given. Liquid flow velocity measurements using the Electrodiffusion Method (EDM) as implemented here suffer from severe problems in three-dimensional flow since calibration can only be performed for two-dimensional flow settings. The screens that have been attached to the needle electrode during the measurements carried out in this projects are not really a satisfying solution since they do introduce – if only small – unwanted flow field disturbances. The almost similar two-dimensional measurement technique presented by Hashiba and Kojima [46] introduces a very efficient data evaluation based on autocorrelation algorithms which makes the tedious electrode calibration procedure unnecessary; according to the authors' suggestions, the method could actually be extended to deliver real three-dimensional velocity vectors thus enabling a much better determination of the three-dimensional flow structures in bubble columns.

Modeling improvement could clearly start with improved computer hardware enabling computations on finer numerical grids leading especially to improved sparger modeling – the ring sparger then could actually be modeled with its original geometry ejecting air towards the reactor bottom and not as a flat patch. Besides this obvious approach, a large number of modeling details calls for improvement of the implemented physics.

Bubble- and particle-induced liquid turbulence have been neglected completely in this project. Literature reports on two-phase flow have shown the importance of including at least the bubble-induced turbulence by means of introducing source terms into the k-ε turbulence model (eqn. 2.24 and eqn. 2.25, respectively). Models for these bubble effects are available [92, 122], particle-induced turbulence should be even easier to implement. Worth considering is furthermore the implementation of a turbulence model that can take anisotropy into account, which is not possible with the k-ε model. A Reynolds stress model as described in section 2.2.4.1 should be better fit to cover anisotropy effects encountered in bubble columns.

When it comes to interphase drag computation, all momentum exchange laws as implemented here assume bubbles to be spherical and non-deformable. In reality, this assumption only holds for very small bubbles; the bubbles encountered in the reactor under consideration have a minimum size of about 5 mm where deformation already starts. Larger bubbles take on an ellipsoidal shape as can clearly be observed in the transparent pilot-plant bubble column. Models that allow for the

implementation of these effects are available [22] and should be included in further computations. Bubble size itself is of important influence for all flow processes in the reactor; setting it to a constant value means neglecting all effects of coalescence, bubble-breakup and expansion due to hydrostatic pressure decrease with increasing vertical position in the reactor and thus can be held responsible for the model's actual inability to account for the flow regime transitions observed in the measurements. Bubble size models like the simple two-bubble-class model by Krishna et al. [60, 61] or the more sophisticated bubble size transport equation developed by Lehr and Mewes [66] are available and should be tested.

Other bubble effects such as added mass force (including the liquid mass in the bubble wake into the computation of the bubble velocity and acceleration) and swarm effects leading to increased bubble rise velocities should be incorporated as well. With all these models, it is important to keep in mind that their effect on centerline liquid velocity and integral gas holdup can act in different directions. Large fast-rising bubbles e. g. lead to higher centerline liquid velocities (which is desired since the model in its current state underpredicts measured liquid velocities); yet, at the same time they yield a reduced bubble residence time inside the reactor leading to reduced integral gas holdup (which is unwanted since the model right now also underpredicts integral gas holdup).

Solid viscosity has been shown to have no influence on computed flow field and dispersed phase distributions over a wide range of values; therefore, it has been set constant to the value of water. While this works reasonably here, a more physically funded approach for its computation would be desirable. A possible extension of Gidaspow's approach for computation of solid viscosity in fluidized beds [36] should therefore be taken into consideration.

Modeling of direct dispersed phase interaction leaves room for improvement as well. Right now, the fitting parameter $c_{g,s} \cdot u_{slip,g,s}$ in eqns. 2.20 and 2.21 lumps together all influences that are not captured by other models, e. g. those due to bubble size considerations. Thus, an implementation of other turbulence or bubble size models will most certainly make a refitting of the direct dispersed phase interaction model necessary. From a physical point of view, the inclusion of other effects than drag would be interesting as well, e. g. could particle-bubble impacts be included. This approach could be extended and generalized to include particle-wall or bubble-wall impacts as well.

From the numerics point of view, the AMG algorithm as implemented here does not represent the best possible approach to solving the systems of equations resulting from multiphase flow modeling. Thus, a definite demand for the development of new, more efficient algorithms is given [53] that can only be satisfied in close cooperation of mathematicians, physicists and engineers. From a computational point of view, parallel computation with distributed systems in a network of common PC workstations would be very desirable since PC clusters are significantly cheaper than shared-memory systems of comparable computational power and are readily available for overnight use in most office environments; still, with the common commercially available CFD

codes, this feature is only marginally developed and difficult to handle or not implemented at all.

With such improvements in modeling and computation, the aim of developing a practical tool for design and scale-up of multiphase flow reactor systems should come into close reach. Hopefully, in the not too far future, CFD will become a tool as widely accepted in chemical and biochemical engineering applications as process modeling using e. g. software packages like Aspen is already; the integration of those two modeling streams is one of the important tasks of the future.

5 Nomenclature

5.1 Latin Symbols

Symbol	Units	Explanation
A	m^2	Particle area projected in flow direction
$A_{Reactor}$	m^2	Reactor cross-sectional area
$A_{Sparger}$	m^2	Free Sparger cross-sectional area
C_D	1	Friction factor
$C_{\varepsilon 1}$	1	Constant in k-ε model
$C_{\varepsilon 2}$	1	Constant in k-ε model
C_μ	1	Constant in k-ε model
c_g	N/m^3	Coefficient in gas phase momentum sink term for direct dispersed phase interaction modeling
$c_{g,s}$	1	Constant for direct dispersed phase interaction model with slip-velocity dependent source terms
$c_{g,s,c}$	N/m^3	Constant for direct dispersed phase interaction model with constant source terms
c_s	N/m^3	Coefficient in solid phase momentum source term for direct dispersed phase interaction modeling
$c_{\alpha,\beta}$	$kg/(m^3\ s)$	Momentum exchange parameter
D	m	Column inner diameter
$D_{ax,\alpha}$	m^2/s	Axial dispersion coefficient of phase α
D_P	N	Single particle drag force
$D_{rad,\alpha}$	m^2/s	Radial dispersion coefficient of phase α
$\mathbf{D}_{\alpha,\beta}$	N/m^3	Drag force per unit volume vector
d_P	m	Particle diameter
G	$J/(m^3 s)$	Turbulence production term

Symbol	Units	Explanation
$g_{(i)}$	m/s^2	Gravitational acceleration (in i-direction)
h	m	Spatial coordinate, vertical direction
k	m^2/s^2	Turbulent kinetic energy
$M_{g,i,d}$	N/m^3	Direct gas-solid momentum interphase transfer term, gas phase, direction x_i
$M_{s,i,d}$	N/m^3	Direct gas-solid momentum interphase transfer term, solid phase, direction x_i
$M_{\alpha,i}$	N/m^3	Momentum interphase transfer term, continuous phase α, direction i
$M_{\beta,i}$	N/m^3	Momentum interphase transfer term, dispersed phase β, direction i
$\tilde{M}_g$	kg/kmol	Molar mass of gaseous phase
N_P	1	Number of dispersed phases in the calculation
$n_{P,V}$	1/m^3	Number of particles per unit volume
p	N/m^2	Hydrostatic pressure
p_0	N/m^2	Environment hydrostatic pressure
p_{inlet}	N/m^2	Hydrostatic pressure at the reactor inlet
Re	1	Reynolds number
R	m	Column inner radius
r	m	Spatial coordinate, radial direction
$\tilde{R}$	kJ/(kmol K)	Gas constant
$S_{l,k}$	J/(m^{3}s)	Source term in kinetic energy equation (liquid phase)
$S_{l,\varepsilon}$	J/(m^{3}s^2)	Source term in kinetic dissipation equation (liquid phase)
t	s	Time
δt	s	Time increment
$\mathbf{u}$	m/s	Flow velocity vector
$\bar{\mathbf{u}}$	m/s	Mean flow velocity vector
$\mathbf{u}'$	m/s	Fluctuational flow velocity vector
$\mathbf{u}''$	m/s	Fluctuational flow velocity vector due to bubble effects
u	m/s	Flow velocity
$u_{B,\infty}$	m/s	Terminal bubble rise velocity
$\mathbf{u_g}$	m/s	Gas flow velocity vector
$u_{G,0}$	m/s	Superficial gas velocity at the reactor top
$u_{g,i}$	m/s	Gas flow velocity in i-direction

Symbol	Units	Explanation
$u_{g,inlet}$	m/s	Prescribed axial gas flow velocity at the reactor inlet
$u_{l,ax,max}$	m/s	Maximum centerline axial liquid velocity
$u_{l(,i)}$	m/s	Liquid flow velocity (in i-direction)
$\overline{u_i u_j}$	m^2/s^2	Component of Reynolds Stress tensor
$\mathbf{u_s}$	m/s	Solid flow velocity vector
$u_{s,i}$	m/s	Solid flow velocity in i-direction
$u_{slip,g,s}$	m/s	Slip velocity between gas and solid phase in direct dispersed phase interaction modeling
$u_{PMMA,\ settling}$	m/s	PMMA particle settling velocity
$\mathbf{u}_\alpha$	m/s	Flow velocity vector of continuous phase α
u_α	m/s	Flow velocity of continuous phase α
$u_{\alpha,i}$	m/s	Flow velocity of continuous phase α in i-direction
$u_{\alpha,j}$	m/s	Flow velocity of continuous phase α in j-direction
$\mathbf{u}_\beta$	m/s	Flow velocity vector of dispersed phase β
u_β	m/s	Flow velocity of dispersed phase β
$u_{\beta,i}$	m/s	Flow velocity of dispersed phase β in i-direction
$u_{\beta,j}$	m/s	Flow velocity of dispersed phase β in j-direction
$v_{ax,\alpha,c}$	m/s	Convective axial velocity of phase α
V_C	m^3	Grid cell volume
V_P	m^3	Particle volume
w_{Fl}	m/s	Liquid velocity
x	m	Spatial coordinate, axial direction in dispersion model
x_i	m	Spatial coordinate
x_j	m	Spatial coordinate

5.2 Greek Symbols

Symbol	Units	Explanation
α		Index denoting a continuous phase
β		Index denoting a dispersed phase
ε	m^2/s^3	Turbulent kinetic dissipation (liquid phase)
$\varepsilon_{g,inlet}$	1	Gas volume fraction at the reactor inlet
ε_α, ε_β	1	Volume fraction of phase α respectively β (gas g / liquid l / solid s)
κ	1	Constant in k-ε-model (Von Karman constant)
μ	Pa s	(Efficient) dynamic viscosity
μ_l	Pa s	(Efficient) liquid dynamic viscosity
$\mu_{l,lam}$	Pa s	Laminar part of efficient liquid dynamic viscosity
$\mu_{l,turb}$	Pa s	Turbulent part of efficient liquid dynamic viscosity
μ_α	Pa s	Effective dynamic viscosity of continuous phase α
$\mu_{\alpha,lam}$	Pa s	Laminar dynamic viscosity of continuous phase α
$\mu_{\alpha,turb}$	Pa s	Turbulent dynamic viscosity of continuous phase α
μ_β	Pa s	Dynamic viscosity of dispersed phase β
ρ_g	kg/m^3	Density of gaseous phase
ρ_l	kg/m^3	Density of liquid phase
ρ_α	kg/m^3	Density of continuous phase α
ρ_β	kg/m^3	Density of dispersed phase β
σ_k	1	Constant in k-ε-model (turbulent Prandtl number for k)
σ_ε	1	Constant in k-ε-model (turbulent Prandtl number for ε)
τ	s	Time (integration variable in averaging procedure)
ω	s^{-1}	Turbulence frequency

Bibliography

[1] Al-Qodah, Z.; Al-Hassan, M.:
Phase Holdup and Gas-to-Liquid Mass Transfer Coefficient in Magneto Stabilized G-L-S Airlift Fermenter, Chemical Engineering Journal 79 (2000), 41-52

[2] Anderson, J. D.:
Computational Fluid Dynamics: The Basics with Applications,
McGraw-Hill, New York (1995)

[3] Bauer, M.; Eigenberger, G.:
Multiscale Modeling of Hydrodynamics, Mass Transfer and Reaction in Bubble Column Reactors, Chemical Engineering Science 56 (2001), 1067-1074

[4] Becker, S.:
Experimentelle Untersuchungen von Blasensäulen als Basis für detaillierte Modellrechnungen, Ph. D. Thesis, University of Stuttgart / Germany, VDI-Verlag (1997)

[5] Becker, S.; de Bie, H.; Sweeney, J.:
Untersuchung der Strömungsstruktur in einer begasten Flachapparatur mit Laser-Doppler-Anemometrie, Chemie Ingenieur Technik 71 (1999), 852-856

[6] Becker, S.; De Bie, H.; Sweeney, J.:
Study on the Flow Structure in an Aerated Flat Apparatus Using Laser Doppler Anemometry, Chemical Engineering and Technology 23 (2000) 3, 222-226

[7] Birthig, A.; Lauschke, G.; Schierholz, W. F.; Beck, D.; Maul, C.; Gilbert, N.; Wagner, H.-G.; Werninger, C. Y.:
CFD in der Chemischen Verfahrenstechnik aus industrieller Sicht,
Chemie Ingenieur Technik 72 (2000) 3, 175-193

[8] Boivin, M.; Simonin, O.; Squires, K. D.:
Direct Numerical Simulation of Turbulence Modulation by Particles in Isotropic Turbulence, Journal of Fluid Mechanics 375 (1998), 235-264

[9] Boivin, M.; Simonin, O.; Squires, K.:
On the Prediction of Gas-Solid Flows with Two-Way Coupling Using Large Eddy Simulation,
Physics of Fluids 12 (2000) 8, 2080-2090

[10] Braeske, H.; Brenn, G.; Domnick, J.; Durst, F.; Melling, A.; Ziema, M.:
Erweiterte Phasen-Doppler-Anemometrie zur Untersuchung dreiphasiger Strömungen,
Chemie Ingenieur Technik 70 (1998) 6, 737-741

[11] Brauer, H.:
Turbulenz in mehrphasigen Strömungen,
Chemie Ingenieur Technik 51 (1979), 934-948

[12] Briggs, W. L.; Henson, V. E.; McCormick, S. F.:
A Multigrid Tutorial,
2nd Edition, SIAM, Philadelphia / Pennsylvania (2000)

[13] Bröder, D.; Sommerfeld, M.:
Simultaneous Measurements of Continuous and Dispersed Phase in Bubble Columns by PDA,
Proceedings Ninth International Symposium on Applications of Laser Techniques to Fluid Mechanics, Lisbon / Portugal (1998)

[14] Brück, F.-J.:
Untersuchungen mit Mikro-Sonden zum Einfluß verschiedener physikalischer Eigenschaften suspendierter Feststoffe auf die fluiddynamischen Funktionen von Blasensäulen,
Ph. D. Thesis, RWTH Aachen / Germany (1985)

[15] Brücker, C.:
3-D Scanning-Particle-Image-Velocimetry: Technique and Application to a Spherical Cap Wake Flow, Applied Scientific Research 56 (1996) 2-3, 157-180

[16] Buchholz, R.; Zakrzewski, K.; Schügerl, K.:
Meßtechniken zur Bestimmung der Eigenschaften von Blasen in Blasensäulen,
Chemie Ingenieur Technik 51 (1979) 6, 568-575

[17] Buchholz, R.; Franz, K.; Onken, U.:
Entwicklung einer richtungscharakteristischen Meßtechnik zur Bestimmung der turbulenten Strömungsstruktur in Mehrphasenströmungen,
Chemie Ingenieur Technik 54 (1982) 608-609

[18] Calis, H. P. A.; Nijenhuis, J.; Paikert, B. C.; Dautzenberg, F. M.; van den Bleek, C. M.:
CFD Modelling and Experimental Validation of Pressure Drop and Flow Profile in a Novel

Structured Catalytic Reactor Packing,
Chemical Engineering Science 56 (2001), 1713-1720

[19] Celik, I.; Wang, Y.-Z.:
Numerical Simulation of Liquid Circulation in a Bubbly Column,
appeared in: Celik, I.; Hughes, D.; Crowe, C. T.; Lankford, D. (Editors):
Numerical Methods for Multiphase Flows,
Proceedings, The American Society of Mechanical Engineers, New York (1990)

[20] Chang, Q.; Wong, Y. S.; Fu, H.:
On the Algebraic Multigrid Method,
Journal of Computational Physics 125 (1996) 2, 279-292

[21] Chhabra, R. P.:
Bubbles, Drops and Particles in Non-Newtonian Fluids,
CRC Press, Boca Raton / Florida (1993)

[22] Clift, R.; Grace, J. R.; Weber, M. E.:
Bubbles, Drops and Particles,
Academic Press, New York, San Francisco, London (1978)

[23] Cockx, A.; Do-Quang, Z.; Line, A.; Roustan, M.:
Use of Computational Fluid Dynamics for Simulating Hydrodynamics and Mass Transfer in Industrial Ozonation Towers, Chemical Engineering Science 54 (1999), 5085-5090

[24] Crowe, C.; Sommerfeld, M.; Tsuji, Y.:
Multiphase Flows with Droplets and Particles,
CRC Press, Boca Raton (1998)

[25] Da Silva, F. A.; Pironti, F. F.; Saez, A. E.:
The Sedimentation-Dispersion Model for Slurry Bubble Columns with a Conical Distributor,
Chemical Engineering Communications 138 (1995), 157-170

[26] Dassori, C. G.:
Three-Phase Reactor Modeling with Significant Backmixing in the Liquid Phase Using a Modified Cell Model (MCM),
Computers chem. Engng. 22 (1998), 679-682

[27] Deckwer, W.-D.:
Bubble Column Reactors,
Wiley, Chichester (1992)

[28] Delnoij, E.; Kuipers, J. A. M.; van Swaaij, W. P. M.:
A Three-dimensional CFD Model for Gas-Liquid Bubble Columns,
Chemical Engineering Science 54 (1999), 2217-2226

[29] Drew, D. A.; Passman, S. L.:
Theory of Multicomponent Fluids,
Springer-Verlag, New York, Berlin, Heidelberg (1999)

[30] Druzhinin, O. A.; Elghobashi, S. E.:
A Lagrangian-Eulerian Mapping Solver for Direct Numerical Simulation of Bubble-Laden Turbulent Shear Flows Using the Two-Fluid Formulation,
Journal of Computational Physics 154 (1999) 1, 174-196

[31] Dziallas, H.:
Lokale Phasengehalte in zwei- und dreiphasig betriebenen Blasensäulenreaktoren,
Ph. D. Thesis, Technical University of Braunschweig / Germany (2000),
in Hempel, D. C. (ed.): ibvt-Schriftenreihe, FIT-Verlag, Paderborn

[32] Dziallas, H.; Michele, V.; Hempel, D. C.:
Measurement of Local Phase Holdups in a Two- and Three-Phase Bubble Column,
Chemical Engineering and Technology 23 (2000) 10, 877-884; see also correction of misprinted figures in Chemical Engineering and Technology 24 (2001) 1, 102-103

[33] Erdal, F. M.; Shirazi, S. A.; Mantilla, I.; Shoham, O.:
Computational Fluid Dynamics (CFD) Study of Bubble Carry-Under in Gas-Liquid Cylindrical Cyclone Separators,
Society of Petroleum Engineers Production and Facilities 15 (2000) 4, 217-222

[34] Feistauer, M.:
Models and Techniques of CFD - State of Art,
Magdeburg (1997)

[35] Gervais, A.; Briens, C. L.; Andre, J. C.; Wild, G.:
A Modified Axial Dispersion Model Applied to Three-Phase Fluidized Bed Reactors with a Transition Zone,
Transactions of the Institution of Chemical Engineers 73 A (1995), 745-749

[36] Gidaspow, D.:
Multiphase Flow and Fluidization: Continuum and Kinetic Theory Descriptions with Applications, Academic Press Inc., San Diego / London (1994)

[37] Gidaspow, D.; Ding, J.; Jayaswal, U. K.:
Multiphase Navier-Stokes Equation Solver,
Appeared in: Celik, I.; Hughes, D.; Crowe, C. T.; Lankford, D. (Editors): *Numerical Methods for Multiphase Flows*, The American Society of Mechanical Engineers, New York (1990)

[38] Griebel, M.:
Numerische Simulation in der Strömungslehre - eine praxisorientierte Einführung,
Vieweg-Verlag, Braunschweig, Wiesbaden (1995)

[39] Griebel, M.; Neunhoeffer, T.; Regler, H.:
Algebraic Multigrid Methods for the Solution of the Navier-Stokes Equations in Complicated Geometries, International Journal for Numerical Methods in Fluids 26 (1998) 3, 281-301

[40] Großmann, C.; Roos, H.-G.:
Numerik partieller Differentialgleichungen,
Teubner, Stuttgart (1992)

[41] Guder, R.:
Fluiddynamik von Dreiphasenströmungen in Treibstrahl-Schlaufenreaktoren,
Ph. D. Thesis, University of Bremen / Germany, VDI-Verlag (1997)

[42] Guder, R.; Räbiger, N.:
Lokale Profile der Gas- und Flüssigphase sowie Turbulenzänderungen der Flüssigkeit als Folge von Wechselwirkungen der Dispersphasen in einem Suspensionsreaktor,
Chemie Ingenieur Technik 66 (1994) 6, 829-832

[43] Gueyffier, D.; Li, J.; Nadim, A.; Scardovelli, R.; Zaleski, S.:
Volume-of-Fluid Interface Tracking with Smoothed Surface Stress Methods for Three-Dimensional Flows, Journal of Computational Physics 152 (1999) 2, 423-456

[44] Hainke, M.; Ammon, K.; Onken, U.:
Simultane Messung von Gelöstsauerstoffkonzentration und Hydrodynamik in aeroben Submersfermentationen, Chemie Ingenieur Technik 70 (1998) 3, 299-301

[45] Hanratty, T. J.; Woods, B. D.; Iliopoulos, I.; Pan, L.:
The Roles of Interfacial Stability and Particle Dynamics in Multiphase Flows: A Personal Viewpoint, International Journal of Multiphase Flow 26 (2000), 169-190

[46] Hashiba, N.; Kojima, E.:
Simultaneous Measurement of Two-Dimensional Velocity and Direction of Liquid Flow by Cross-Correlation Method, Journal of Chemical Engineering of Japan 29 (1996) 4, 577-581

[47] Hashiba, N.; Kojima, E.:
Measurement of Liquid Circulation in Concentric Airlift Reactors by Cross-Correlation Method, Journal of Chemical Engineering of Japan 30 (1997) 1, 23-29

[48] Hetsroni, G. (Editor):
Handbook of Multiphase Systems,
McGraw Hill, New York (1982)

[49] Hetsroni, G.:
Particles-Turbulence Interaction,
International Journal of Multiphase Flow 15 (1989), 735-746

[50] Hillmer, G.:
Experimentelle Untersuchung und fluiddynamische Modellierung von Suspensionsblasensäulen, Ph. D. Thesis, University of Erlangen / Germany (1993)

[51] Ishii, M.:
Thermo-Fluid Dynamic Theory of Two-Phase Flow,
Eyrolles, Paris (1975)

[52] Ishii, M.; Zuber, N.:
Drag Coefficient and Relative Velocity in Bubbly, Droplet or Particulate Flows,
AIChE Journal 25 (5) 1979, 843-855

[53] Jakobsen, H. A.:
Phase Distribution Phenomena in Two-Phase Bubble Column Reactors,
Chemical Engineering Science 56 (2001), 1049-1056

[54] Katz, J.; Meneveau, C.:
Wake-Induced Relative Motion of Bubbles Rising in Line,
International Journal of Multiphase Flow 22 (1996) 2, 239-258

[55] Kawase, Y.; Moo-Young, M.:
Liquid Phase Mixing in Bubble Columns with Newtonian and Non-Newtonian Fluids,
Chemical Engineering Science 41 (1986), 1969-1977

[56] Kochbeck, B.; Lindert, M.; Hempel, D. C.:
Determination of Local Gas and Solid Holdups in Airlift Loop Reactors by Means of Time-Domain-Reflectometry, Chemical Engineering and Technology 20 (1997), 533-537

[57] Koh, P. T. L.; Manickam, M.; Schwarz, M. P.:
CFD Simulation of Bubble-Particle Collisions in Mineral Flotation Cells,
Minerals Engineering 13 (2000) 14-15, 1455-1463

[58] Kohnen, C.; Bohnet, M.:
Messung und Simulation der Fluidströmung in gerührten Fest/Flüssig-Suspensionen,
Chemie Ingenieur Technik 72 (2000) 6, 609-612

[59] Kojima, H.; Iguchi, A.; Asano, K.:
Solid Holdup in Bubble Columns with Suspended Solid Particles Under Continuous Operation, Canadian Journal of Chemical Engineering 62 (1984), 346-351

[60] Krishna, R.; Urseanu, M. I.; van Baten, J. M.; Ellenberger, J.:
Influence of Scale on the Hydrodynamics of Bubble Columns Operating in the Churn-Turbulent Regime: Experiments vs. Eulerian Simulation,
Chemical Engineering Science 54 (1999), 4903-4911

[61] Krishna, R.; van Baten, J. M.; Urseanu, M. I.:
Three-Phase Eulerian Simulation of Bubble Column Reactors Operating in the Churn-Turbulent Regime: A Scale-Up Strategy,
Chemical Engineering Science 55 (2000), 3275-3286

[62] Krishna, R.; Urseanu, M. I.; van Baten, J. M.; Ellenberger, J.:
Liquid Phase Dispersion in Bubble Columns Operating in the Churn-Turbulent Regime,
Chemical Engineering Journal 78 (2000), 43-51

[63] Lahey, R. T.; Drew, D. A.:
An Analysis of Two-Phase Flow and Heat Transfer Using a Multidimensional, Multi-Field, Two-Fluid Computational Fluid Dynamics (CFD) Model,
Japan / US Seminar on Two-Phase Flow Dynamics, Santa Barbara, California, June 5 - 8, 2000; available online from http://www.rpi.edu/~laheyr/ATPF.pdf

[64] LaRoche, R. D.:
The Use of Computational Fluid Dynamics for Chemical Process Engineering,
Proceedings Chemputers Europe 4, Barcelona / Spain (February 1998)

[65] Lee, S. L. P.; de Lasa, H. I.:
Radial Dispersion Model for Bubble Phenomena in Three-phase Fluidized Beds,
Chemical Engineering Science 43 (1988) 9, 2445-2449

[66] Lehr, F.; Mewes, D.:
A Transport Equation for the Interfacial Area Density Applied to Bubble Columns,
Chemical Engineering Science 56 (2001), 1159-1166

[67] Li, C.; Mosyak, A.; Hetsroni, G.:
Direct Numerical Simulation of Particle-Turbulence Interaction,
International Journal of Multiphase Flow 25 (1999) 2, 187-200

[68] Li, Y.; Zhang, J. P.; Fan, L.-S.:
Numerical Simulation of Gas-Liquid-Solid Fluidization Systems Using a Combined CFD-VOF-DPM Method: Bubble Wake Behaviour,
Chemical Engineering Science 54 (1999), 5101

[69] Lindert, M.:
Zur Maßstabsvergrößerung von Airlift-Schlaufenreaktoren,
Ph. D. Thesis, University of Paderborn / Germany (1992)

[70] Lindert, M.; Schäfer, S.; Kochbeck, B.; Hemmi, M.; Hempel, D. C.:
Bestimmung von lokalen Gas- und Feststoffgehalten in einem Airlift-Schlaufenreaktor mit Hilfe der Time-Domain-Reflectometry,
Chemie Ingenieur Technik 65 (1993) 5, 563-565

[71] Lindken, R.; Gui, L.; Merzkirch, W.:
Geschwindigkeitsmessungen in Mehrphasenströmungen mit Hilfe der Particle Image Velocimetry, Chemie Ingenieur Technik 70 (1998), 856-860

[72] Lindken, R.; Gui, L.; Merzkirch, W.:
Velocity Measurement in Multiphase Flow by Means of Particle Image Velocimetry,
Chemical Engineering and Technology 22 (1999) 3, 202-206

[73] Liu, S.:
Particle Dispersion for Suspension Flow,
Chemical Engineering Science 54 (1999), 873-891

[74] Mahnke, E. U.; Büscher, K.; Hempel, D. C.:
A Novel Approach for the Determination of Mechanical Stresses in Gas-Liquid Reactors,
Chemical Engineering and Technology 23 (2000) 6, 509-513

[75] Meili, R. T.:
Faseroptik knackt Partikelwolken,
Chemie Technik 25 (1996) 10, 56-57

[76] Menzel, T.:
Die Reynolds-Schubspannung als wesentlicher Parameter zur Modellierung der Strömungsstruktur in Blasensäulen und Airlift-Schlaufenreaktoren,
Ph. D. Thesis, University of Dortmund / Germany, VDI-Verlag (1990)

[77] Millies, M.; Mewes, D.:
Phasengrenzflächen in Blasenströmungen - Teil 1: Blasensäulen,
Chemie Ingenieur Technik 68 (1996) 6, 660-669

[78] Millies, M.; Drew, D. A.; Lahey, R. T.:
A First Order Relaxation Model for the Prediction of the Local Interfacial Area Density in Two-Phase Flows, International Journal of Multiphase Flow 22 (1996) 6, 1073-1104

[79] Mitra-Majumdar, D.; Farouk, B.; Shah, Y. T.:
Hydrodynamic Modeling of Three-Phase Flows through a Vertical Column,
Chemical Engineering Science 52 (25) 1997, 4485-4497

[80] Morii, T.; Ogawa, Y.:
Development and Application of a Fully Implicit Fluid Dynamics Code for Multiphase Flow,
Nuclear Technology 115 (1996), 333-341

[81] Mudde, R. F.; Simonin, O.:
Two- and Three-Dimensional Simulations of a Bubble Plume Using a Two-Fluid Model,
Chemical Engineering Science 54 (1999), 5061-5069

[82] Mürtz, H.:
Phasenverteilung und Suspensionsphasengeschwindigkeit in einer Suspensionsblasensäule,
Ph. D. Thesis, University of Dortmund / Germany (1990)

[83] N. N.:
CFX-4.2: Solver Manual,
AEA Technology, Harwell / UK (1997)

[84] Nienow, A. W.:
Bioreactor and Bioprocess Fluid Dynamics,
Proceedings, 3rd International Conference on Bioreactor and Bioprocess Fluid Dynamics, Cambridge, UK (September 14-16, 1993); BHR Group / Mechanical Engineering Publications Ltd., London (1993)

[85] Nigmatulin, R. I.; Lahey, R. T.; Drew, D. A.:
On the Different Forms of Momentum Equations and on the Intra- and Interphase Interac-

tion in the Hydromechanics of a Monodispersed Mixture,
Chemical Engineering Communications 141-142 (1996), 287-302

[86] Onken, U.; Buchholz, R.:
Meßmethoden in Fermentern unter sterilen Bedingungen,
Chemie Ingenieur Technik 54 (1982) 6, 581-590

[87] Onken, U.; Hainke, M.:
Measurement of Hydrodynamics and Dissolved Oxygen with a Polarographic Microelectrode,
Chemical Engineering and Technology 22 (1999) 9, 767-772

[88] Padial, N. T.; VanderHeyden, W. B.; Rauenzahn, R. M.; Yarbro, S. L.:
Three-Dimensional Simulation of a Three-Phase Draft-Tube Bubble Column,
Chemical Engineering Science 55 (2000), 3261-3273

[89] Pannek, S.:
Untersuchungen der Elektrodiffusionsmeßtechnik mit Sauerstoff als Depolarisator für den Einsatz in Mehrphasenströmungen,
Ph. D. Thesis, University of Dortmund / Germany (1996)

[90] Parasu Veera, U.:
Gamma Ray Tomography Design for the Measurement of Hold-Up Profiles in Two-Phase Bubble Columns, Chemical Engineering Journal 81 (2001), 251-260

[91] Patankar, S. V.:
Numerical Heat Transfer and Fluid Flow,
Hemisphere Publ. Co., New York (1980)

[92] Pfleger, D.; Becker, S.:
Modelling and Simulation of the Dynamic Flow Behaviour in a Bubble Column,
Chemical Engineering Science 56 (2001), 1737-1747

[93] Pfleger, D.; Gomes, S.; Gilbert, N.; Wagner, H.-G.:
Hydrodynamic Simulations of Laboratory Scale Bubble Columns Fundamental Studies of the Eulerian-Eulerian Modelling Approach,
Chemical Engineering Science 54 (1999), 5091 - 5099

[94] Prasser, H.-M.; Schaffrath, A.:
Workshop on Measuring Techniques for Steady State and Transient Multiphase Flows 1999,
Kerntechnik 64 (1999) 5-6, 309-310

[95] Ranade, V. V.; Tayalia, Y.:
Modelling of Fluid Dynamics and Mixing in Shallow Bubble Column Reactors: Influence of Sparger Design, Chemical Engineering Science 56 (2001), 1667-1675

[96] Reinecke, N.; Mewes, D.; Schmitz, D.; Petritsch, G.:
Tomographische Meßverfahren - Visualisierung zwei- und dreidimensionaler Datenfelder, Chemie Ingenieur Technik 69 (1997), 1254

[97] Riquarts, H.-P.:
Strömungsprofile, Impulsaustausch und Durchmischung der Flüssigphase in Blasensäulen, Chemie Ingenieur Technik 53 (1981) 1, 60-61

[98] Rodi, W.:
Turbulence Models and their Application in Hydraulics - A State of the Art Review, Habilitation Thesis, University of Karlsruhe / Germany (1980)

[99] Sanyal, J.; Vasquez, S.; Roy, S.; Dudukovic, M. P.:
Numerical Simulation of Gas-Liquid Dynamics in Cylindrical Bubble Column Reactors, Chemical Engineering Science 54 (1999), 5071-5083

[100] Sato, Y.; Sekoguchi, K.:
Liquid Velocity Distribution in Two-Phase Bubble Flow, International Journal of Multiphase Flow (1975) 2, 79

[101] Sauer, T.; Hempel, D. C.:
Fluid Dynamics and Mass Transfer in a Bubble Column with Suspended Particles, Chemical Engineering and Technology 10 (1987), 180-189

[102] Schlüter, M.; Räbiger, N.:
Bubble Swarm Velocity in Two Phase Flows, HTD-Vol. 361, Proceedings of the ASME Heat Transfer Division, Anaheim / California, Volume 5, ASME 1998

[103] Schlüter, S.:
Modellierung und Simulation von Blasensäulenreaktoren, Ph. D. Thesis, University of Dortmund / Germany (1992)

[104] Schügerl, K.; Lübbert, A.; Korte, T.; Diekmann, J.:
Meßtechnik zur Charakterisierung von Gas/Flüssigkeitsreaktoren, Chemie Ingenieur Technik 57 (1985) 8, 641-650

[105] Schütze, J.; Gollmer, K.; Deckwer, W.-D.:
Der Einsatz numerischer Strömungssimulation zur Modellierung aerober Bioprozesse,
Proceedings, 16. DECHEMA-Jahrestagung der Biotechnologen, Wiesbaden / Germany, May 26-28, 1998

[106] Schweitzer, J.-M.; Bayle, J.; Gauthier, T.:
Local Gas Holdup Measurements in Fluidized Bed and Slurry Bubble Column,
Chemical Engineering Science 56 (2001), 1103-1110

[107] Seeger, A.; Affeld, K.; Goubergrits, L.; Richard, N.; Kertzscher, U.; Wellnhofer, E.:
X-Ray Based Assessment of the Three-Dimensional Velocity of the Liquid Phase in a Bubble Column,
Proceedings of the Third International Workshop on PIV '99, Santa Barbara (1999), 519-524

[108] Shimizu, K.; Takada, S.; Minekawa, K.; Kawase, Y.:
Phenomenological Model for Bubble Column Reactors: Prediction of Gas Hold-Ups and Volumetric Mass Transfer Coefficients,
Chemical Engineering Journal 78 (2000), 21-28

[109] Sokolichin, A.; Eigenberger, G.:
Bubble Column Reactors - Applicability of the standard k-ε turbulence model to the dynamic simulation of bubble columns: Part I. Detailed Numerical Simulations,
Chemical Engineering Science 54 (1999), 2273-2284

[110] Sommer, K.; Bohnet, M.:
Modellierung von Dreiphasen-Wirbelschicht-Bioreaktoren im Hochleistungsbetrieb,
Chemie Ingenieur Technik 68 (1996) 9, 1083-1084

[111] Sommer, K.:
Modellierung der Strömung und des Stofftransportes in Dreiphasen-Wirbelschicht-Bioreaktoren, Ph. D. Thesis, Technical University of Braunschweig / Germany, Shaker Verlag, Aachen (1997)

[112] Sommerfeld, M.:
Numerical Simulation of the Particle Dispersion in Turbulent Flow: The Importance of Particle Lift Forces and Particle/Wall Collision Models,
appeared in: Celik, I.; Hughes, D.; Crowe, C. T.; Lankford, D. (Editors):
Numerical Methods for Multiphase Flows,
Proceedings, The American Society of Mechanical Engineers, New York (1990)

[113] Sommerfeld, M.; Decker, S.; Kohnen, G.:
Time-dependent Calculation of Bubble Columns Based on Reynolds-averaged Navier-Stokes Equations with k-ε Turbulence Model,
Proceedings of the 2nd Japanese-German Symposium on Multi-Phase Flow, Tokyo, 1997, Paper No. 3-1-4, pp. 323-334

[114] Soong, Y.; Fauth, D. J.; Knoer, J. P.:
Ultrasonic Characterization of Solids Holdup in a Bubble Column Reactor,
Chemical Engineering and Technology 23 (2000) 10, 751-753

[115] Steinemann, J.:
Charakterisierung des Gasphasenverhaltens in Blasensäulen mittels einer neuentwickelten elektrischen Mehrpunkt-Leitfähigkeitssonde,
Ph. D. Thesis, University of Dortmund / Germany (1985)

[116] Sundaresan, S.:
Modeling the Hydrodynamics of Multiphase Flow Reactors: Current Status and Challenges,
AIChE Journal 46 (2000) 6, 1102 - 1105

[117] Sussman, M.; Puckett, E. G.:
A Coupled Level Set and Volume-of-Fluid Method for Computing 3D and Axisymmetric Incompressible Two-Phase Flows,
Journal of Computational Physics 162 (2000) 2, 301-337

[118] Tillenkamp, F.; Loth, R.:
Phase Distribution Measurements During Transient Bubbly Two-Phase Flow in a Vertical Pipe, Chemical Engineering and Technology 23 (2000) 4, 347-352

[119] Triesch, O.; Bohnet, M.:
Einfluss von Partikeln auf die Fluidturbulenz in einer verzögerten Gas/Feststoffströmung,
Chemie Ingenieur Technik 72 (2000) 8, 848-852

[120] Truckenbrodt, E.:
Lehrbuch der angewandten Fluidmechanik,
Springer-Verlag, Berlin, Heidelberg, New York (1988)

[121] Tsuchiya, K.; Ohsaki, K.; Taguchi, K.:
Large and Small Bubble Interaction Patterns in a Bubble Column,
International Journal of Multiphase Flow 22 (1996) 1, 121-132

[122] Vial, C.; Laine, R.; Poncin, S.; Midoux, N.; Wild, G.:
Influence of Gas Distribution and Regime Transitions on Liquid Velocity and Turbulence in a 3-D Bubble Column, Chemical Engineering Science 56 (2001) 1085-1093

[123] Wang, M.; Dorward, A.; Vlaev, D.; Mann, R.:
Measurements of Gas-Liquid Mixing in a Stirred Vessel Using Electrical Resistance Tomography, 1st World Congress on Industrial Process Tomography, Buxton, Greater Manchester, April 14-17, 1999

[124] Warsito; Ohkawa, M.; Kawata, N.; Uchida, S.:
Cross-Sectional Distributions of Gas and Solid Holdups in Slurry Bubble Column Investigated by Ultrasonic Computed Tomography,
Chemical Engineering Science 54 (1999), 4711-4728

[125] Webster, R.:
An Algebraic Multigrid Solver for Navier-Stokes Problems,
International Journal for Numerical Methods in Fluids 18 (1994), 761-780

[126] Wilcox, D. C.:
Turbulence Modelling for CFD,
2nd Edition, DCW Industries, Inc., La Cañada, California (1998)

[127] Witt, P. J.; Perry, J. H.; Schwarz, M. P.:
A Numerical Model for Predicting Bubble Formation in a 3D Fluidized Bed,
Applied Mathematical Modelling 22 (1998) 1071-1080

[128] Wolff, C.:
Untersuchungen mit Mehrkanal-Mikrosonden zum Einfluß suspendierter Feststoffe auf die Hydrodynamik in Blasensäulen-Reaktoren für Chemie und Biotechnologie,
Ph. D. Thesis, University of Aachen / Germany, VDI-Fortschritt-Berichte, Reihe 3, Nr. 176, VDI-Verlag (1989)

[129] Wu, Y.; Al-Dahhan, M. H.:
Prediction of Axial Liquid Velocity Profile in Bubble Columns,
Chemical Engineering Science 56 (2001), 1127-1130

[130] Yin, F. H.; Sun, C. G.; Afacan, A.; Nandakumar, K.; Chuang, K. T.:
CFD Modeling of Mass Transfer Processes in Randomly Packed Distillation Columns,
Industrial and Engineering Chemistry Research 39 (2000) 5, 1369 - 1380

[131] Zehner, P.; Benfer, R.:
Modelling Fluid Dynamics in Multiphase Reactors,
Chemical Engineering Science 51 (10) 1996, 1735-1744